

***MULTI-SCALE MAPPING OF DIAGENETIC PROCESSES IN SANDSTONES
USING IMAGING SPECTROSCOPY: A CASE STUDY OF THE FRONTIER
FORMATION (WYOMING, U.S.A.) AND THE UTRILLAS FORMATION
(BURGOS, SPAIN)***

A Thesis Presented to
the Faculty of the Department of Earth and Atmospheric Sciences
University of Houston

In Partial Fulfillment
of the Requirements for the Degree
Master of Science

By
Virginia Alonso de Linaje de Nicolás
University of Houston
December 2016

**MULTI-SCALE MAPPING OF DIAGENETIC PROCESSES IN SANDSTONES
USING IMAGING SPECTROSCOPY: A CASE STUDY OF THE FRONTIER
FORMATION (WYOMING, U.S.A.) AND THE UTRILLAS FORMATION
(BURGOS, SPAIN)**

Virginia Alonso de Linaje de Nicolás

APPROVED:

Dr. Shuhab Khan, Chairman

Dr. Julia Wellner, Member

Dr. Janok P. Bhattacharya, Member

Dr. Álvaro Jimenez-Berrocso, Member

Dean, College of Natural Sciences and Mathematics

ACKNOWLEDGEMENTS

I would like to express my gratitude to Dr. Shuhab Khan, from believing on me since the beginning, his guidance and encouragement during these two years. My special thanks to my committee members, Dr. Julia Wellner, Dr. Janok Bhattacharya, and Dr. Álvaro Jiménez-Berrocoso for their support and comments improving the manuscript.

I also wish to thank my friends and colleagues from the Geological Remote Sensing Laboratory: Diana Krupnik, Kivanc Biber, Ismail Abir, Wanda Crupa, Jingqiu Huang, Juhi Aggarwal, and Macey Crockett for their helpful tips and assistance when needed. I want to specially thank Lei Sun, Proma Bhattacharyya, and Ünal Okyay for their support in the field and data collection. Thanks to my university friends Alberto Carballo and Carolina Ramon for our everlasting lunch time breaks and laughs together.

Last but not least, my special thanks to my beloved family: Ama, Aita, Beatriz, Mami, and Kantha for their emotional support and encouragement every single day. A special thanks to my “Bilboko lagunak” and my new Woodlands’ family.

***MULTI-SCALE MAPPING OF DIAGENETIC PROCESSES IN SANDSTONES
USING IMAGING SPECTROSCOPY: A CASE STUDY OF THE FRONTIER
FORMATION (WYOMING, U.S.A.) AND THE UTRILLAS FORMATION
(BURGOS, SPAIN)***

An Abstract of a Thesis

Presented to

the Faculty of the Department of Earth and Atmospheric Sciences

University of Houston

In Partial Fulfillment

of the Requirements for the Degree

Master of Science

By

Virginia Alonso de Linaje de Nicolás

University of Houston

December 2016

ABSTRACT

Imaging spectroscopy is applied to two sandstone formations to study diagenetic processes in sedimentary deposits. Spectral data from hand specimens and cores were acquired and compared with close-range hyperspectral imaging to analyze lateral and vertical geochemical variations and quantify facies and diagenetic mineral abundances. The study was carried out on the delta front deposits of Wall Creek Member of the Cretaceous Frontier Formation, Wyoming and on the upper member of the Utrillas Formation, Spain. Visible Near-Infrared (VNIR) and Shortwave-Infrared (SWIR) Specim® hyperspectral cameras were used to scan near vertical and well exposed outcrop walls. Reflectance spectra was analyzed and compared with high resolution laboratory spectral and hyperspectral imaging data, thin sections, and results of previous sedimentological studies.

Spectral Angle Mapper (SAM) and Mixture Tuned Matched Filtering (MTMF) classification algorithms were applied to quantify facies and mineral abundances in the Frontier Formation. MTMF is the most effective and reliable technique when studying spectrally similar materials. Classification results show that Parasequence #6 of the Wall Creek Member in the Frontier Formation is composed of 87 m² of bar facies, 150 m² of channel facies, 11 m² of distal facies, and 27 m² of carbonate concretions. Calcite cement in channel facies concretions is homogeneously distributed, whereas the bar facies was shown to be interbedded with layers of non-calcite-cemented sandstone.

Distinctive characteristics of the absorption features of clay minerals (well-ordered kaolinite, poorly-ordered kaolinite, and mica (illite + muscovite)) were used to identify authigenic kaolinite and detrital kaolinite in the Utrillas Formation. Results show that poorly-ordered kaolinite is only present in floodplain deposits, while well-ordered authigenic kaolinite

is related to paleochannel deposits and organic rich irregular patches. Meteoric water flux probably induced feldspar and mica alteration, and authigenic clays precipitation. Contemporary bacterial degradation of organic matter might be the cause of authigenic clay formation. The exposures of Utrillas Formation at Basconcillos del Tozo quarry are composed of 214 m² of paleochannel facies, 235 m² of floodplain facies, and 36 m² of altered areas.

Key words: Hyperspectral imaging, diagenesis, MTMF, SAM, Frontier Formation, Utrillas Formation, spectroscopy,

TABLE OF CONTENTS

LIST OF FIGURES	ix
LIST OF TABLES	xvi
LIST OF APPENDIX	xvi
CHAPTER 1	1
1. INTRODUCTION	1
1.1 MOTIVATION	2
1.2 OBJECTIVES	4
1.3 ORGANIZATION OF THE THESIS	4
1.4 GEOLOGICAL SETTING	5
1.4.1 The Frontier Formation, Wall Creek Member in Raptor Ridge (Wyoming, US).....	5
1.4.2 The Utrillas Formation in Basconcillos del Tozo (Spain)	13
CHAPTER 2	19
2. METHODOLOGY & DATA SET	19
2.1 IMAGE SPECTROSCOPY	19
2.1.1 Image Spectroscopy in Geologic Studies	24
2.2 DATA SET	25
2.2.1 Spectral Data	25
2.2.2 Hyperspectral Data	26
2.2.3 Petrography	40
CHAPTER 3	42
3. RESULTS: THE FRONTIER FORMATION	42
3.1 SPECTRAL DATA	42
3.2 HYPERSPETRAL DATA	47
3.2.1 Imaging of Core Samples	48
3.2.2 Imaging of the Outcrop	51
3.3 DISCUSSION	58
CHAPTER 4	61
4. RESULTS: THE UTRILLAS FORMATION	61
4.1 STRATIGRAPHY AND SEDIMENTOLOGY	61

4.2	SPECTRAL DATA	63
4.3	HYPERSPETRAL DATA.....	66
4.3.1	Imaging of Rock Samples	66
4.3.2	Imaging of the Outcrop.....	72
4.4	PETROGRAPHY	79
4.5	DISCUSSION.....	84
CHAPTER 5	88
5. CONCLUSIONS	88
REFERENCES	92
A. APPENDIX A	100

LIST OF FIGURES

Figure 1-1 (a) Location of the study area. (b) General overview map showing studied outcrop distribution of the Frontier Formation and major basins in Wyoming, USA. The study area is located in Big Sulphur Draw, Natrona County. (c) Map of Raptor ridge with the locations of studied outcrop in the Parasequence #6 and cores (Wall Creek Member, Frontier Formation). (Modified from Gani & Bhattacharya 2007). Map source: Esri, Digital Globe..... 6

Figure 1-2 (a) Cretaceous stratigraphy of the Powder River Basin, Wyoming. (b) Outcrop type section of the Wall Creek Member at Raptor Ridge site. (c) Lithologic and ichnologic symbols used in logs. The study section is in a dashed red rectangle. (From Gani and Bhattacharya 2007). 8

Figure 1-3 Detailed identification of sedimentary features of cliff face in the depositional dip direction. See Figure 1-1 for location. (a) Facies map diagram. (b) Distribution of carbonate concretions, distributary mouth bars and laterally migrating channels. (modified from Gani & Bhattacharya 2007; Lee et al. 2007). 12

Figure 1-4 Regional geological map of the Basque Cantabrian Basin northern Spain and location of Sedano trough. Abbreviations in map: Ay-1, Ayoluengo-1; Ay-32, Ayoluengo-32; Bas, Basconillos; Cad, Cadialso-1; Cant, Cantonegro-1; Cor, Cordovilla; Hui, Hidobro-1 and 2; Hon, Hontomin-1 and 2; Oll, Olleros; Pol, Polientes-1; Poza, Poza de la Sal; Sal, Salinas de Pisuerga; Toz, Tozo-1; Zam, Zanzas A-1; Vill, Villanueva de Rampalay. Abbreviations in legend: Ku, Late Cretaceous; KL-J, Early Cretaceous to Jurassic; Pz, Palaeozoic (modified from Beroiz & Permanyer 2011). 14

Figure 1-5 (a) Geological map of the NW Burgos province, Castilla y Leon, Spain. Scale 1:50,000. (data from IGME, Cartografía- Geológica GEODE 50). (b) Aerial photograph with locations of hyperspectral VNIR and SWIR scans in the Basconillos del Tozo quarry. Note, as the quarry is active it is a dynamic system, so the image does not exactly match with time of scanning. (Source: Esri Digital Globe, GeoEye, Earthstar). 15

Figure 1-6 Mesozoic and Lower and Middle Cenozoic stratigraphy chart of the Sedano Trough, southwest sector of the Basque-Cantabrian Basin. Lithology, previously described megasequences and major structural events are depicted. The study section is in a dashed red rectangle. Colors are correlated to Figure 1-4 (modified from Beroiz & Permanyer 2011). 16

Figure 2-1 Mineral spectra in the VNIR and SWIR area of the electromagnetic spectra. Notice that quartz and feldspars do not show any characteristic absorption features. Data from U.S. Geological Survey spectral Library (Clark et al., 2007)). K-Fd= Potasic Feldspar, Na-Fd= Sodium feldspar, Q= quartz, C= calcite, K= kaolinite, H= hematite, G= Goethite..... 21

Figure 2-2 Graph showing reflectance spectra vs. wavelength in nm. Data from U.S. Geological Survey spectral library (Clark et al. 2007).(a) Reflectance spectra of poorly-ordered kaolinite, well-ordered kaolinite, and illite. (b) Continuum removed reflectance spectra from the U.S. Geological Survey spectral library of poorly-ordered kaolinite, well-ordered kaolinite, and illite. Abbreviations: [K- Poorly Ordered] =poorly-ordered kaolinite, [K- Well-ordered] = well-ordered kaolinite. 22

Figure 2-3 Data acquisition methods. (a) ASD FieldSpec Pro spectroradiometer. (b) VNIR and SWIR cameras mounted in the Pan and Tilt rotating stage for outcrop scanning at the Utrillas Formation. The cameras were faced perpendicular to the outcrop. Notice the white reference panel parallel to the outcrop face. (c) Laboratory scanning system for core and rock samples. SWIR and VNIR cameras were fixed while the remotely controlled moving stage, which allows the samples to go through the scanning area. 28

Figure 2-4 Optimal scanning position for ground-based imaging spectroscopy. Wider dash lines show the direct light path. Thinner red dashed lines correspond to reflected and/or scattered light from adjacent surfaces and/or atmosphere (after Kurz et al. 2013)..... 29

Figure 2-5 Workflow diagram for hyperspectral image preprocessing and steps used in the ongoing research. 30

Figure 2-6 Definition of the continuum removal and absorption features characteristics. The spectra were extracted from the SWIR hyperspectral image at Raptor Ridge, after bad bands removal (after Van der Meer 2004)..... 35

Figure 2-7 Scatter plots for the MTMF results showing Mf score in X-axis and infeasibility results in Y-axis. Pixels that have MTMF scores greater than 0.5 and infeasibility values smaller than 30 were used and plotted in the red rectangle. The rest of the classified pixels were not taken into account. (a) Scatter plot showing Mf scores vs. Infeasibility results for the concretions endmember in Raptor Ridge. (b) Scatter plot showing Mf scores vs. Infeasibility results for the sandstone endmember in Raptor Ridge. 39

Figure 3-1 (a) Photographs of three of the four boxes of core eight from Raptor Ridge. Red points correspond to areas where spectral data were collected. Red dashed lines correspond to areas that were imaged by hyperspectral cameras. (b, c, d, and e) Graph displaying spectral reflectance data (in percentage) vs. wavelength (in nanometers) collected from selected spots on core eight shown in red dots from Figure 3-1a. Each graph corresponds to points collected in b-bar facies, c-channel facies, d-carbonate concretions in bar facies, e-carbonate concretions in channel facies. Main absorption peaks are depicted. 45

Figure 3-2 (a) Photographs of three of the four boxes of core nine from Raptor Ridge. Red points correspond to areas where spectral reflectance data were collected. Red dashed lines correspond to areas that were imaged by hyperspectral cameras. (b, c, and d) Graph displaying spectral reflectance data (in percentage) vs. wavelength (in nanometers) collected from selected spots on core nine shown in red dots from Figure 3-2a. Each graph corresponds to points collected in b-bar facies, c-channel facies, d-carbonate concretions in bar facies. Main absorption peaks are depicted. 46

Figure 3-3 SWIR absorption features of clay minerals and calcite in spectral data collected in different point of core eight and core nine. For location refer to Figure 3-1 and Figure 3-2. The red rectangles and green triangles correspond to calcite and kaolinite reflectance parameters, respectively. Blue and red areas correlate with carbonate concretions in channel facies and bar facies, respectively. 47

Figure 3-4 Photomosaic (resolution of ~0.5 cm) image depicting different endmembers selected for classification purposes. Endmembers were selected based on field observations, previous geological studies and spectral analysis. (a) Frontal splay deposits. (b) Iron oxide surface alterations. (c) Carbonate concretions and channel facies. (d) Bar facies. (e) Channel facies and prodelta facies. 48

Figure 3-5 Core eight and core nine from Raptor Ridge. (Column a) Core photograph. (Column b) False-color composite image with spectral bands 2,195 nm, 2,334 nm, and 2,152 nm displayed as RGB. (Column c) Spectral Angle Mapper classified image using U.S. Geological Survey spectral library from calcite and kaolinite. (Column D) Normalized spectra depicting depth at band 2,334 nm (calcite). Darker red means deeper absorption features; hence greater abundance. (Column E) Normalized spectra depicting depth at band 2,195 nm (kaolinite). Darker red means deeper absorption features; hence greater abundance. 50

Figure 3-6 (a) Outcrop VNIR image in true color composite showing bands 174, 111, and 55 displayed as RGB. (b) Minimum Noise Fraction Transformation image for SWIR with bands 4,7,8 displayed as RGB. (c) Band ratios image for SWIR data displayed in (B_1/B_2) to enhance spectral

differences $[B_1=(B_{2328nm}+B_{2334nm}+B_{2322nm})/3, B_2= (B_{2152nm}+B_{2159nm}+B_{2171nm})/3]$. *Grey and black pixels correspond to mask areas in A and B, respectively*..... 51

Figure 3-7 SWIR spectra of ROI's that were used for classification purposes. (a) Selected endmembers in the coherent MNF bands for MTMF classification. (b) Reflectance spectra of the selected endmembers in the hyperspectral image for SAM classification. (b') Continuum removed reflectance spectra of the selected endmembers in the hyperspectral image for SAM classification. Gaps in reflectance spectra correspond to water absorptions at 1,400 nm and 1,900 nm that were removed from the image. (c) Reflectance of facies derived from SWIR spectral data of cores. (c') Continuum removed reflectance of facies derived from SWIR spectral data of cores. (d) Reflectance of facies derived using spectroradiometer data. (d') Continuum removed reflectance of facies derived from spectroradiometer data. (e) Spectra of kaolinite and calcite and kaolinite:50 %-calcite: 50 % created from U.S. Geological Survey spectral library (Clark et al. 2007). (e') Continuum removed spectra of kaolinite and calcite and kaolinite:50 %-calcite: 50% created from U.S. Geological Survey (Clark et al. 2007)..... 54

Figure 3-8 (a) Hyperspectral map extracted from the MTMF image using SWIR data set is depicted. Only pixels where MT score are >50 % or more, and infeasibility less than 30 were plotted. (b) Reclassified rule-based SAM image using extracted endmember from the image itself based on field data. (c) Reclassified rule-based SAM image using SWIR hyperspectral image spectra collected in the laboratory. (d) Reclassified rule-based SAM image using endmembers extracted from spectral data. 56

Figure 3-9 (a) SAM classified image using normalized SWIR image for kaolinite. Red corresponds to kaolinite free areas. Maximum content of kaolinite is shown in blue. (b) Normalized image showing 2,205 nm wavelength depth that corresponds to kaolinite absorption feature. (c) Normalized image depicting 2,334 nm wavelength depth that correspond to the absorption feature of calcite. Darker red areas correspond to greater depth features; hence more abundance. A threshold of 0.95 was used for noise removal. 57

Figure 3-10 Comparison of normalized abundance of endmembers based on different classification methods in SWIR image of Raptor Ridge. All calculations were normalized excluding masked pixels for results. 57

Figure 4-1 Schematic stratigraphic column for the outcrop of the Utrillas Formation. The locations for hand samples are shown. Figure 4-8a is for the S-W outcrop wall, whereas, W-E outcrop wall is shown in Figure 4-9a. 62

Figure 4-2 Photographs of the Utrillas Formation outcrop at Basconillos del Tozo. (a) The top sandstone package (in Figure 4-1) with planar cross stratification. Red dashed follow the stratification. Erosional contact between claystone and sandstone layers is marked by yellow line. (b) Conglomeratic sandstone at the base of the second sandstone package. claystone layers with supergenic alteration minerals that provide this reddish, yellowish color. (c) Fracture claystone with yellowish color. (d) Presence of native sulfur as an alteration product..... 63

Figure 4-3 (a) Photograph of thin sections of samples from Utrillas Formation. (b) Plots showing the reflectance spectra in nanometers of the thin sections data collected with spectroradiometer (continuous lines) and laboratory setting SWIR hyperspectral image (dashed lines). Colors were chosen randomly..... 65

Figure 4-4 (a) True color composite image using the VNIR data of hand samples collected from the Utrillas Formation displayed as R: 475 nm, G: 510 nm, B: 650 nm. (b) MNF results for SWIR images with bands 7,5,4 displayed as RGB. (c) Band ratios image created from normalized data displayed as RGB. R: (B1,958 nm/B1,649 nm), G: (B2,171 nm/B2,127 nm), B: (B2,151 nm/ B2,127 nm). 67

Figure 4-5 SAM classification image based on SWIR data from U.S. Geological Survey spectral library of: micaceous phase: Illite, well-ordered kaolinite [WO-K] and, poorly-ordered kaolinite [PO-K]. The angular similarity threshold was always lower than 0.1 radians and different for each endmember. 67

Figure 4-6 (a) Graph depicting wavelength (μm) vs. reflectance of the U.S. Geological Survey spectra of: illite in black, well-ordered kaolinite in blue, and poorly-ordered kaolinite in green. (b) Zoom to the graph A depicting the differences between illite, well-ordered kaolinite, and poorly-ordered kaolinite at $\sim 2,206$ nm absorption minimum. (c) Continuum removed reflectance spectra from 2,140 nm to 2,450 nm showing the bands used for kaolinite-crystallinity index and Micaceous Phase (MP) abundance index. 70

Figure 4-7 (a) Hyperspectral images of hand samples from the Utrillas Formation generated by applying 'Kaolinite-Crystallinity Index'. Warm colors are indicative of low values, thus presence of well-ordered kaolinite. Cold colors indicate high values, thus presence of poorly-ordered-kaolinite. (b) Classified image generated by applying 'Micaceous phase-crystallinity Index. Only pixels with 2,203 nm absorption feature depth greater than 0.95, of the continuum-removed image where used for classification. Abbreviations: PO-kaolinite and WH% low= poorly-ordered kaolinite and low-micaceous phase abundance, PO-kaolinite and WH% high= Poorly-ordered kaolinite and high-micaceous phase abundance, WO-kaolinite and WH% low= Well-ordered kaolinite and low-micaceous phase abundance, WO-kaolinite and WH% high= Well-ordered kaolinite and high-micaceous phase abundance..... 71

Figure 4-8 S-N outcrop of the Utrillas formation at Basconillos del Tozo. See Figure 1-5 for location. (a) True color composite VNIR image displaying bands R: 640 nm, G: 549 nm, and B: 469 nm. (b) Minimum Noise Fraction image for SWIR data with bands 2, 5, and 6 displayed as RGB. (c) Band-ratios image displayed as R: (Band 2,171 nm/Band 2,203 nm), G: (Band 2,203 nm/Band 2,171 nm), B: (Band 2,159 nm/ Band 2,171 nm). (Graph a) Example of continuum removed reflectance spectra of poorly-ordered kaolinite found in the flood-plain facies. (Graph b) Example of continuum-removed reflectance spectra of well-ordered kaolinite found in the paleochannel facies. (Graph c) Example of continuum-removed reflectance spectra of well-ordered kaolinite and calcite cement. 73

Figure 4-9 W-E outcrop of the Utrillas formation (a) True color composite VNIR image displaying bands R:640 nm, G:549 nm, and B:469 nm. (b) Minimum Noise Fraction image based on SWIR image with bands 1, 5, and 3 displayed as RGB. (c) Band-ratios image displayed as RGB the following: R: (Band 2,171 nm/Band 2,203 nm), G: (Band 2,203 nm/Band 2,171 nm), B: (Band 2,159 nm/ Band 2,171 nm). (Graph a) Example of continuum-removed reflectance spectra of poorly-ordered kaolinite found in the flood-plain facies. (Graph b) Example of continuum-removed reflectance spectra of well-ordered kaolinite found in the paleochannel facies. (Graph c) Example of continuum removed reflectance spectra of well-ordered kaolinite and calcite cement. 75

Figure 4-10 (a) SAM classification image of the S-N outcrop wall using ASD from collected hand samples. (b) SAM classification image of the S-N outcrop wall using U.S. Geological Survey spectral library of: micaceous phase: Illite, well-ordered kaolinite [WO-K], poorly-ordered kaolinite [PO-K], and calcite. The angular-similarity threshold was always lower than 0.1 radians and different for each endmember. 76

Figure 4-11 (a) SAM classification image of the W-E outcrop wall using spectral data of hand samples. (b) SAM classification image of the W-E outcrop wall using U.S. Geological Survey spectral library of: Micaceous phase: Illite, well-ordered kaolinite [WO-K], poorly-ordered kaolinite [PO-K], and calcite. The angular-similarity threshold was always lower than 0.1 radians and different for each endmember. 76

Figure 4-12 (a) “Kaolinite Crystallinity Index” resulting image for S-N outcrop of the Utrillas Formation. Warm colors are indicative of low values, thus presence of well-ordered kaolinite. Cold colors indicate high values, thus presence of poorly-ordered kaolinite. (b) “Micaceous phase -crystallinity Index” resulting image for S-N outcrop of the Utrillas Formation. Only pixels with 2,203 nm absorption feature depth greater than 0.95, of the continuum-removed image where used for classification. Abbreviations: PO-kaolinite and MP% low= poorly-ordered kaolinite and low-micaceous phase abundance, PO-kaolinite and MP% high= Poorly-ordered kaolinite and high-micaceous phase abundance, WO-kaolinite and MP% low= Well-ordered

kaolinite and low-micaceous phase abundance, WO-kaolinite and MP% high= Well-ordered kaolinite and high- micaceous phase abundance. 77

Figure 4-13 (a) “Kaolinite Crystallinity Index” image for W-E outcrop of the Utrillas formation. Warm colors are indicative of low values, thus presence of well-ordered kaolinite. Cold colors indicate high values, thus presence of poorly-ordered kaolinite. (b) “Micaceous phase-crystallinity Index” resulting image for W-E outcrop of the Utrillas Formation Only pixels with 2,203 nm absorption feature and depth greater than 0.95, of the continuum-removed image where used for classification. Abbreviations: PO-kaolinite and MP% low= poorly-ordered kaolinite and low-micaceous phase abundance, PO-kaolinite and MP% high= Poorly-ordered kaolinite and high-micaceous phase abundance, WO-kaolinite and MP% low= Well-ordered kaolinite and low-micaceous phase abundance, and WO-kaolinite and MP% high= Well-ordered kaolinite and high-micaceous phase abundance. 78

Figure 4-14 SWIR reflectance spectra of the results of MPAI results. (a) SWIR reflectance spectra. (b) Normalized SWIR reflectance spectra from 2120 nm- 2430 nm. Blank areas in the left side of graph correspond to water absorptions. Black arrows point out distinctive characteristics of each endmember. Abbreviations: PO-MP Low= poorly-ordered kaolinite and low-micaceous phase abundance, PO-MP High = Poorly-ordered kaolinite and high-micaceous phase abundance, WO_MP Low = Well-ordered kaolinite and low-micaceous phase abundance, WO_MP High= Well-ordered kaolinite and high-micaceous phase abundance. 79

Figure 4-15 Q-F-RF compositional diagram of the sandstones from the Utrillas formation. 80

Figure 4-16 Photomicrographs of samples from the Utrillas Formation. (a) Fan-shape authigenic kaolinites growing at the edge of a monocrystalline quartz grain with straight extinction in sample Can-9 in plain light. (b) Poorly-sorted sandstone with micas bent and broken at the edges of the grains replaced by kaolinite in sample Can-2 in crossed nicols. (c) Pore-filling authigenic kaolinite in sample Can-9 in crossed nicols. (d) Fe-oxide cement (goethite) surrounded by a monocrystalline angular-quartz grain with undulose extinction in crossed nicols. (Can-M). (e) Laminated mudstone in sample Can-9 in crossed nicols. (f) Claystone in sample Can-F in crossed nicols. Qtz=quartz, M=Muscovite, ak=authigenic kaolinite, Yellow dashed indicated direction of lamination. 83

Figure 4-17 Facies interpretation of the Utrillas Formation outcrop based on SWIR classification methodologies. 86

LIST OF TABLES

Table 1-1 University departments and research groups currently working in close range hyperspectral for geological studies worldwide. The table is based on the research done until finalizing this thesis (Sept. 2016).	3
Table 1-2 Architectural elements and lithofacies description of Wall Creek Member Parasequence #6 in Raptor Ridge, Wyoming. F1: Facies 1; F2: Facies 2; F4: Facies 4; F5:Facies5. (after Gani & Bhattacharya 2007).....	10
Table 1-3 Percentage distribution of carbonate concretions at the outcrop and core scales. ..	11
Table 2-1 Characteristics of VNIR and SWIR Specim [®] cameras (from www.specim.fi).....	27
Table 4-1 Major absorption minimum in spectral data of the hand specimen. Grey color corresponds to absorption minimum related to water. Red color corresponds to absorption minimum related to iron oxide minerals. Blue color corresponds to absorption minimum related to clay minerals.....	64
Table 5-1 Advantages vs. disadvantages of imaging spectroscopy applied to sandstone outcrop studies.....	88

LIST OF APPENDIX

Appendix A-1 Tables with primary observation for the thin sections of the Utrillas Formation.....	100
Appendix A-2 Point counting results of the Utrillas Formation facies. Abbreviations QRF: Quartz, Rock fragments, Feldspar, Rock Frag: rock fragments.....	103

CHAPTER 1

1. INTRODUCTION

Post-depositional mineralogical alteration due to fluid-flow migration can control flow paths by affecting rock porosity and permeability in reservoirs (hydrocarbon and/or groundwater). After deposition, depending on the fluid chemistry, new minerals can fill up pores spaces, significantly reducing the porosity of the rock. Alternatively, the mineral phase can be dissolved, increasing porosity and permeability (Dutton et al., 2002; Taylor & Machent, 2011). Therefore, high resolution quantitative mineral mapping will be an excellent way to understand complex diagenetic processes and reduce uncertainty in reservoir characterization. The failure to recognize precipitation of authigenic cements in geologic formations may cause the failure of the reservoir and/or lateral migration. There are many examples in sandstone reservoirs where calcite concretions and clay cements changed flow dynamics and reduced reservoir quality (Bjørkum & Walderhaug 1993; Hassouta et al. 1999; Dutton et al. 2000; Dutton et al. 2002).

Geologists use a variety of methods to determine diagenetic minerals distribution and mineral composition such as: X-ray diffraction (XRD), electron microscope (SEM), and petrographic studies. These traditional methods are time consuming, economically expensive, some methods have scale limitations, and some others are destructive (Zaini et al., 2014). Therefore, interpolation and generalization is used by geoscientists to estimate diagenetic effects and other mineralogical variations. Imaging spectroscopy and these traditional methodologies can be combined to improve reservoir characterization studies.

However, portable hyperspectral cameras have opened up new horizons for mineralogical characterization at different scales, from hundreds of meters (outcrop) to millimeters (laboratory specimens) (Murphy et al. 2012; Murphy & Monteiro 2013; Schneider et al. 2014;

Boesche et al. 2015). This technique has proven to be very effective to quantify mineralogy and composition without “*a priori*” knowledge of the formation (Murphy et al. 2014). Previous studies used drilled cores for quantitative geological mapping and mineral classification (Kruse 1996; Taylor et al. 2000; Gallie et al. 2002; Bolin & Moon 2003; Kruse et al. 2010; Kruse et al. 2012).

For this study, two sandstone outcrops were selected. Both of them display geochemical variations due to diagenetic processes (Lee et al. 2007; Nyman et al. 2014; AGGEP 2015). The first outcrop belongs to the Wall Creek Member of the Frontier Formation, in Wyoming. The location is informally known as “Raptor Ridge”. In this document, this outcrop is named as Raptor Ridge. The second outcrop includes sands and clays of the Utrillas Formation, in Basconcillos del Tozo (Spain). Both of these outcrops were scanned by Visible Near-Infrared (VNIR) and Shortwave-Infrared (SWIR) hyperspectral cameras. Representative samples and core samples were used for laboratory analyses. In addition, hyperspectral scanning and spectral data were collected in the laboratory and thin sections were studied for confirmation of remote-sensing data.

1.1 MOTIVATION

Spectral data, multispectral and, hyperspectral satellite images have been effectively utilized in the geological studies in the last decade. However, in recent years, new portable cameras (e.g., Specim, Finland; HySpex Norway) allowed geologists to apply the same techniques at smaller scales, increasing the resolution and applicability to scientific research, in the oil and gas and the mining industry among others.

Other than the Geological Remote Sensing Laboratory at the University of Houston, there are very few institutes and universities around the world that own VNIR and SWIR cameras, equipment and trained geologists capable of collecting geological field hyperspectral data, processing, and interpretation (Table 1-1).

Table 1-1 University departments and research groups currently working in close range hyperspectral for geological studies worldwide. The table is based on the research done until finalizing this thesis (Sept. 2016).

GROUP NAME/PROJECT NAME	MAIN RESEARCHER	WEBSITE	COUNTRY
University of Houston/Department of Earth and Atmospheric Science	Shuhab Khan	http://www.uh.edu/~sdkhan/	United States of America
University of Twente/ ITC Faculty of Geo_information Science and Earth Observation	Freek Van de Meer	https://www.itc.nl/geological-remote-sensing	The Netherlands
UniResearch/ Center for integrated Petroleum Research/Virtual Outcrop Geology Group	Tobias Kurz	http://org.uib.no/cipr/Project/V OG/hyperspectral.htm	Norway
Geological Survey of Sweden		http://www.sgu.se/en/mineral-resources/geological-information-for-mineral-exploration/drill-core-collection/drill-core-scanning-at-sgu/	Sweden
The University of Sydney/ Engineering & Information Technologies	Richard Murphy	http://sydney.edu.au/engineering/index.shtml	Australia
Rochester Institute of Technology/Target Detection Blind Test	John Kerekes	http://dirsapps.cis.rit.edu/blindtest/	United States of America
UniCamp/ Instituto de Geociência	Carlos Roberto de Souza Filho	http://portal.ige.unicamp.br/	Brazil
University of Alberta	Benoit Rivard, Michael Lipsett	https://uofa.ualberta.ca/faculties-and-programs/centresinstitutes/centre-for-earth-observation-sciences	Canada

1.2 OBJECTIVES

Spectral data were used to analyze the two outcrops and representative samples. The main objectives for this thesis are:

1. Testing imaging spectroscopy capabilities with different spectral and spatial datasets and select the best classification technique for sandstone studies.
2. High-resolution mapping of diagenetic cements in the Frontier Formation and the Utrillas Formation sandstones to better understand their secondary-mineral distribution at different scales using an image spectroscopy approach.
3. Facies distribution and abundance based on spectral differences and comparison with previous published sedimentological data.
4. Determination of kaolinite-illite distribution within the Utrillas Formation outcrop and its possible relationship between hydrocarbon micro-seepages and development of kaolinite layers.

1.3 ORGANIZATION OF THE THESIS

The thesis is distributed in five chapters. In chapter 1, the introduction, motivation, objectives, geological setting, and previous sedimentological studies carried out in the Frontier Formation and the Utrillas Formation are described. Chapter 2 explains the different data sets that were used in this work and the methodology and approach used during the ongoing research. As two different formations were studied, results and discussion are compiled in chapter 3 for the Frontier Formation and chapter 4 for the Utrillas Formation. Finally, chapter 5 summarizes conclusions and recommendations for further study.

1.4 GEOLOGICAL SETTING

1.4.1 The Frontier Formation, Wall Creek Member in Raptor Ridge (Wyoming, US)

The study area is located between The Powder River Basin and Wind River Basin in Wyoming (Figure 1-1a & b). After the Sevier Orogeny (Middle and/or Late Jurassic), clastic sediments were transported from uplifted strata into the western margin of the Western Interior seaway (Wiltschko & Dorr 1983). Consequently, the Frontier Formation clastic wedge prograded east and southeastward from the Sevier orogenic belt into a foreland basin that contained the western margin of the Cretaceous Western Interior Seaway during the Upper Cretaceous (Cenomanian-Turonian) (Bhattacharya & Willis 2001). The area was later deformed into a series of anticlines during the Laramide Orogeny (Maastrichtian-Tertiary) (Wiltschko & Dorr 1983).

The Frontier Formation is sandwiched by older Mowry and younger Cody Shales that are marine mudstones deposited during regional transgressions of the seaway (Willis et al. 1999). The Frontier Formation consists of, at least, three unconformity-bounded members (from oldest to youngest): the Cenomanian Belle Fourche Member, the Emigrant Gap Member of Middle Turonian age, and the Upper Turonian Wall Creek Member (Merewether 1996; Bhattacharya & Willis 2001) (Figure 1-2). The Frontier Formation consists of shale, inter-stratified claystones, siltstones, sandstone bodies, pebble conglomerates, and bentonite horizons that consist of thick successions of non-marine to thinner marine interbedded with shale at the Raptor Ridge study area.

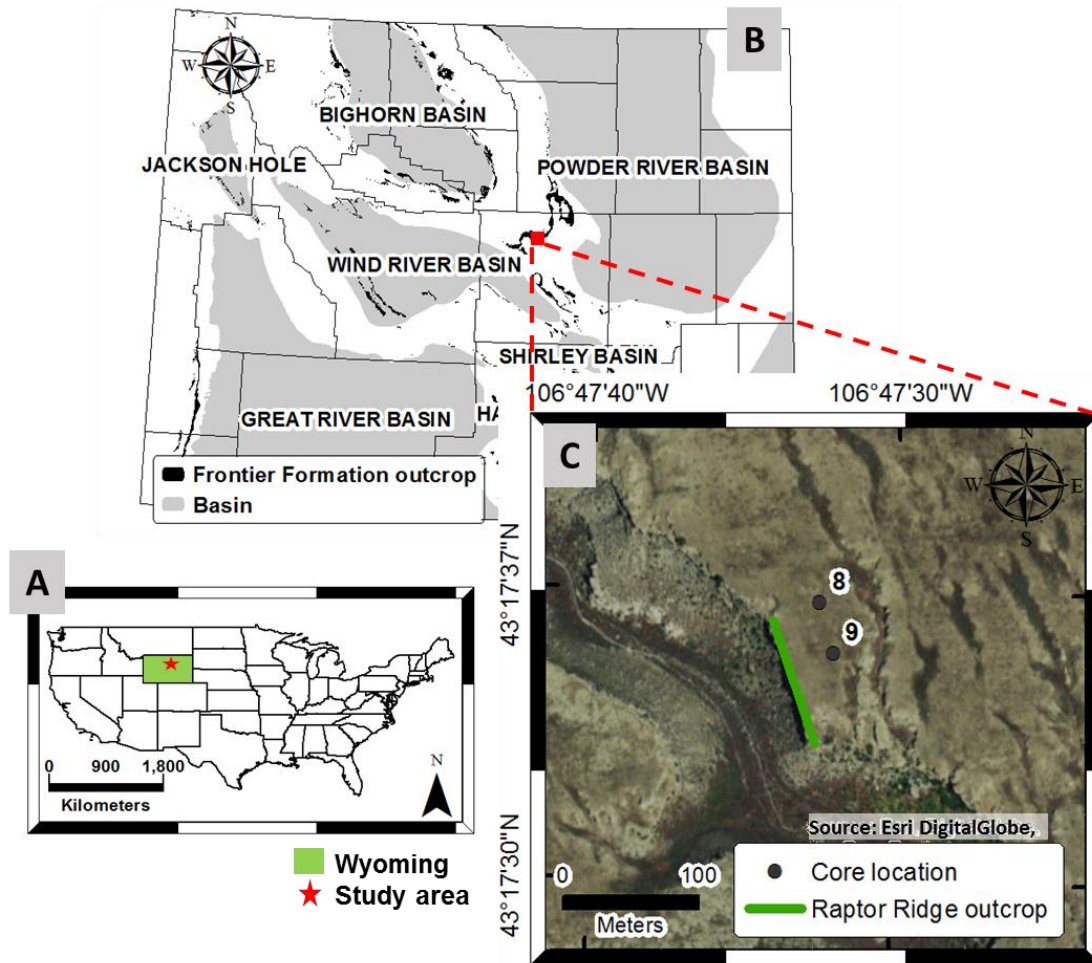


Figure 1-1 (a) Location of the study area. (b) General overview map showing studied outcrop distribution of the Frontier Formation and major basins in Wyoming, USA. The study area is located in Big Sulphur Draw, Natrona County. (c) Map of Raptor ridge with the locations of studied outcrop in the Parasequence #6 and cores (Wall Creek Member, Frontier Formation). (Modified from Gani & Bhattacharya 2007). Map source: Esri, Digital Globe.

The Wall Creek Member of the Frontier Formation is Upper Cretaceous (Turonian 93.5 Ma) in age and deposited under fluvial-deltaic conditions. This member is composed of seven major sand bodies deposited in shallow marine conditions under cyclic transgressions-regressions during a lowstand (Gani & Bhattacharya 2007). Each of the seven bodies shows one or more upward-coarsening facies successions (i.e., parasequences), that are bounded by a marine

flooding surface. A detailed stratigraphy of the Lower and Upper Cretaceous in the Powder River Basin and an outcrop type section can be found in Figure 1-2.

Parasequence #6 of the Wall Creek Member spectacularly crops out at the study area, Raptor Ridge, Wyoming (43° 17' 30.85''N, 106° 47' 27.65''W). In this work, only the cliff face in the depositional dip direction was analyzed. Parasequence #6 presents a lobate geometry with a shore parallel elongation, interpreted to have a mixed-influence (river and tide) deltaic origin. It is capped by a transgressive ravinement surface (Gani, 2005).

High-resolution cliff mapping allowed identification of six architectural elements, that were defined as one or a package of stratum that form the building-blocks of a depositional system (Gani & Bhattacharya 2007; Lee et al. 2007) (Figure 1-3a). The summary of the architectural elements and facies description is shown in Table 1-2. Lee et al. (2007) summarized the facies distribution showing the alternation of southward-dipping clinofolds of the distributary mouth bars (in yellow) that are separated by laterally migrating channels (in orange), in Figure 1-3b.

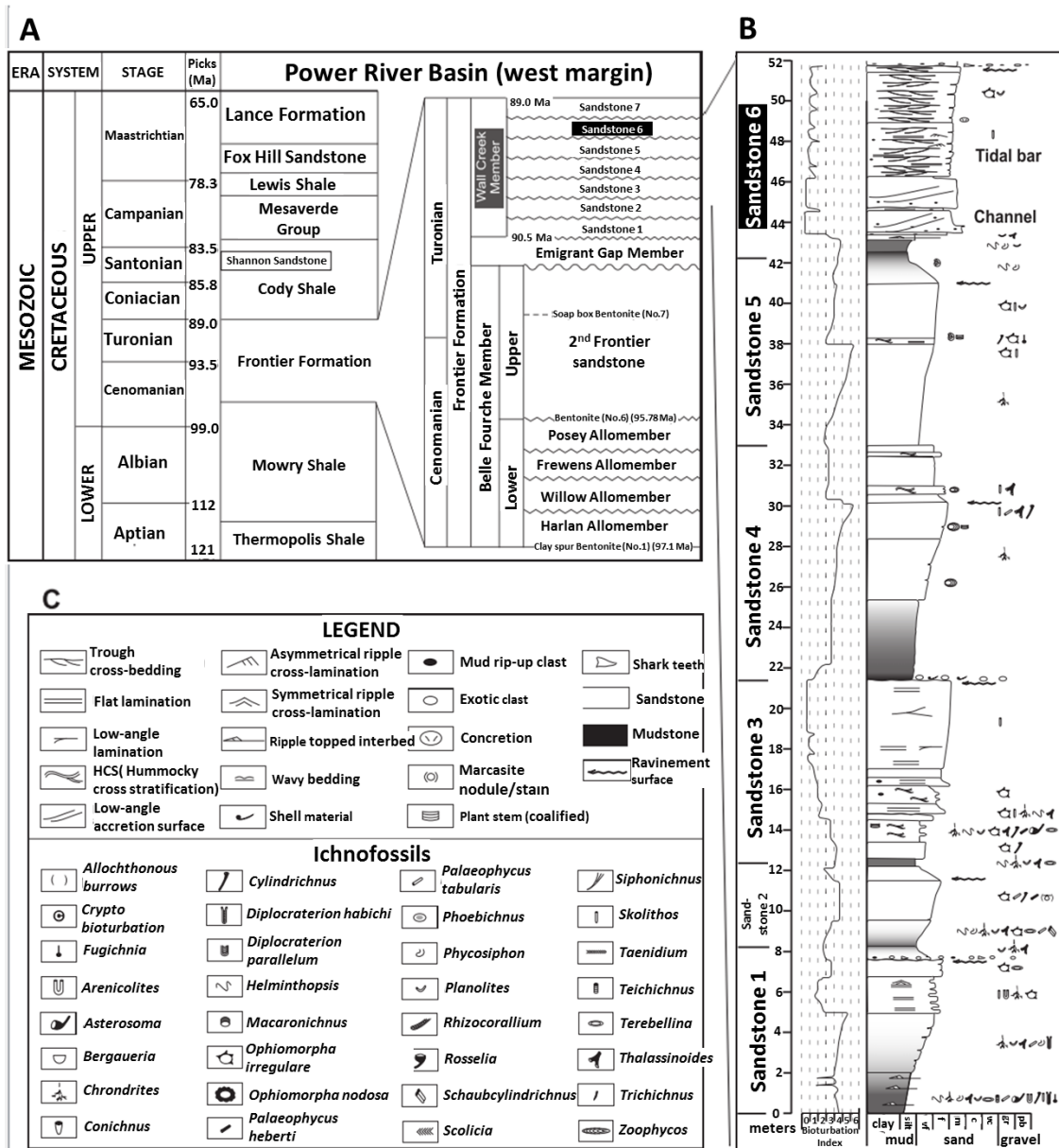


Figure 1-2 (a) Cretaceous stratigraphy of the Powder River Basin, Wyoming. (b) Outcrop type section of the Wall Creek Member at Raptor Ridge site. (c) Lithologic and ichnologic symbols used in logs. The study section is in a dashed red rectangle. (From Gani and Bhattacharya 2007).

Previous studies at the outcrop scale mapped and described the distribution of carbonate concretions (Lee et al. 2007; Nyman et al. 2014). Additionally, ten cores, drilled near the outcrop were used to integrate and interpret sedimentological and ichnological characteristics (Gani et

al., 2008). 3D-concretion distribution studies using Ground Penetrating Radar (GPR), core data, and outcrop description show that concretions are elongated and tabular in shape (Lee et al. 2007). The thickness of the concretions in the cliff face ranges from 0.2 to 1.7 m with a maximum length of 10 m. Concretions are not uniformly distributed, being more abundant in channel facies (Lee et al. 2007). Carbonate concretions represent 12.1 % (5.5 % in bar facies and 9.7 % in channel facies) of the total outcrop area. At the same time, core analyses suggest that the abundance of carbonate concretions was greater, 14.5 % in bar facies and 10.5 % in channel facies. This slight difference could be attributed to the irregular distribution of concretions, having a dendritic and aggregate pattern (Lee et al. 2007; Nyman et al. 2014) (Table 1-3).

Isotopic data ($\delta^{18}\text{O}$ and $\delta^{13}\text{C}$) suggested that the main source of carbon comes from alteration of organic matter, sea water, and marine skeletal carbonate. At a later stage, Ca^+ may have come from dissolution of volcanic rock fragments and bentonites (Nyman et al. 2014).

FACIES	DESCRIPTION	LITHOFACIES DESCRIPTION	SEDIMENTARY DEPOSITION	ARCHITECTURAL ELEMENTS	OUTCROP PICTURE
Facies 1	Thinly laminated sandy mudstones	Sandy mudstone with < 25 % of very fine grained sands. Abundant bioturbation with preserved paper thin lamination and sporadic marcasite (FeS ₂) nodules (1-4 mm in diameter).	Open marine environment and possible frequent river input.	Prodelta fines	
Facies 2	Heterolithic	Interbedded mudstones and thick (< 5 cm) very fine to fine grained, asymmetric rippled sandstone beds. Mud chips and coal chips (a 2-5 mm long).	Fluctuating mudstones and sandstones with some wave activity. Non-marine sedimentary source through a possible distributary channel		
Facies 3	Massive to parallel laminated sandstones	Sharp to erosional based and fine to medium grained sandstones. Sandstone beds range from 5 to 40 cm thick.	Gravity deposits. Waning sediments gravity flows from high sediments discharge during river floods slump failures at a river mouth, and/or storm re-suspension of bottom sediments. Middle to lower delta front deposits.	Frontal Splay	
Facies 4	Channelized sandstones	Medium-grained sandstones showing erosional channel bases and mostly sharp upper boundaries. Mud clast and convoluted bedding are observed locally. Erosional U-shape depressions and thin lateral wings indicating channelized flows.	Sediment gravity flow events. Channelized gravites deposited in a lower to middle delta front environment.	Channel	
Facies 5a	Trough cross-stratified sandstone	Fine to medium grained sandstone. Seaward-directed, and occasionally landward-directed, trough cross-stratified sandstones with scattered clasts (mostly mudstones, rarely shells and coals).	Deposition due to the migration of simple and/or compound dunes. Local decrease or increase in flow velocity and tidal periodicities. Proximity to a river source.	Bar accretion	
Facies 5b		Fine to medium grained sandstone. Landward-directed or alternating seaward-directed and landward-directed trough cross-stratified sandstones with mud and shell clasts, mostly along foresets.	Deposited in a lower to upper delta front environment.	Tidally modulated deposits	
Facies 6	Hummocky cross-stratified sandstones (HCS)	Hummocky cross-stratified fine to medium grained sandstone beds ranging in thickness from a few centimeters to few decimeters. Wavy to parallel lamination, gutter casts, and symmetrical wave ripples. Rare mud and coal clasts.	Strong oscillatory flows and unidirectional currents during storms. Distal to middle delta front shoreface environment.	Storm Sheet	

Table 1-2 Architectural elements and lithofacies description of Wall Creek Member Parasequence #6 in Raptor Ridge, Wyoming. F1: Facies 1, F2: Facies 2, F4: Facies 4, F5: Facies 5. (after Gani & Bhattacharya 2007)

Table 1-3 Percentage distribution of carbonate concretions at the outcrop and core scales.

OUTCROP (%)		REFERENCES
Bars	Channel	
12		(Nyman et al. 2014)
5.5	9.7	(Lee et al. 2007)

Sandstones at Raptor Ridge are described as upper fine grained, moderately sorted, sub-angular to sub-rounded feldspathic litharenite to lithic arkoses (Q₅₁, F₂₁, R₂₈) with an equal abundance of K-feldspar and plagioclase. Within the concretions, calcic-plagioclase is preferentially replaced by calcite. Rock fragments are composed of volcanics, chert, and sedimentary fragments. Some accessory minerals includes biotite, chalcedony, and carbonate grains (Lee et al. 2007; Nyman et al. 2014). The major diagenetic cements are calcite and authigenic chlorite. Minor diagenetic cements includ kaolinite, iron-oxide, and quartz overgrowth. The concretions are entirely cemented by calcite with minor authigenic, kaolinite, chlorite co-existing in the margins forming pore filling and pore lining phases. Cements are confined in the middle part of the sandstone body, suggesting preferential flow path (Nyman et al. 2014).

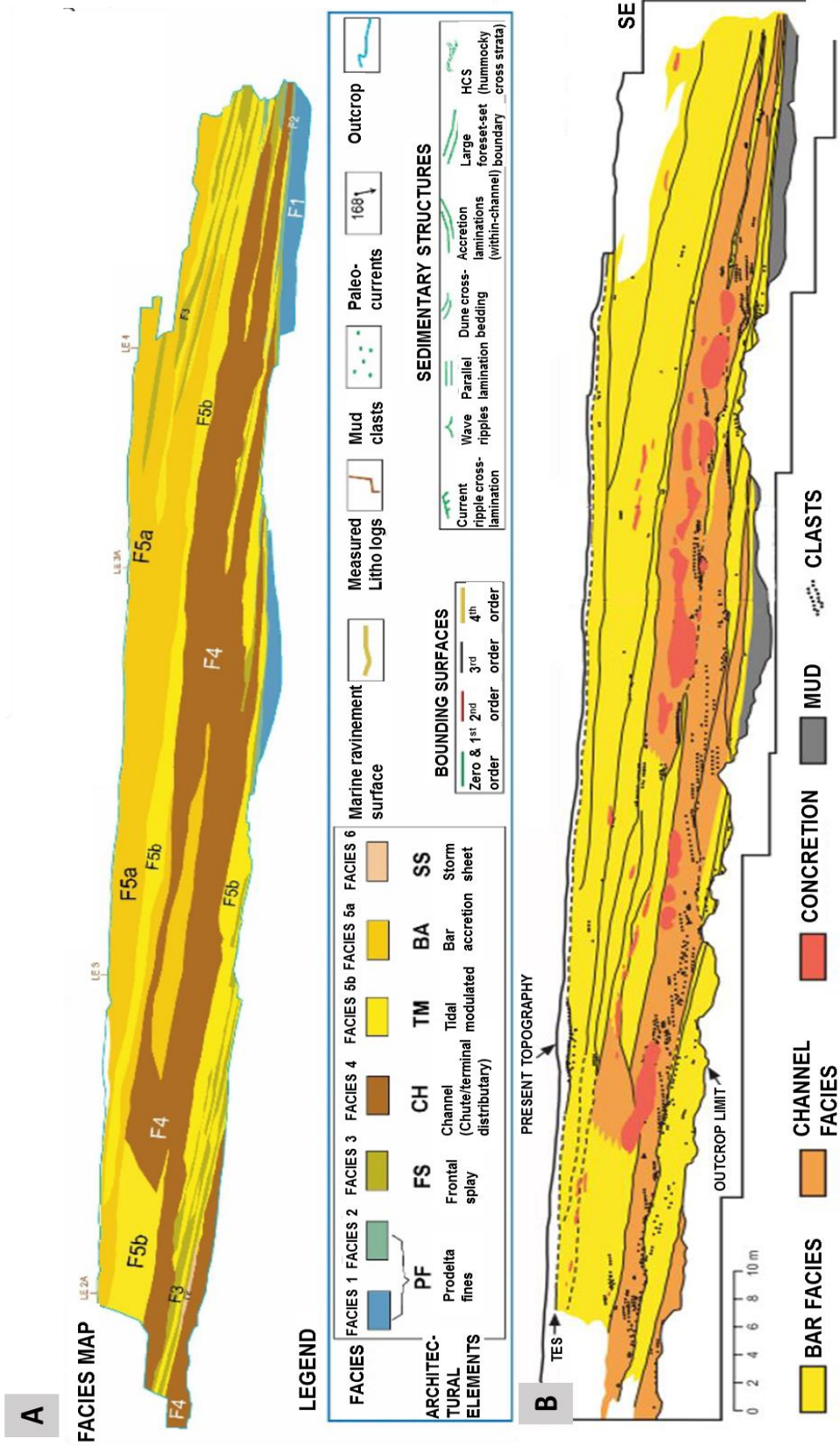


Figure 1-3 Detailed identification of sedimentary features of cliff face in the depositional dip direction. See Figure 1-1 for location. (a) Facies map diagram. (b) Distribution of carbonate concretions, distributary mouth bars and laterally migrating channels. (modified from Gani & Bhattacharya 2007; Lee et al. 2007).

1.4.2 The Utrillas Formation in Basconillos del Tozo (Spain)

The study area (42°41'38.87"N, 3°58'35.72"W) is located in a quarry at Basconillos del Tozo (Burgos, Spain) and in the southwest margin of the Basque Cantabrian Basin (Figure 1-4 and Figure 1-5). At this location, the Utrillas Formation crops out at three clean surfaces (East, South, West directions) that make it ideal site for scanning.

In the study area, Permian-Triassic rifting was associated with extensional faulting and volcanic activity, followed by the deposition of a thick clastic interval and a salt sequence during the Upper Triassic. During the second rifting phase, the Sedano trough was formed accommodating the Upper Jurassic-Lower Cretaceous continental to paralic clastic section. Triassic salt moved towards the basin margins, creating broad swells along the Zamanzas and Ubierna trends. Transtension, which occurred during Aptian-Albian, made the salt domes break, and reactivated NW-SE and NE-SW trending basement structures. During the Pyrenean compressional phase, left- and right-lateral wrenching occurred along previously reactivated trends bordering the Sedano trough, the Zamanzas to the NE and the Ubierna zone to the SW (Canerot et al., 2005).

From Late Carboniferous to the recent, seven megasequences were described (Figure 1-6). They are formed by continental, shallow-marine, and deep marine sedimentary rocks with a thickness greater than 10 km (Ramírez del Pozo 1969; Beroiz & Permanyer 2011).

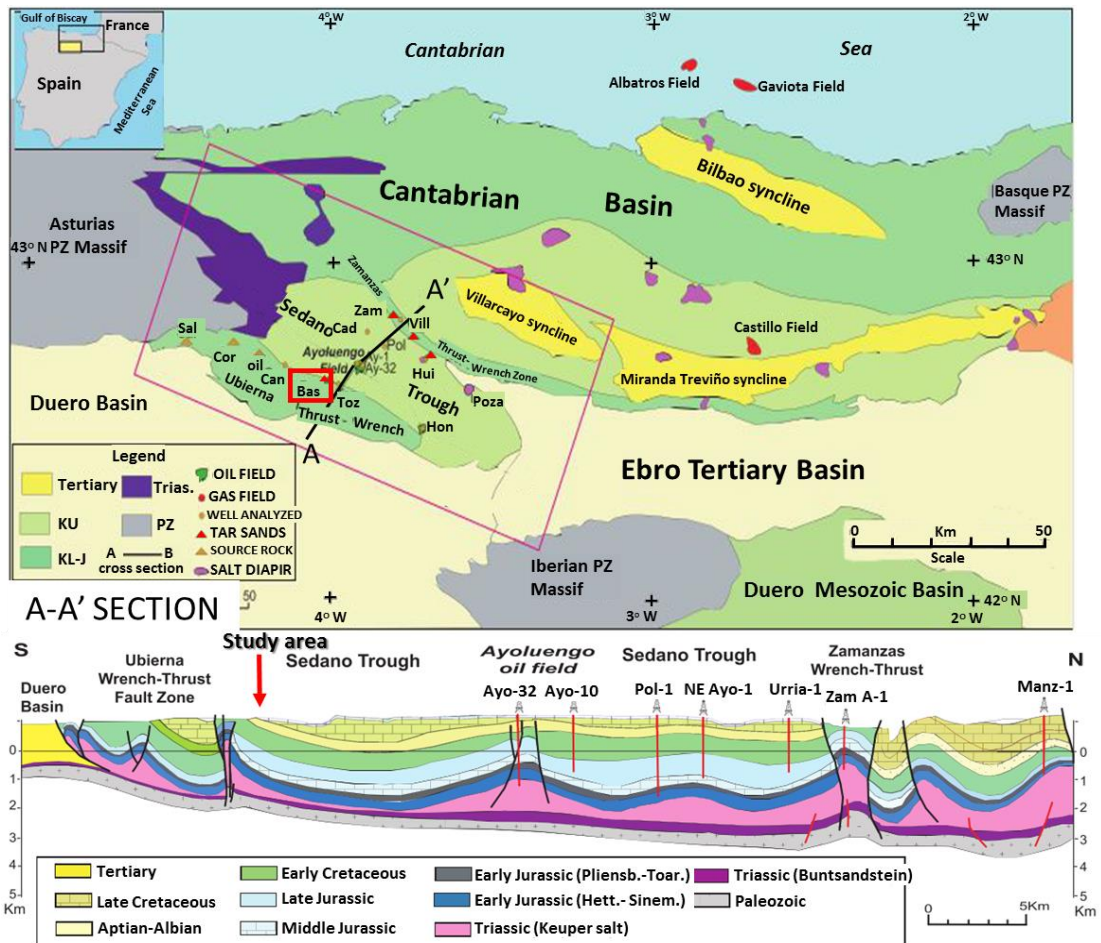


Figure 1-4 Regional geological map of the Basque Cantabrian Basin northern Spain and location of Sedano trough. Abbreviations in map: Ay-1, Ayoluengo-1; Ay-32, Ayoluengo-32; Bas, Basconillos; Cad, Cadialso-1; Cant, Cantonegro-1; Cor, Cordovilla; Hui, Hidobro-1 and 2; Hon, Hontomin-1 and 2; Oll, Olleros; Pol, Polientes-1; Poza, Poza de la Sal; Sal, Salinas de Pisuega; Toz, Tozo-1; Zam, Zamanzas A-1; Vill, Villanueva de Rampalay. Abbreviations in legend: Ku, Late Cretaceous; KL-J, Early Cretaceous to Jurassic; Pz, Palaeozoic (modified from Beroiz & Permanyer 2011).

The Utrillas megasequence was first defined by Aguilar et al. (1971). It was deposited in the Early Cretaceous (Upper Albian-Lower Cenomanian) and it is associated with the transgression that occurred in the Lower Cretaceous (ITGE 1994). To the north, these facies laterally changes to deltaic-marine deposits and tubiditic sequences. In the study area, the Utrillas Formation is composed of a 230 m of fluvial siliciclastic strata, composed of interbedded sandstones,

siltstones, and claystones, which are bounded concordantly by the Upper Cretaceous shallow marine carbonates at the top, and with Wealden megasequence at the bottom (Figure 1-6).

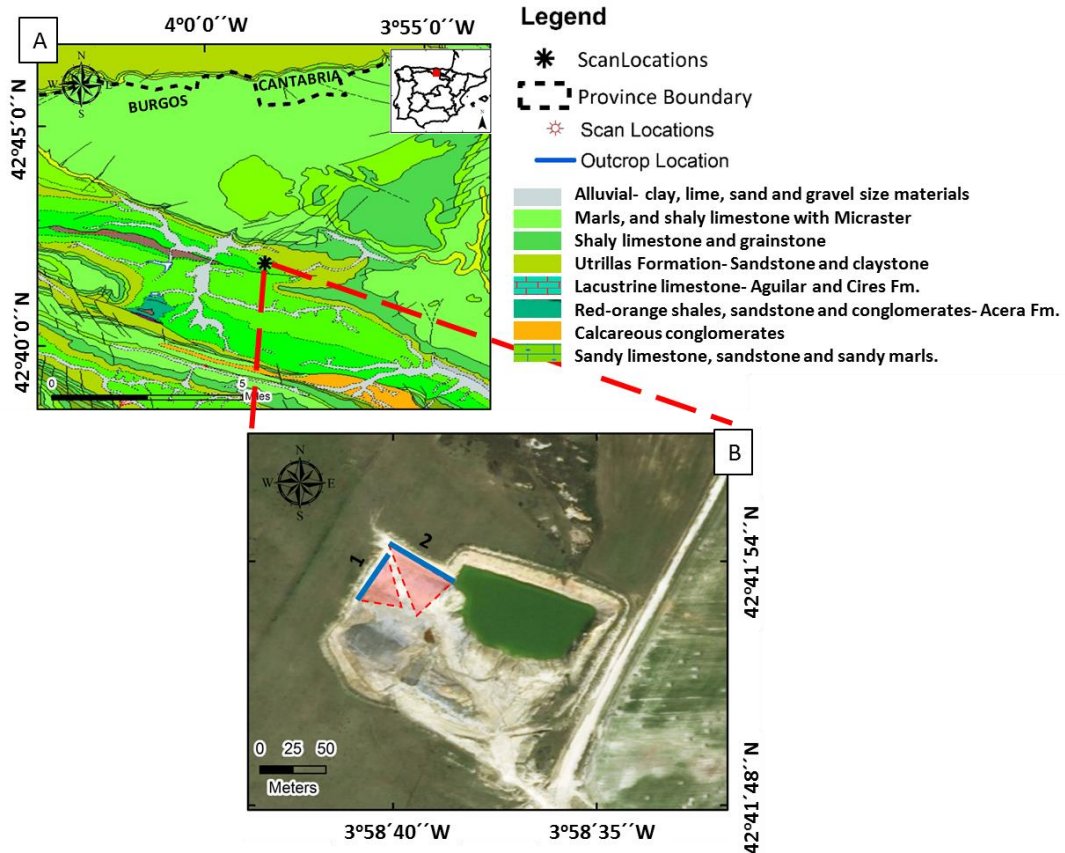


Figure 1-5 (a) Geological map of the NW Burgos province, Castilla y Leon, Spain. Scale 1:50,000. (data from IGME, Cartografía- Geológica GEODE 50). (b) Aerial photograph with locations of hyperspectral VNIR and SWIR scans in the Basconcillos del Tozo quarry. Note, as the quarry is active it is a dynamic system, so the image does not exactly match with time of scanning. (Source: Esri Digital Globe, GeoEye, Earthstar).

The facies were interpreted to be part of fluvial channels-fills, inter-channel subaerial, and floodplain deposits (ITGE 1994; Arostegui et al. 2000). It is subdivided into two sub-members. The lower member (U1) corresponds to braided channel deposits and the upper member (U2) is interpreted as meandering stream and floodplain deposits (Marfil & Gomez-Gras 1992; Arostegui et al. 2000).

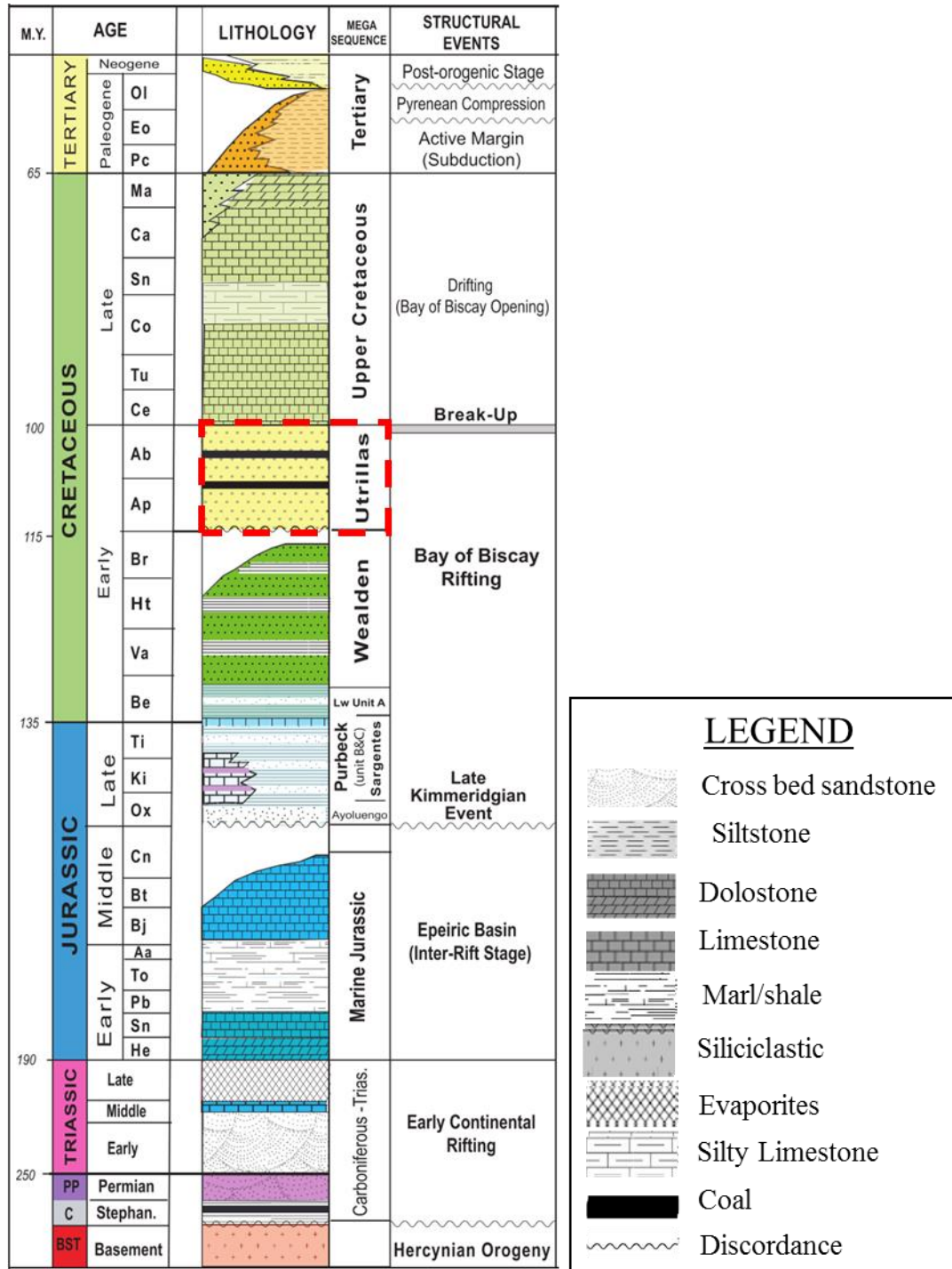


Figure 1-6 Mesozoic and Lower and Middle Cenozoic stratigraphy chart of the Sedano Trough, southwest sector of the Basque-Cantabrian Basin. Lithology, previously described megasequences and major structural events are depicted. The study section is in a dashed red rectangle. Colors are correlated to Figure 1-4 (modified from Beroiz & Permanyer 2011).

Sandstones found in the Utrillas Formation were described as siliceous conglomerates, poorly cemented white fine to medium sandstone, arenites, and greywackes with low diagenesis. The U1 sub-member is described as a lithic greywacke while the U2 sub-member is composed of quartz- arenite and subarkose. The main framework constituents are quartz (monocrystalline and polycrystalline) and scarce potassium feldspar grains (< 10 %). The matrix is formed by microcrystalline quartz and clay minerals, kaolinite that occasionally contains some micaceous phase (illite/mica). The pseudo-hexagonal fragmented shape of Illite crystals suggest a detrital origin. Kaolinite is the main cement constituent and it was probably formed by the dissolution of plagioclase and k-feldspar under the influence of meteoric water and probably some CO₂ rich or organic acid rich fluids (Arostegui et al. 2000). Kaolinite abundance is greater at the top and bottom of the formation where sandstones are in contact with the shales (Bauluz et al. 2008). This suggests some kind of interaction between organic acid or CO₂ fluids. Occasionally, siderite is replaced by Fe-oxides and small amounts of pyrite, jarosite, and organic matter were found (ITGE 1994). In some of the measured sections interbedded versicolor shales with lignite, asphalt, and pyrite have been described (ITGE 1994).

XRD and scanning electron microscopy (SEM) studies from Bauluz et al. (2008) confirmed the presence of different types of kaolinite with different morphology, crystallinity, degree of ordering, and crystal perfection in layers of sandstone, siltstone, and claystone of the Utrillas Formation. Authigenesis of kaolinites gives information about the physiochemical conditions at the time of deposition as well as the stage of diagenetic evolution (Arostegui et al. 2001).

In sandstone layers, kaolinite displays high crystallinity and a high degree of ordering, euhedral hexagonal plates (up to 1 µm in size) and no smectite interlayered. They were mainly found as the rock matrix filling primary porosity as vermicular booklets and covering altered k-

feldspar fragments. Kaolinite crystals might have grown in situ probably in shallow burial conditions due to incipient diagenesis (Bauluz et al. 2008).

In claystone layers, kaolinite shows a low crystallinity and a low degree of ordering with anhedral-subhedral rounded morphologies and have some smectite interlayers (Bauluz et al. 2008). This morphology implies that they underwent intense transportation from the source area to the depositional basin, so that they were interpreted as having a detrital origin. XRD features and composition suggest that they were formed by weathering of micaceous or illitic phases in the source area.

CHAPTER 2

2. METHODOLOGY & DATA SET

In this chapter, the state of the art of image spectroscopy is described. Three different data sets were used in this study, spectral data, hyperspectral data, and petrography. Each dataset is divided into acquisition and processing steps.

2.1 IMAGE SPECTROSCOPY

Imaging spectroscopy or hyperspectral imagery is a non-destructive remote sensing technique for mineral identification and mapping, based on electromagnetic radiation reflected from a target (Goetz et al. 1985). When a light photon interacts with any target (in this case a mineral or a rock), light of certain wavelengths is absorbed by electronic and vibrational processes and transmitted at other wavelengths (Van der Meer 1995; Clark 1999; Van der Meer 2004).

The unique way in which light is reflected from each material (mineral or rock), can be used for the identification of specific minerals and lithologies (Clark 1999). In the spectra, the minimum absorption value is related to a specific mineralogy. Other characteristics of the spectra, such as depth, width, or asymmetry are related to the abundance of the mineral (Van der Meer 2004).

Spectral reflectance of rocks depends on their mineral composition and physical properties. Spectral reflectance of minerals are well known (Van der Meer 1995). Many authors have studied the spectral properties of carbonates (Hunt & Salisbury 1970; Gaffey 1987), clay minerals (Bishop et al. 2008; McKeown et al. 2011), iron oxides (Cudahy 1997; Rodger et al.

2012), and hydrocarbons (Hörig et al. 2001; Kühn et al. 2004). Moreover, a U.S. Geological Survey spectral library of minerals, that were determined in the laboratory by a spectroradiometer is available online e.g., Clark et al. (2007) for reference and for image data classification.

The electromagnetic spectral range from 400-2,500 nm comprises the region where iron-, hydroxyl-, sulfate-, water, and carbonate bearing minerals display spectral features. Other minerals, such as quartz or feldspar, do not display any distinctive absorption features in this electromagnetic range (Figure 2-1).

The specific position and shape of carbonate minerals is determined by the metal cations connected to CO_3 and the crystal lattice. In the SWIR region, the most common constituents of carbonate rocks can be identified by prominent absorption feature centered in the wavelength range of: 2,333-2,340 nm for calcite (CaCO_3) and 2,312–2,323 nm for dolomite ($\text{CaMg}(\text{CO}_3)_2$) (Gaffey 1986; Zaini et al. 2014). Calcite reflectance spectra is depicted in red in Figure 2-1.

For iron oxides, electronic processes related to Fe^{3+} octahedrally bonded to ligands of oxygen (hematite) or oxygen and hydroxyl (goethite) creates distinctive absorption features (Haest et al. 2012). Goethite and hematite have crystal field absorptions between 630 to 715 nm and 850 to 1,000 nm, respectively, and a charge-transfer absorption occurs between 480 and 550 nm (Figure 2-1).

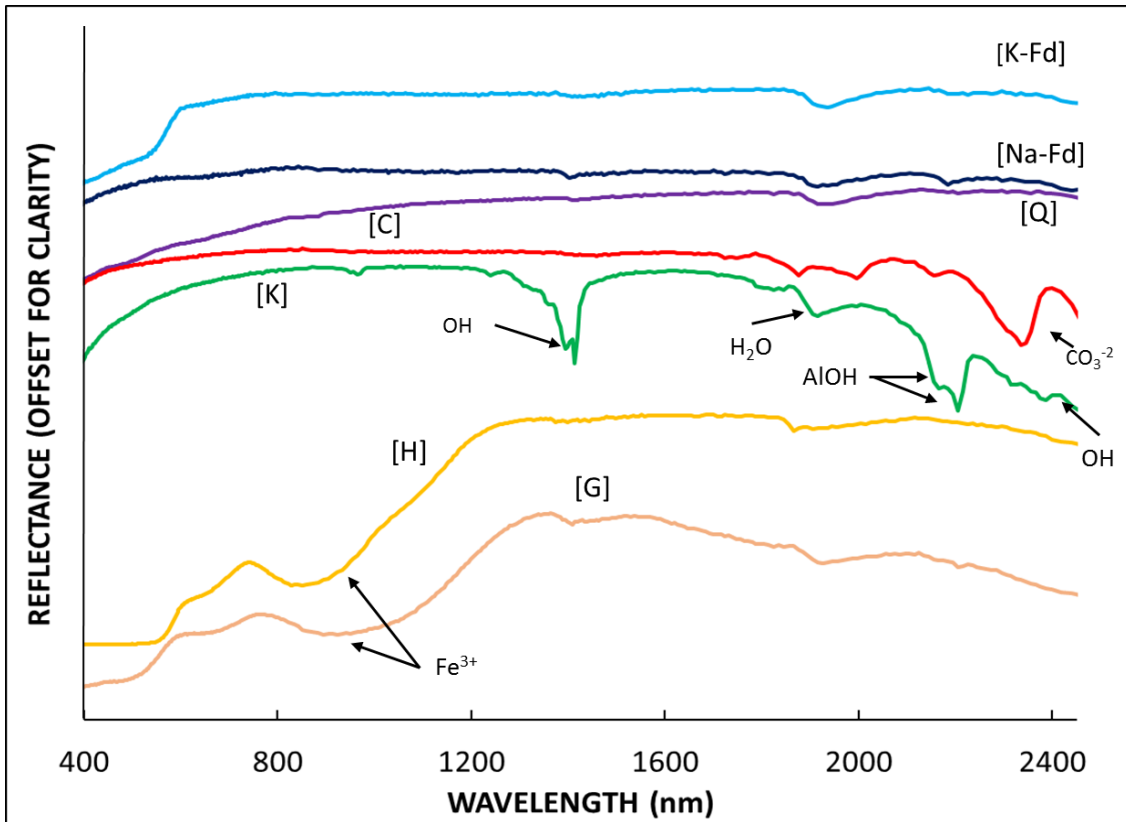


Figure 2-1 Mineral spectra in the VNIR and SWIR area of the electromagnetic spectra. Notice that quartz and feldspars do not show any characteristic absorption features. Data from U.S. Geological Survey spectral Library (Clark et al., 2007)). K-Fd= Potassic Feldspar, Na-Fd= Sodium feldspar, Q= quartz, C= calcite, K= kaolinite, H= hematite, G= Goethite.

Clay minerals (Al-OH clays) can include kaolin group minerals (halloysite, dickite, nacrite, poorly-, and well-ordered kaolinite, white micas such as illite, muscovite, paragonite, brammalite, phengite, and lepidolite, and Al smectite (Meunier 2005). In the spectral range between 2,185 and 2,210 nm, clay diagnostic absorption features occur as a result of a combination of Al-OH bending and OH stretching vibrations. The position and depth of these additional absorption features allow distinction between different kaolin group minerals. Poorly- and well-ordered kaolinite have their minimum absorption feature at $2,208 \pm 3$ nm (Clark et al., 1990; Cudahy 1997; Bishop et al., 2008) and an additional absorption feature between

2,160 and 2,190 nm (Clark et al. 1990) (Figure 2-1 and Figure 2-2). SWIR reflectance spectra was previously used to determine the crystallinity of kaolinite (Zhang et al. 2001; Haest et al. 2012).

White micas have their minimum absorption features at $2,208 \pm 3$ nm, but they do not show a secondary absorption peak, like kaolin group minerals, that allow them to be distinguished from for each other (Figure 2-2). Illite and muscovite reflectance spectra are very similar and very hard to distinguish from each other, that is why they will be considered as micaceous phases (illite and muscovite) (Zhang et al. 2001) (Figure 2-2).

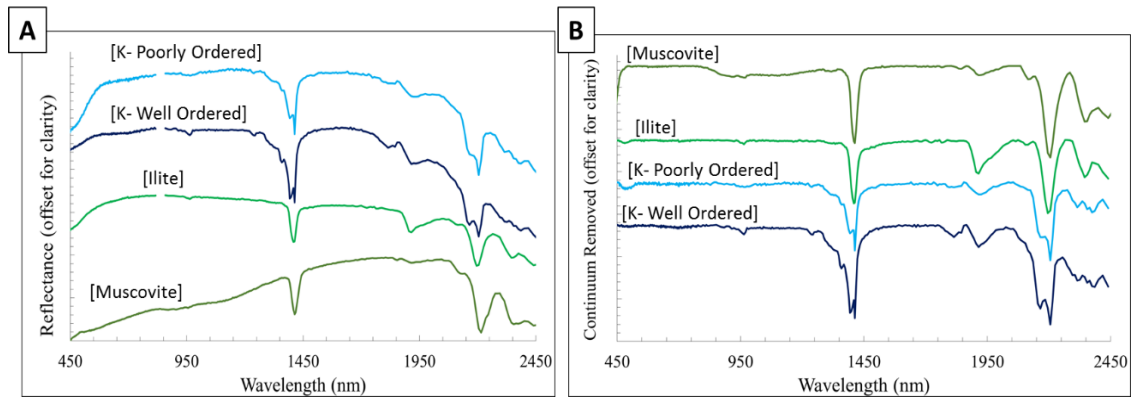


Figure 2-2 Graph showing reflectance spectra vs. wavelength in nm. Data from U.S. Geological Survey spectral library (Clark et al. 2007). (a) Reflectance spectra of poorly-ordered kaolinite, well-ordered kaolinite, and illite. (b) Continuum removed reflectance spectra from the U.S. Geological Survey spectral library of poorly-ordered kaolinite, well-ordered kaolinite, and illite. Abbreviations: [K- Poorly Ordered] =poorly-ordered kaolinite, [K- Well-ordered] = well-ordered kaolinite.

Even though some minerals do not show absorption characteristic in the SWIR (e.g., quartz, feldspar, hematite) their presence can alter the overall spectral response (Figure 2-1). The presence of hematite reduces the overall reflectance and can cause the attenuation of band intensity. On the other hand, glauconite and chlorite show an increasing trend of reflectance (Bowitz & Ehling 2008). Artificial mixtures with quartz-kaolinite-dickite revealed no variance in

the relative intensity and peak position, but a minor decrease in the overall signal when quartz exceeds 98 wt % (Zhang et al. 2001).

Grain-size studies on the characteristics of spectral features of calcite and dolomite revealed spectral changes mainly in the depth of the absorption band and the overall brightness in the SWIR, decreasing with increasing grain size (Gaffey 1986; Zaini et al. 2012). On the other hand, band position, width, and asymmetry do not vary with grain size. In general, coarser grain size, absorb more electromagnetic radiation and therefore, the depth of the absorption increases with increasing grain size (Gaffey, 1987). Recently, Zaini et al. (2012) concluded that the depth of absorption bands increases with increasing grain size in calcite and dolomite samples between 45-250 μm and decreases when the grain size was greater than 250 μm while the overall reflectance decreases with increasing grain size. Absorption depth slightly increases (order of a value of 0.02 (unitless) in the continuum spectra) with grain size fraction between 45-500 μm and slightly decreases when the grain size is greater than 500 μm . On the other hand, asymmetry slightly get more negative with greater grains size (order of a value of -0.005 (unitless) in the continuum spectra) (Zaini et al. 2012).

It is important to keep in mind that image pixels are composed for mixtures of minerals. Variations in percentages presented in a given pixel can change the absorption depth (Van der Meer 2004) and sometimes location (e.g., calcite-dolomite phase) (Zaini et al. 2014). Even though the abundance of a mineral is low, artificial clay mineral mixtures with only ~ 1 wt % were well-resolved with SWIR (Zhang et al. 2001).

2.1.1 Image Spectroscopy in Geological Studies

Satellite and airborne data, as well as laboratory spectroscopy, have been used for over 100 years to obtain mineral composition (Van der Meer et al. 2001). In recent years, more portable hyperspectral cameras are used in the field to map outcrop sections and determine the mineral composition on a centimeter scale for geological characterization (Kurz et al. 2012(a); Petrovic et al. 2012; Murphy & Monteiro 2013; Murphy et al. 2014; Boesche et al. 2015; Okyay & Khan 2016; Snyder et al., 2016). The most recent studies combined Terrestrial Laser Scanning (TLS) to create a photorealistic 3D model that enhances geologic features and facilitates geologic interpretation (Buckley et al. 2013; Kurz et al. 2012(b)).

Kurz et al. (2013) developed a workflow for hyperspectral data acquisition in the field using preprocessing and processing techniques as well as TLS data integration. The technique was tested in carbonate and sandstone outcrops with promising results (Kurz et al. 2012(a)). Murphy and Monteiro (2013) mapped the distribution of ferric iron minerals in a mine using VNIR and SWIR cameras to quantify the relative amount of iron in each area. Denk (2015) mapped by products of the steel industry with close-range hyperspectral techniques. More recently, Okyay & Khan (2016) predicted relative direction of paleoflow in the clastic Wingate Sandstone, Utah. Krupnik et al. (2016) used terrestrial lidar and close-range hyperspectral data to analyze compositional variations in carbonates at very thin scale. Other research groups are studying laboratory specimens and drill core scanning. High accuracy hyperspectral data is acquired in a laboratory setting for mining and oil and gas industry applications (Kruse 1996; Taylor 2000; Bolin & Moon 2003; Kruse et al. 2010; Kruse et al. 2012). In addition, the Geological Survey of Sweden is currently (during 2016) scanning thousands of meters of drill cores in northern

Sweden with VNIR, SWIR, and long-wave infrared (LWIR), to develop a hyperspectral data base complementary to the physical drill cores (<http://www.sgu.se/en/>). Recently, Asadzadeh & de Souza Filho (2016) published a review about the fundamental and advance spectral processing methods for geological remote sensing.

2.2 DATA SET

VNIR and SWIR data were acquired at an outcrop in Raptor Ridge. In addition, ten and six SWIR images were collected for two cores (eight and nine) in the laboratory. In the cores, only the portions that contain the carbonate concretions were scanned. Thirty-seven such areas in core eight and 19 spots in core nine were selected for spectral data acquisition with the spectroradiometer. A systematic sampling was performed every 5-10 cm at the central area of the core, in those portions of the core that were previously imaged by hyperspectral cameras.

At the Utrillas Formation two outcrop walls were scanned with VNIR and SWIR cameras. Thirteen hand-specimens were collected in the field. These samples were scanned in the laboratory with hyperspectral cameras and spectral reflectance data were collected with the spectroradiometer. Thirteen thin sections were prepared and studied.

2.2.1 Spectral Data

2.2.1.1 Data Acquisition

ASD FieldSpec Pro spectroradiometer was used in the laboratory to acquire spectral reflectance data for core samples collected at Raptor Ridge and hand-specimens collected at the Utrillas formation. The spectroradiometer collects 2,151 bands with a spectral bandwidth of 1 nm from 350 to 2,500 nm. Spectra were collected at a distance of 1-5 cm with a broadband

direct-contact light as the light source. The spectroradiometer was calibrated using dark current and a white reference panel (Labsphere®) before data collection (Figure 2-3a).

2.2.1.2 Data Processing

Spectroradiometer results are provided in absolute reflectance. The data were formatted to an excel extension using a program provided by FieldSpec Pro. While the spectroradiometer collects three different measurements, all the results presented here are the average of these three measurements.

2.2.2 Hyperspectral Data

2.2.2.1 Data Acquisition

The field work was carried out during the summer 2015. Ground-based hyperspectral imaging data were acquired from both sites (Frontier Formation and Utrillas Formation) with VNIR Specim V10E sensor for VNIR and SWIR Specim ImSpector N25E (Specim, Finland) (Table 2-1). Two different lenses (OLE 22.5 and OLE56 with a field of view of 24° and 10°, respectively) were used depending on the distance from the camera to the outcrop. The cameras were mounted in a Pan and Tilt rotating stage remotely controlled by the user. The Pan and Tilt Utility software, developed by Middleton Spectra Vision, allows the cameras to move along-track to perform scanning. The image is taken as a push-broom line scanner with the rotation axis parallel to the sensor line (Kurz et al. 2013) and transfer to camera control station (Figure 2-3a).

VNIR camera collects 420 bands from 400 nm to 1,000 nm with a bandwidth of ~1.4 nm. On the other hand, SWIR camera collects 256 bands from 896-2,503 nm with a bandwidth of 6 nm. For calibration purposes, a Spectralon® calibration panel with a 99 % reflectance was placed within sensor's field of view parallel to the outcrop face. For image correction purposes, a

parallel dark image was taken for every image blocking the sensor input, while using the same image parameters.

Table 2-1 Characteristics of VNIR and SWIR Specim[®] cameras (from www.specim.fi).

Hyperspectral image characteristics		
	VNIR	SWIR
Spectral range	<i>394 to 1,000 nm</i>	<i>970 to 2,500 nm</i>
Spectral resolution	<i>2.8 nm</i>	<i>10 nm</i>
Number of bands	<i>840</i>	<i>256</i>
Spatial resolution (Outcrop)	<i>~5 cm</i>	<i>~15 cm</i>
Spatial resolution (Lab)	<i>~0.06 cm</i>	<i>~0.2 cm</i>

Hyperspectral images are affected by illumination conditions and measurement at-sensor radiance can be influenced by the illumination angle, adjacency, shadowing, and temporal effects (Kurz et al. 2013; Murphy et al. 2014). For optimal oblique illumination, the scanning device should be perpendicular to the outcrop face and the sun (light source) should be at a minimum angle with respect to the outcrop wall (Figure 2-4). Furthermore, tilted and/or close-by-scan positions can lead to distorted pixels at the edge of the images. For more information about optimal data collection refer to Kurz et al. 2013. Variability in moisture created by precipitation (previous days rainfall) or running water could cause classification problems (Murphy et al. 2012).

Consequently, field work campaigns were planned in advance, taking into account the outcrop direction, vertical component (e.g., Google Earth and Digital Elevation Model (DEM) data), sun azimuth and solar elevation (<http://www.noaa.gov/>).

At Raptor Ridge the cameras were set ~50 m from the outcrop wall. The pixel size was 5 cm and 15 cm for VNIR and SWIR, respectively. At the Utrillas Formation, two scanned positions

were set at ~25 m from the outcrop wall. The pixel size was 5 cm and 15 cm for VNIR and SWIR, respectively (Figure 2-3b).

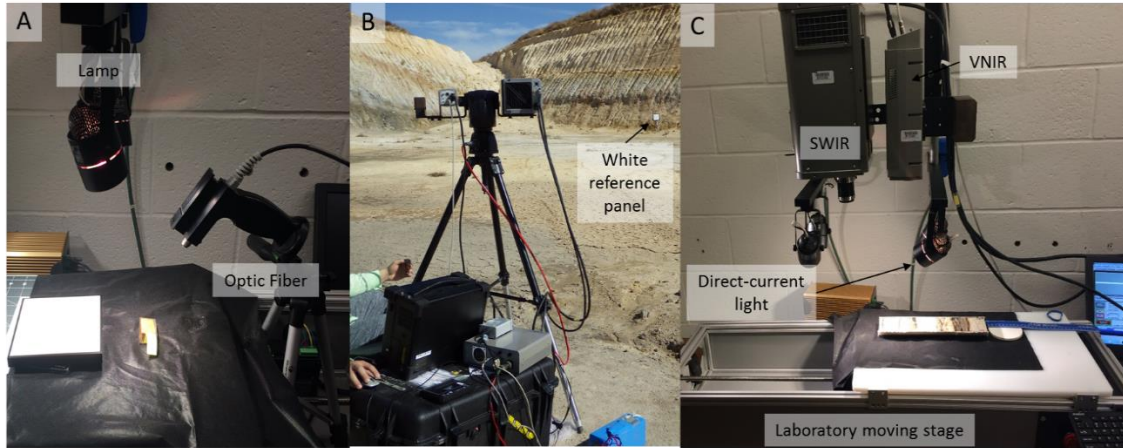


Figure 2-3 Data acquisition methods. (a) ASD FieldSpec Pro spectroradiometer. (b) VNIR and SWIR cameras mounted in the Pan and Tilt rotating stage for outcrop scanning at the Utrillas Formation. The cameras were faced perpendicular to the outcrop. Notice the white reference panel parallel to the outcrop face. (c) Laboratory scanning system for core and rock samples. SWIR and VNIR cameras were fixed while the remotely controlled moving stage, which allows the samples to go through the scanning area.

The same cameras were installed in a custom laboratory configuration to scan the cores from Raptor Ridge and hand samples from the Utrillas Formation. The imaging sensor was configured to record continuous spectra at a high spatial resolution of 0.06 mm and 0.2 mm for VNIR and SWIR, respectively. Rock samples were scanned on a moving stage at a distance of about ~35 cm. Hyperspectral cameras were remotely controlled by a PC and the data was acquired under similar illumination conditions created by a four direct-current bulbs perpendicular to the scanned area. For every image a calibrated white reference panel was scanned for calibration purposes (Figure 2-3c).

Approximately, 3.5 m of core eight and 2 m of core nine from Raptor Ridge and 13 representative rock samples from the Utrillas Formation were scanned in the laboratory.

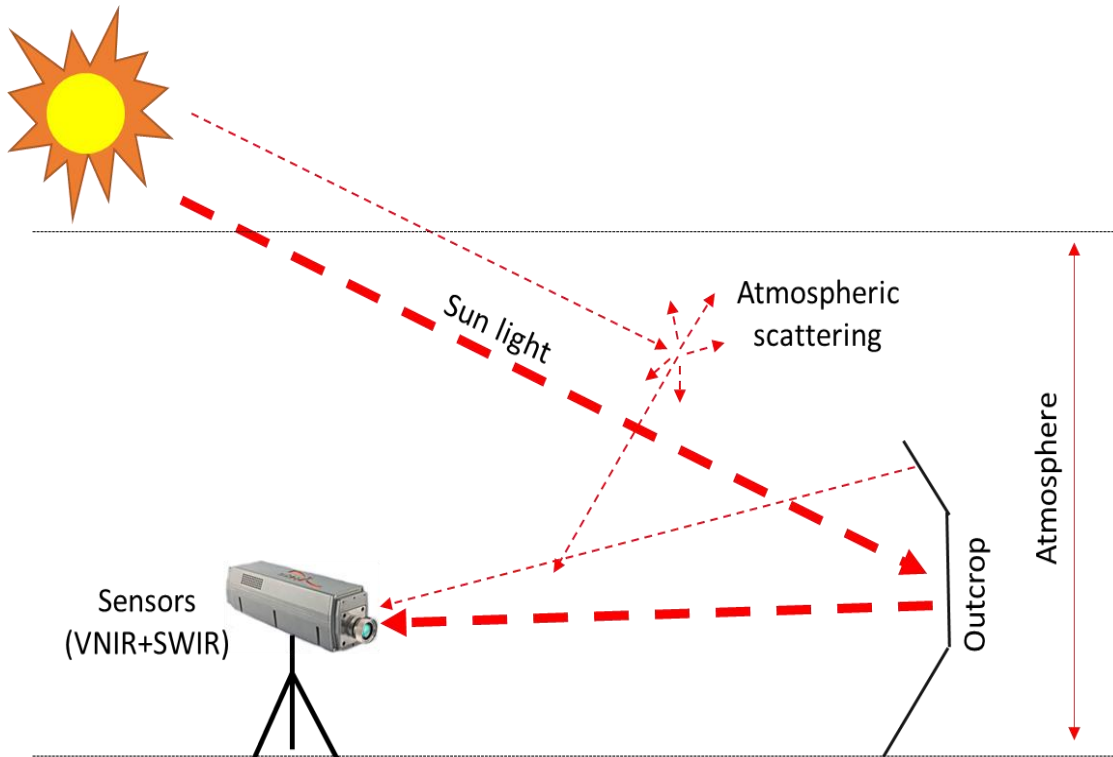


Figure 2-4 Optimal scanning position for ground-based imaging spectroscopy. Wider dash lines show the direct light path. Thinner red dashed lines correspond to reflected and/or scattered light from adjacent surfaces and/or atmosphere (after Kurz et al. 2013).

2.2.2.2 Data Processing

There is no standardized method for processing ground-based hyperspectral remote sensing data (Asadzadeh & de Souza Filho 2016). Some preprocessing steps should be performed to the hyperspectral images to remove noise and atmospheric distortions and convert the raw image from at-sensor radiance into reflectance values. The steps for data preprocessing are summarized in Figure 2-5. After these preprocessing steps, the resulting image was classified using different methods to produce a better understanding of the mineral composition and/or lithology of the outcrop and laboratory samples. For preprocessing and processing purposes, standard tools available in Environment for Visualizing Images (ENVI® versions Classic and ENVI

5.1[®] Harris Geospatial Solutions, previously Exelis Visual Information Solutions) software was used, as well as in-house solutions developed in the Matlab 2014 (Mathworks Inc.).

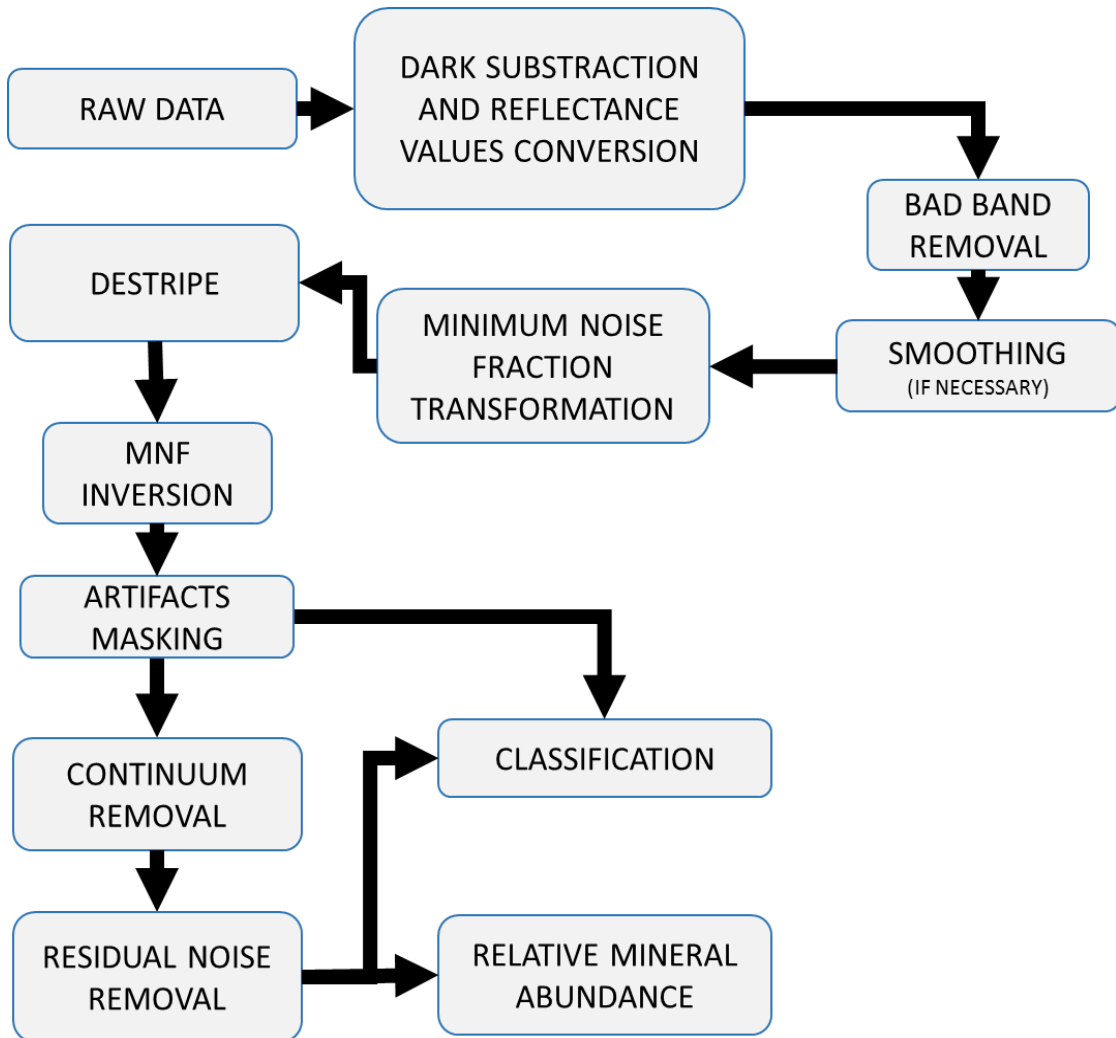


Figure 2-5 Workflow diagram for hyperspectral image preprocessing and steps used in the ongoing research.

The raw hyperspectral images must be corrected to at-sensor radiance. Dark current was subtracted from the image data using an in-house developed code. This process removes the atmospheric scattering by subtracting a pixel value that represents the background for each band (ENVI Help). Empirical Line Calibration (ELC) was applied to convert the radiance data into

relative reflectance images and atmospheric corrections (i.e., solar irradiance and atmospheric effects) (Kurz et al. 2013). Each band digital numbers (DN) were equated to reflectance by a linear regression (ENVI Help). Image spectra were obtained from the center of the calibration panels in the image and matched with the absolute reflectance of the panels measured with the spectroradiometer under laboratory conditions.

Atmospheric gases (N₂, CO₂, O₂, H₂O etc.) absorb radiation in certain bands of the electromagnetic spectrum, known as atmospheric absorption bands which create distortion and spectral noise. The biggest atmospheric absorption bands range between 950-1,200 nm, 1,340-1,500 nm, 1,800-2,050 nm, and 2,356- 2,500 nm. These areas of the spectra were masked as bad bands in all images.

Savitzky-Golay filter was run to smooth the data and remove the remaining noise in the spectra (Savitzky & Golay 1964). A greater filter width produces the smoothest results. In general, the better results in terms of smoothing and data quality were obtained when the parameters were set as filter width of 2 and a 3 polynomial degree.

Minimum Noise Fraction (MNF), (Green et al. 1988), is a linear transformation that decorrelates spectral bands and separates random noise from the image data in order to increase image quality and maximize the signal to noise ratio (Kurz et al. 2013). Spatially, coherence bands and those that show eigenvalues greater than 3, were used for further processing. In contrast, equal and near unity (and < 3) eigenvalues were interpreted as noise bands. For most of the VNIR and SWIR analyzed images, the first 10-20 components appear to be spatially coherent and were selected.

Destripe was applied to the MNF result to remove periodic scan-line stripping in the images. The mean of every n th line was calculated and normalized to its respective mean (Envi Help).

After MNF transformation, an inverse transformation was applied to create a noise free image with minimum disturbance. The resulting MNF inversion created an image that was used to directly compared to the spectral libraries.

Visualization of different MNF in Red-Green-Blue (RGB) images was used for preliminary interpretations of the data. The areas that were highly affected by shadows and any other part of the image that was not part of the targeted outcrop (e.g., vegetation, fallen blocks, shadows, and over exposed areas) were masked and excluded from subsequent processing. A semi-automated process was applied for pixel masking. Mask bands were created using MNF bands that enhanced different materials and light conditions such as vegetation or shadows (Diana Krupnik personal communication). For optimal results, a closer look and manual masking were performed using a Region of Interest (ROI).

2.2.2.3 Image Classification

Many peer-reviewed papers compared different classification techniques and applied them to hyperspectral imaging (Rojas et al. 2010; Murphy et al. 2012; Zaini et al. 2014; Schneider et al. 2014; Asadzadeh & de Souza Filho 2016). In this section, a brief summary of these techniques is provided.

There are different algorithms to categorize pixels in an image. Spectral processing techniques have been divided into knowledge-based approaches and data-driven approaches. Reference data is not required in the knowledge-based approaches, whereas in data-driven approaches the spectra of a pixel is defined by the user using endmembers (Asadzadeh & de

Souza Filho 2016). Endmembers are the reference spectra of each classification category depending on the chemical composition of the object of study (e.g., in an outcrop image sandstone and claystone spectra can be endmembers).

From the knowledge-based category, band ratios and continuum removal were used for preliminary results visualization because of their simplicity and convenience.

Band ratios, which highlight the spectral differences between bands, can be used for a first look at the data and endmember selection. One advantage of using the band ratio is its invariance to shadowing which is constant in all of the bands (Zhouyu et al. 2006; Asadzadeh & de Souza Filho 2016). Although band ratios are widely used in multispectral images with great success, this method does not have the same acceptance in the hyperspectral field due to sloping spectra and atmospheric heterogeneities. Usually, the bands applied to band ratios are chosen from observation from previous knowledge. Hyperspectral bands are narrow, therefore, at the target spectra range areas, 3 or more consecutive bands are added in order to highlight the specific absorption features.

To highlight carbonate concretions in Raptor Ridge the following formulas were applied using the three images created.

- $(B_{2328}+B_{2334}+B_{2322})/3$ (a)
- $(B_{2152}+B_{2159}+B_{2171})/3$ (b)
- $(B_{2196}+B_{2203}+B_{2209})/3$ (c)

The B_{xxx} corresponds to the selected band wavelength (in nanometers). Only the band ratio that enhances spectral differences the best is presented and corresponds to: (a)/(b). The ENVI code used for band creation is:

- $\text{float}((b1) + \text{float}(b2) + \text{float}(b3))/3.0$ (ENVI code) (1)

To highlight the spectral differences in the Utrillas Formation the following band ratio formula was applied:

- (B_{2171}/B_{2152}) (d)
- (B_{2203}/B_{2171}) (e)
- (B_{2159}/B_{2171}) (f)

The continuum removal methodology allows a comparison between different characteristics of absorption features related to mineral abundance. The reflectance spectrum can be divided in three basic components, (a) a continuum (also known as “hull”), (b) absorption bands, and (c) residuals or noise (Asadzadeh & de Souza Filho 2016).

The continuum is described as the overall albedo of the reflectance curve and it is considered to be the manifestation of non-selective multiple scattering and the presence of spectrally inactive minerals (e.g., microcrystalline quartz) (Asadzadeh & de Souza Filho 2016). The continuum can be effectively removed and scaled (normalized) to 100 % (Figure 2-6). After this continuum is removed, the description of absorption feature characteristics such as: depth, width, and asymmetry can be used to determine relative abundance and/or grain size changes (van der Meer 2004; Bell et al. 2010; Zaini et al. 2012).

Continuum removal methodology provides better results when applied just to areas of the spectra where absorption features are located (Asadzadeh & de Souza Filho 2016).

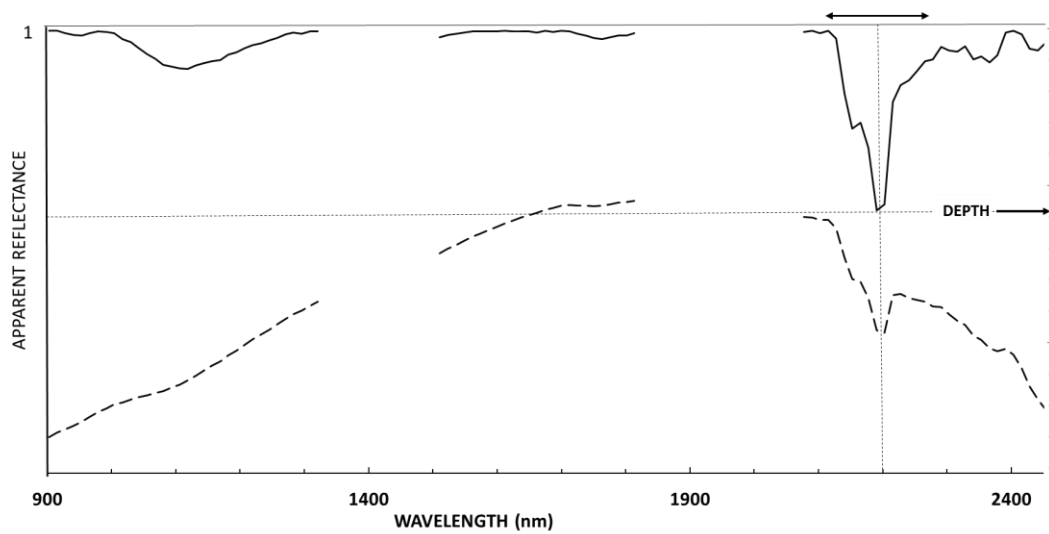


Figure 2-6 Definition of the continuum removal and absorption features characteristics. The spectra were extracted from the SWIR hyperspectral image at Raptor Ridge, after bad bands removal (after Van der Meer 2004).

The position of absorption bands are defined as the wavelength at the position of maximum absorption, hence where the minimum reflectance of an absorption feature occurs (Figure 2-1) (Van der Meer 2004; Zaini 2009).

The depth (D) of the absorption feature corresponds to the reflectance value at the shoulders (in normalized data equals to 1) minus the ratio of reflectance value at the position of the absorption wavelength, R_b is the reflectance at the band bottom and R_c is the reflectance of the continuum at the same band as R_b (Figure 2-6) (Van der Meer 2004; Zaini 2009).

- Depth (D) = $1 - (R_b/R_c)$ (g)

The width of an absorption features, is defined as the sum of the area left (A_{left}) of absorption position and the area right (A_{right}) of absorption position and divided by two times the depth value of the feature (Figure 2-6) (Van der Meer et al. 2004; Zaini 2009).

- $Width = (A_{left} + A_{right}) / 2D$ (h)

The asymmetry of absorption band, (S), represents the ratio of the area left (A_{left}) of the absorption position to the area on the right (A_{right}) (Figure 2-6) (Van der Meer 2004; Zaini 2009).

- $Asymmetry (S) = (A_{left} / A_{right})$ (i)

From the data driven spectral processing techniques, Spectral Angle Mapper (SAM) (whole pixel analyst), and Mixture Tuned Match Filtering (MTMF) (sub-pixel analyst) were used and compared in VNIR and SWIR images.

SAM is a physical-based spectral classification technique that defines the similarity between the image spectra and the given reference spectra. SAM treats the spectra as n -dimensional vectors, where only the direction of the vectors is important and not its length. Therefore, grain-size differences in the dataset will not affect the resulting spectral angle (Hecker et al. 2008). Smaller angles will represent closer matches to the reference spectra and will be classified together (Envi Help; Van der Meer et al. 2001). The rule image is provided as a result of the SAM classification and depicts the difference in angle between the image spectrum and the reference spectrum. Darker pixels represent lower angles and consequently more similar spectra. The rule image can be used for reclassification purposes using different angle thresholds for each endmember.

Some peer reviewed papers applied the SAM algorithm for close-range hyperspectral image classification (Murphy et al. 2012; Denk et al. 2015; Okayay & Khan 2016).

One of the main weakness of the SAM classification algorithm is that rather than taking into account the shape of the individual absorption features, the result is an average fit over the entire spectral range of the dataset. Therefore, it cannot be determined if the contributing factor to spectral angle was a mismatch in the distribution of absorption features or the entire spectrum has a slight mismatch in all bands. Furthermore, it is susceptible to additive effects, general tilting, and wavelength shifts in the spectra (Hecker et al. 2008). Although SAM classification methods are indifferent to illumination variations, recent studies suggested that optimal spectral angle classification varies depending on the rock type and different shadow conditions. Therefore, no single reference spectrum can be selected as a “definite” spectrum for each class, nor a single angular threshold (Murphy et al. 2012). Moreover, it is very difficult to construct a spectral library of shadowed spectra because their shape will be determined by the particular environmental conditions under which they were collected (atmospheric and surrounding structures) (Murphy et al. 2012).

MTMF classification is a combination of both classification methods: LSU and statistical Matched Filtering (MF). Consequently, it has the ability to map a single known endmember without any information about the rest of the image (Boardman 1998). MTMF output images are a set of images that represent MF scores and the infeasibility scores for each pixel related to the spectra of the endmember. MF output images help to estimate the abundance of that endmember in the image that is related to the relative degree of match to the reference spectrum. Every resulting pixel has a number from 0 to 1, 1 representing the perfect match (Envi Help). The infeasibility image is used to reduce the number of false positives. Pixels that contain

high infeasibility values are likely to be MF false positives (Envi Help). MTMF greatly increases the detectability and selectivity, compared to other classification methods. In order to increase the efficiency in the processing, it should be performed in the coherent MNF bands (Kurz et al. 2013). One of the drawbacks of this classification technique is the difficulty of finding pure endmembers in the image. Many researchers applied the MTMF algorithm for close-range hyperspectral image classification (Kurz et al. 2008; Kurz et al. 2009; Kruse et al. 2010; Kurz et al. 2012(a); Kurz et al. 2012(b); Kurz et al. 2013).

For classification purposes, a threshold of 0.5 for MF results was picked in order to select pixels with greater matches. Moreover, only pixels with less than 30 infeasibility values were selected to reduce false positives in classification. For that purpose, a mathematical expression was run on the MTMF results.

- $(b1 > 0.5 \text{ and } b2 < 30) * 1$ (Envi Code) (3)

In Figure 2-7 MF scores vs infeasibility results from MTMF results for Raptor Ridge were plotted as an example. Only pixels that fall into the red rectangle were taken into account for classification.

The “Kaolinite-Crystallinity-Index” (KCI) and the “Micaceous Phase Abundance Index” (MPAI) at the Utrillas Formation were developed to classify the image into four different endmembers depending on the kaolinite vs. micaceous phase content.

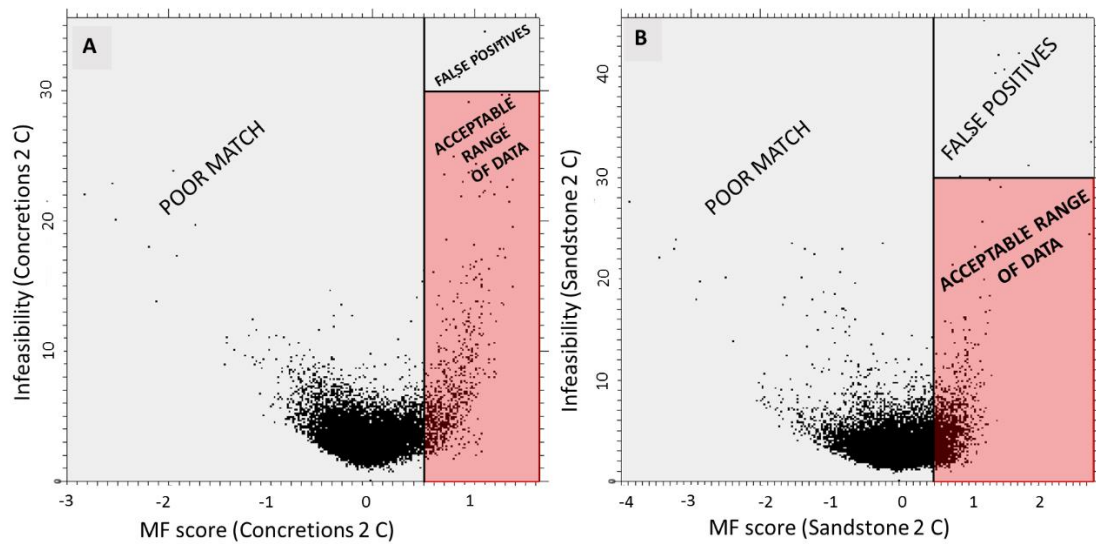


Figure 2-7 Scatter plots for the MTMF results showing MF score in X-axis and infeasibility results in Y-axis. Pixels that have MTMF scores greater than 0.5 and infeasibility values smaller than 30 were used and plotted in the red rectangle. The rest of the classified pixels were not taken into account. (a) Scatter plot showing Mf scores vs. Infeasibility results for the concretions endmember in Raptor Ridge. (b) Scatter plot showing Mf scores vs. Infeasibility results for the sandstone endmember in Raptor Ridge.

The KCI is applied to the SWIR normalized spectra between 2,100 nm and 2,400 nm in order to separate well-ordered kaolinite from poorly-ordered kaolinite:

- $(B_{2159\text{nm}} - B_{2165\text{nm}}) * 10$ (j)

The B_{xxx} correspond to the band wavelength (in nanometers) selected.

The MPAI is applied to the KCI results in order to divide areas with well-ordered kaolinite with variable abundance of micaceous phase and poorly-ordered kaolinite with variable abundance of micaceous phase. The expressions used for each endmember are (Results section Figure 4-6):

- Poor-ordered kaolinite + micaceous phase high % \rightarrow (g) greater than 0.04 and $B_{2,271\text{ nm}}$ less than 0.998.

- Poor-ordered kaolinite + micaceous phase mica low % → (g) greater than 0.04 and $B_{2,271nm}$ equal to 1.
- Well-ordered kaolinite + micaceous phase high % → (g) less 0.04 and $B_{2,271nm}$ less than 0.0998.
- Well-ordered kaolinite + micaceous phase low % → (g) less 0.04 and $B_{2,271nm}$ equal to 1.

Every classification methodology performed better with different spectral extraction approaches. There were four different ways to select the endmember data before classifying an image:

- (a) Spectra collected from the image itself (using ROI's) and based on field-work data and previous knowledge.
- (b) Spectral data collected from the core data at the laboratory stage and applied to outcrop data.
- (c) Spectra collected with the spectroradiometer from cores.
- (d) Previously published spectral data from U.S. Geological Survey spectral library (<http://speclab.cr.usgs.gov/spectral-lib.html>)

As a way to minimize classification errors, it is recommended to select the endmember spectra from the image itself (Hecker et al. 2008). However, the endmember selection depends on the purpose of the classification. During this work four methodologies were tested and the best results are presented.

2.2.3 Petrography

For the thin section description, a Nikon Eclipse LV 100POL and binocular microscopes were used. The microscope is attached to a Nikon DS-Fi1 digital camera connected to a computer for

image collection. A LEICA DM 750 P, attached to a fixed stage was used for point counting (~200 points per sample) following the methodology of Chayes (1956). Based on Folk (1974) the error was estimated in 2 %.

CHAPTER 3

3. RESULTS: THE FRONTIER FORMATION

In this section, the results of spectral data and hyperspectral outcrop and laboratory images from Parasequence #6 of the Raptor Ridge are presented. In Figure 3-1a and Figure 3-2a photographs of core eight and core nine are shown. In Figure 3-4 the scanned outcrop at Raptor Ridge is depicted.

3.1 SPECTRAL DATA

The reflectance spectra of the five different facies that comprise the Raptor Ridge outcrop have specific physical and chemical characteristics that allow them to be distinguished. In Figure 3-1 b, c, d, e & Figure 3-2 b, c, d the reflectance spectra of different lithologies found in the Raptor Ridge deltaic wedge is depicted. They were divided into, bar facies, channel facies, carbonate concretions in bar facies, carbonate concretions in channel facies, and distal facies. However, sometimes the similarity between facies (similar composition and slight changes in grain size) showed similar reflectance and hence difficult to distinguish apart. In general, when calcite was present, the overall reflectance at the VNIR part of the spectra increased (e.g., Figure 3-2 d). The overall spectra reflectance for channel facies was slightly lower than bar facies, probably this is related to a slightly larger grain size.

Sandstone framework constituents, quartz and feldspar, have no distinctive absorption features in VNIR or SWIR. On the other hand, cement constituents, such as kaolinite and calcite, show distinguishable characteristic absorption peaks. Although chlorite was previously described as a cement phase (Nyman et al. 2014), its presence is not observed in the spectral data. Zhang et al. (2001) reported erroneous results for spectroscopy analysis in rocks with

chlorite due to dark a color and hence lower signal to noise ratios, low precision, and high detection-limits.

A closer look of the specific parameters (e.g., depth, width, and asymmetry) of the reflectance spectra of kaolinite and calcite (major cement constituents), in the SWIR wavelength region is shown in Figure 3-3. The red and green line correspond to calcite and kaolinite reflectance parameters, respectively. Blue and red rectangles are correlated with carbonate concretions in channel facies and bar facies, respectively.

The depth of the absorption peak is related to mineral abundance. Additionally, physical properties such as grain size reduce the overall reflectance spectra, as it happens in channel facies, where the grain size was described as medium sand (Gani & Bhattacharya 2007) (Figure 3-1 and Figure 3-2). Changes in grain size can alter the width, while asymmetry is invariant.

There are two strong absorption features one at 1,365-1,435 nm and the other one at 1,851-2,064 nm that are related to OH⁻ and OH⁻/H₂O absorption (Clark et al. 1990). These areas of the spectra were removed. Two small absorption peaks were seen around 480 nm and 890 nm (Figure 3-1 and Figure 3-2).

The presence of absorption features at 480-550 nm, and 850-1,000 nm has been previously related to hematite (Haest et al., 2012). These absorption features were found in all the core measurements but are more prominent in the carbonate concretions.

The absorption feature located at around 2,200 nm is characteristic of clay minerals (Clark et al., 1990; Haest et al. 2012) (Figure 3-1 and Figure 3-2). These absorption peaks can be found in both the sandstone host rock (bar and channel facies) and in the carbonate concretions, but depth absorption was smaller in the concretions (Figure 3-3). Additionally, this drop, in

combination with a smaller peak at 2,165 nm, creates a doublet that is characteristic of well-ordered kaolinite. This doublet is slightly prominent in the bar and channel facies than the distal facies and carbonate concretions. Kaolinite show two smaller absorptions at 2,321 and 2,381 nm. As shown in the graphs (Figure 3-3), the width of kaolinite absorption was relatively constant along the measured sections. The position of the absorption minimum remains constant along the core section at ~2,005 nm. The depth of the peak at ~2,005 nm in the carbonate concretions decreases, meaning that the kaolinite abundance is lower (except, in core eight points: 115 & 116). Apart from, some anomalies in the host rock (i.e., in core eight points: 66 & 95), the asymmetry of the 2,005 nm peak was relatively constant with a standard deviation of 1.12.

Calcite is characterized by absorption features at around ~2,000 nm, ~2,335 nm and ~2,550 nm (Gaffey 1987; Clark et al. 2007). However, both the interaction with other mineral absorption peaks (e.g., at 2,000 nm with clay minerals) and spectral range availability (from 1,000 nm-2500 nm) allowed only the use of the absorption minimum at 2,335 nm as the main distinctive absorption feature. The width of the absorption minimum for calcite was similar for both types of concretion with major peak anomalies found at the edges of concretions (e.g., in core eight points: 35 & 66). The depth of the peak at ~2,335 nm was homogeneous along the concretion transect. The asymmetry of calcite was slightly reduced at the edges of concretion (i.e., in core eight points: 41, 66 & 78) (Figure 3-3). Overall, the absorption position varies from 2,333 nm to 2,335 nm (Figure 3-3).

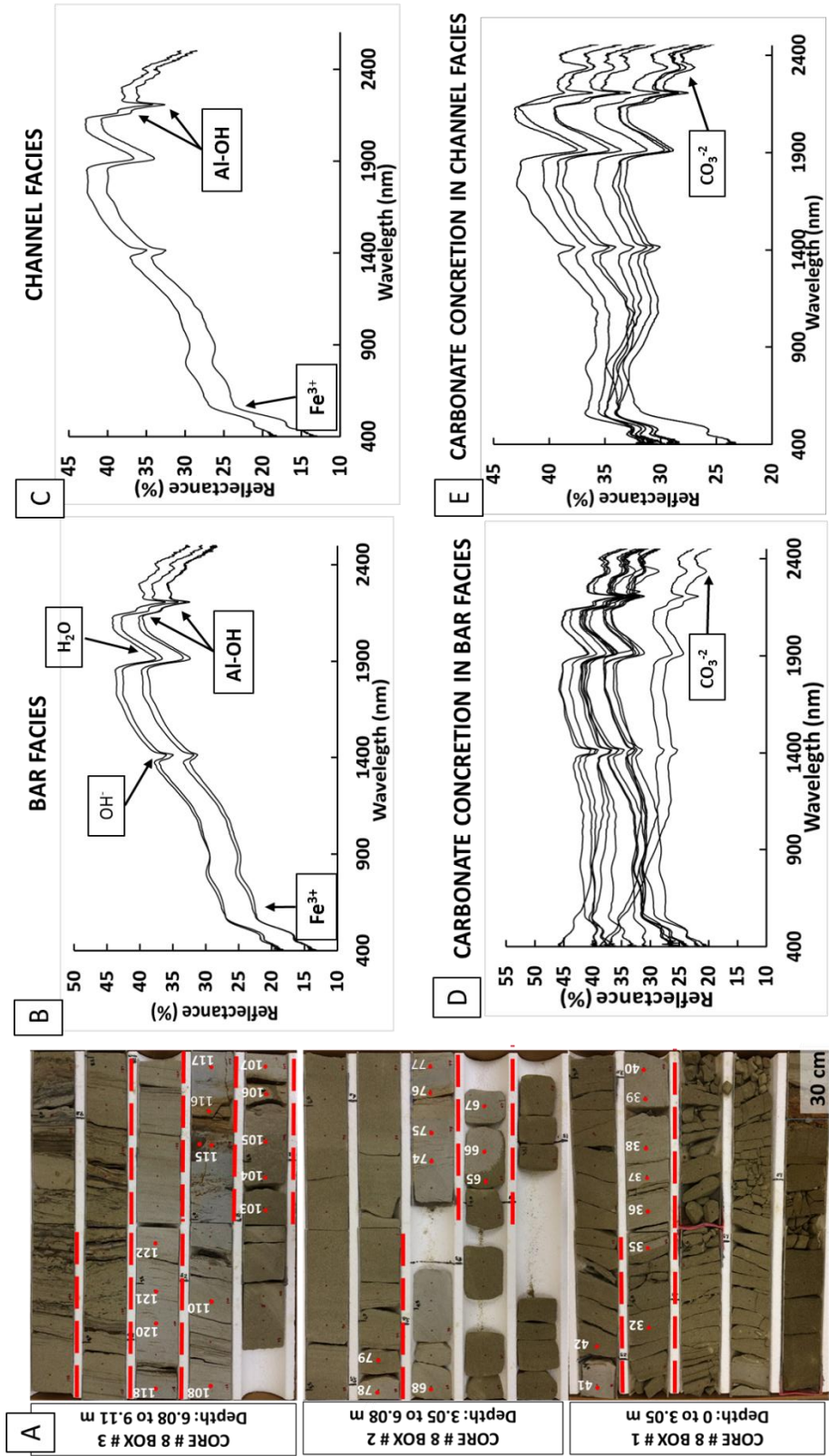


Figure 3-1 (a) Photographs of three of the four boxes of core eight from Raptor Ridge. Red points correspond to areas where spectral data were collected. Red dashed lines correspond to areas that were imaged by hyperspectral cameras. (b, c, d, and e) Graph displaying spectral reflectance data (in percentage) vs. wavelength (in nanometers) collected from selected spots on core eight shown in red dots from Figure 3-1a. Each graph corresponds to points collected in b-bar facies, c-channel facies, d-carbonate concretions in bar facies, e-carbonate concretions in channel facies. Main absorption peaks are depicted.

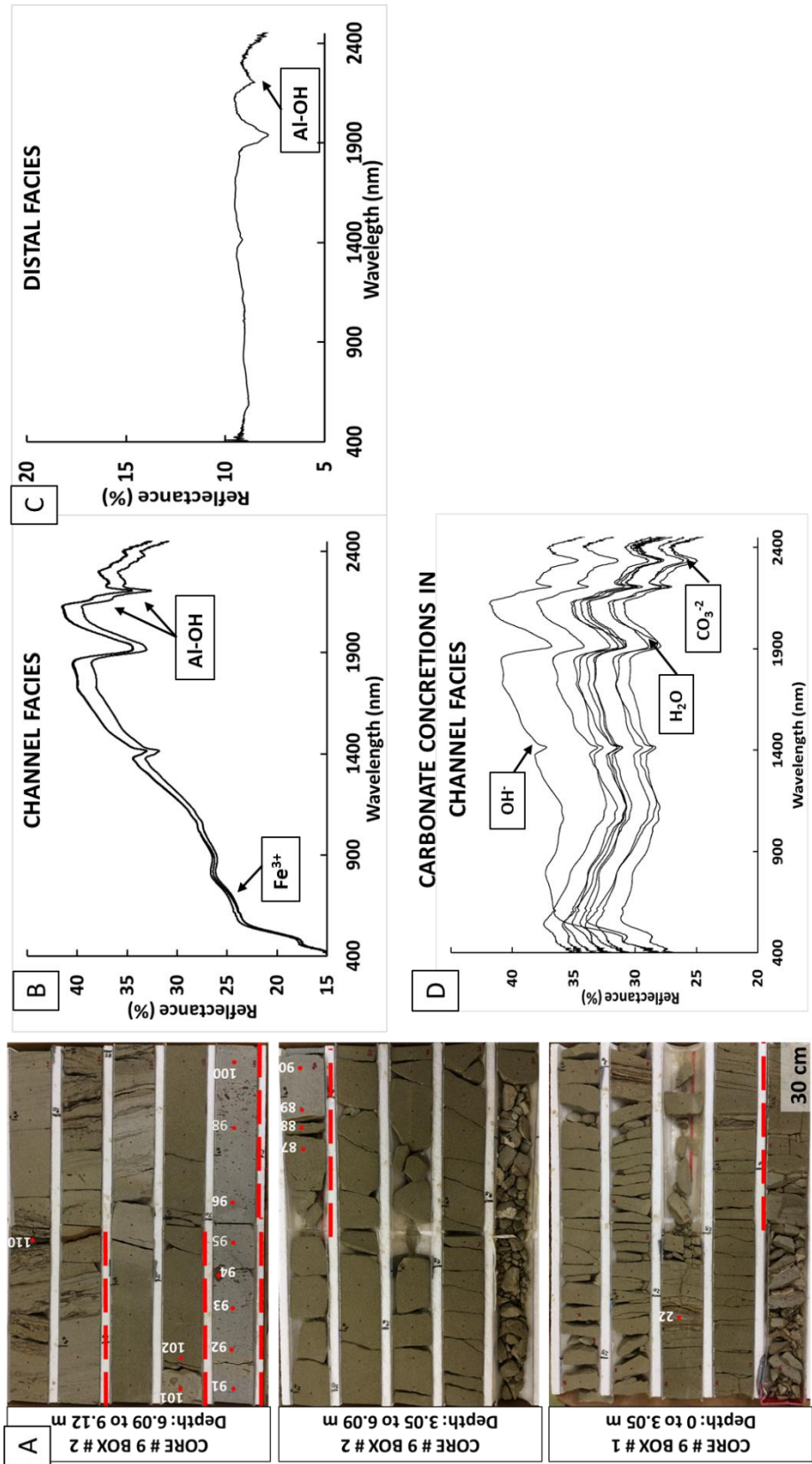


Figure 3-2 (a) Photographs of three of the four boxes of core nine from Raptor Ridge. Red points correspond to areas where spectral reflectance data were collected. Red dashed lines correspond to areas that were imaged by hyperspectral cameras. (b, c, and d) Graph displaying spectral reflectance data (in percentage) vs. wavelength (in nanometers) collected from selected spots on core nine shown in red dots from Figure 3-2a. Each graph corresponds to points collected in b-bar facies, c-channel facies, d-carbonate concretions in bar facies. Main absorption peaks are depicted.

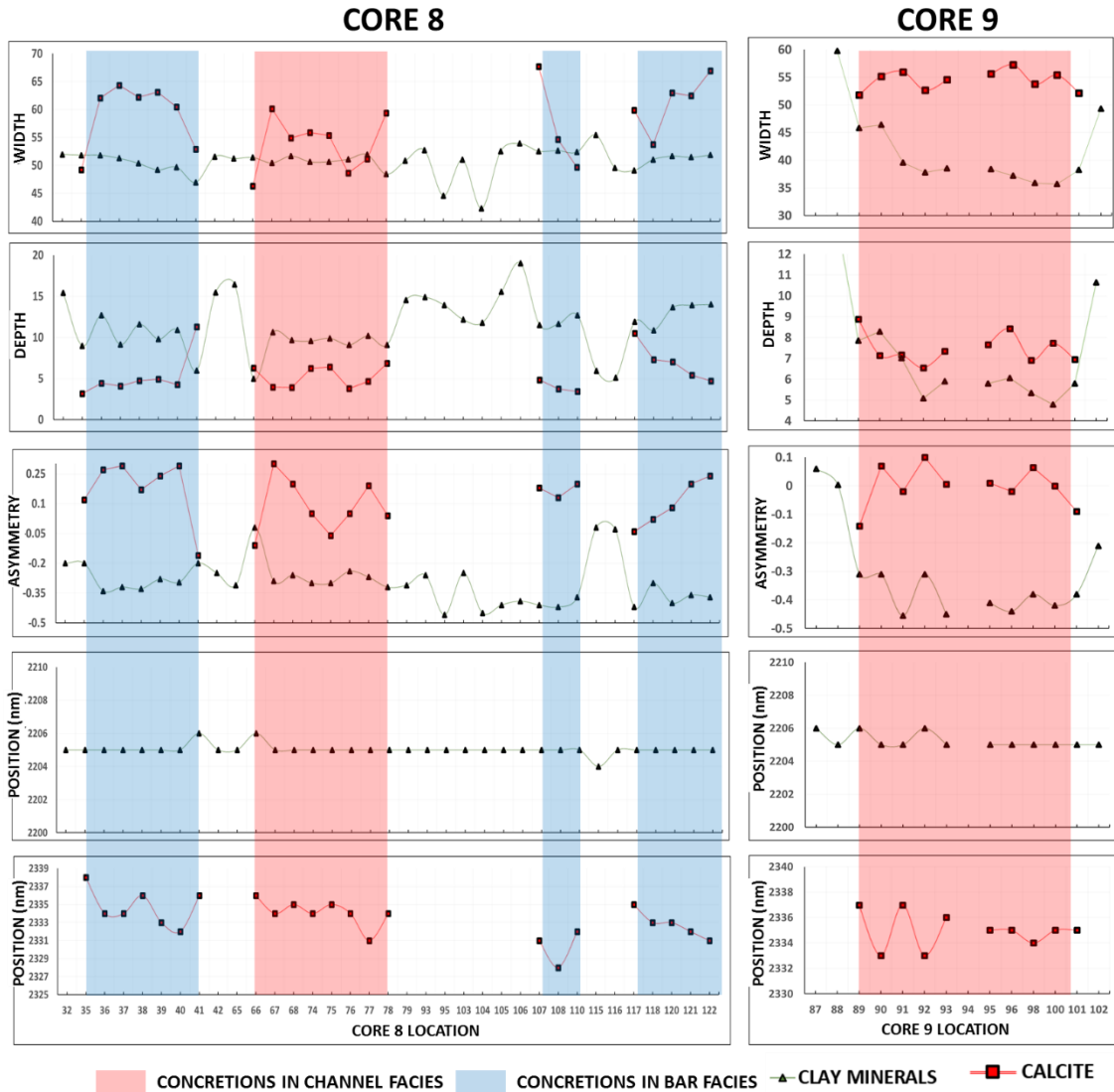


Figure 3-3 SWIR absorption features of clay minerals and calcite in spectral data collected in different point of core eight and core nine. For location refer to Figure 3-1 and Figure 3-2. The red rectangles and green triangles correspond to calcite and kaolinite reflectance parameters, respectively. Blue and red areas correlate with carbonate concretions in channel facies and bar facies, respectively.

3.2 HYPERSPECTRAL DATA

Different approaches and classification methods were employed for classifying SWIR images of the core and outcrop data. Based on Gani & Bhattacharya (2007) and Lee et al. (2007) facies

associations description and field outcrop observations, 4 endmembers were selected: channel facies, bar facies, carbonate concretions, and distal facies (Figure 3-4, Figure 3-6a, & Figure 3-7).

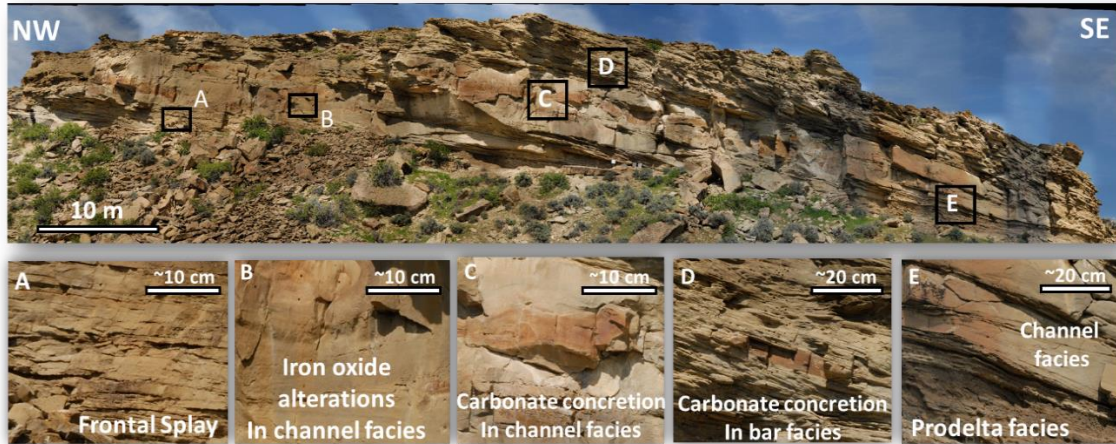


Figure 3-4 Photomosaic (resolution of ~ 0.5 cm) image depicting different endmembers selected for classification purposes. Endmembers were selected based on field observations, previous geological studies and spectral analysis. (a) Frontal splay deposits. (b) Iron oxide surface alterations. (c) Carbonate concretions and channel facies. (d) Bar facies. (e) Channel facies and prodelta facies.

3.2.1 Imaging of Core Samples

Core-eight and core-nine were only scanned with the SWIR camera where calcite concretions were located. In total 18 SWIR images were acquired, these were preprocessed and classified using different methodologies. The photograph of the core is shown in Figure 3-5a.

Figure 3-5b depicts a false color SWIR image with spectral bands 2,195 nm, 2,334 nm and 2,152 nm displayed as RGB. As a preliminary observation, carbonate concretions are displayed in pink and host rock sandstone (bar facies and channel facies) in green.

The SAM classification technique, using the U.S. Geological Survey spectral library from calcite and kaolinite, is depicted in Figure 3-5c. In this case, areas where calcite is present are shown in red and areas with kaolinite in green. Black pixels correspond to unclassified pixels.

The angular similarity threshold was always lower than 0.075 radians and has been varied for every endmember.

In addition, normalized spectra using the continuum removal technique was used to reflect the relative abundance of kaolinite and calcite over the cores. The depth of the absorption minimum at ~2,203 nm (characteristic of clay minerals) and ~2,334 nm (characteristic of calcite) is shown in Figure 3-5d & e. Clearly both methodologies allow distinction between carbonate concretions and the sandstone host rock and results were comparable.

Results of core image analysis revealed that the calcite cement in channel facies was homogeneously distributed from the edges to the center of the concretions, whereas, calcite cement at the concretions located in proximal and distal bar facies was less homogeneous and show interbedded thin layers of non-calcite cemented sandstone, where kaolinite was more abundant.

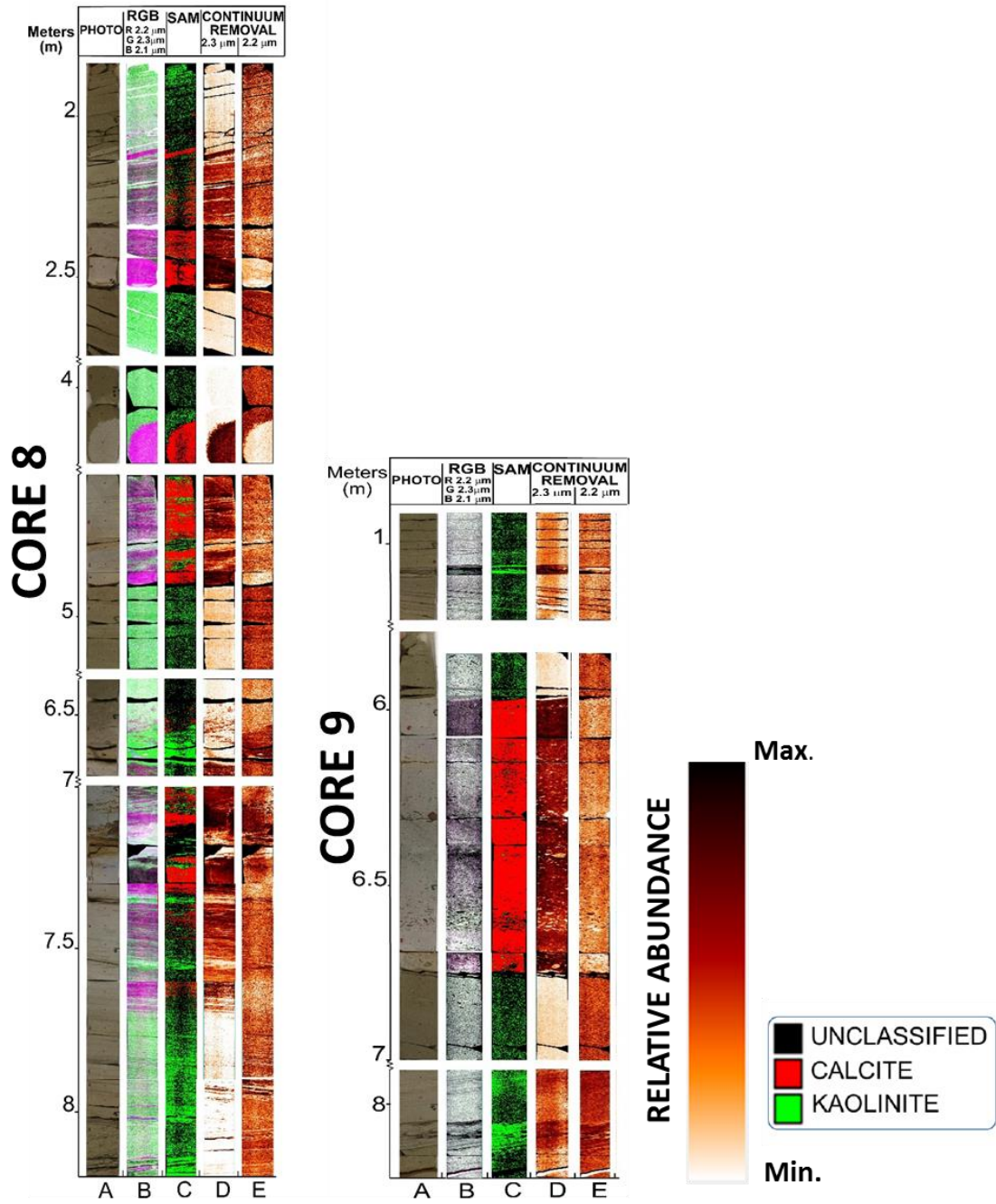


Figure 3-5 Core eight and core nine from Raptor Ridge. (Column a) Core photograph. (Column b) False-color composite image with spectral bands 2,195 nm, 2,334 nm, and 2,152 nm displayed as RGB. (Column c) Spectral Angle Mapper classified image using U.S. Geological Survey spectral library from calcite and kaolinite. (Column D) Normalized spectra depicting depth at band 2,334 nm (calcite). Darker red means deeper absorption features; hence greater abundance. (Column E) Normalized spectra depicting depth at band 2,195 nm (kaolinite). Darker red means deeper absorption features; hence greater abundance.

3.2.2 Imaging of the Outcrop

For a quick analysis of the SWIR outcrop data, MNF output bands were first examined (Figure 3-6b). Band ratios images were generated to highlight areas with spectral differences between bands (Figure 3-6c), making it easier for subsequent endmember selection. In Figure 3-6c, carbonate concretions are shown in cold colors (green/blue), whereas the host rock is shown in warm colors (yellow/red). With very similar spectra, channel and bar facies are not distinguished here.

The SWIR outcrop image was classified using SAM and MTMF classification algorithms. The results were compared to each other and to previous studies to determine which technique performs better in siliciclastic rocks for hyperspectral image processing.

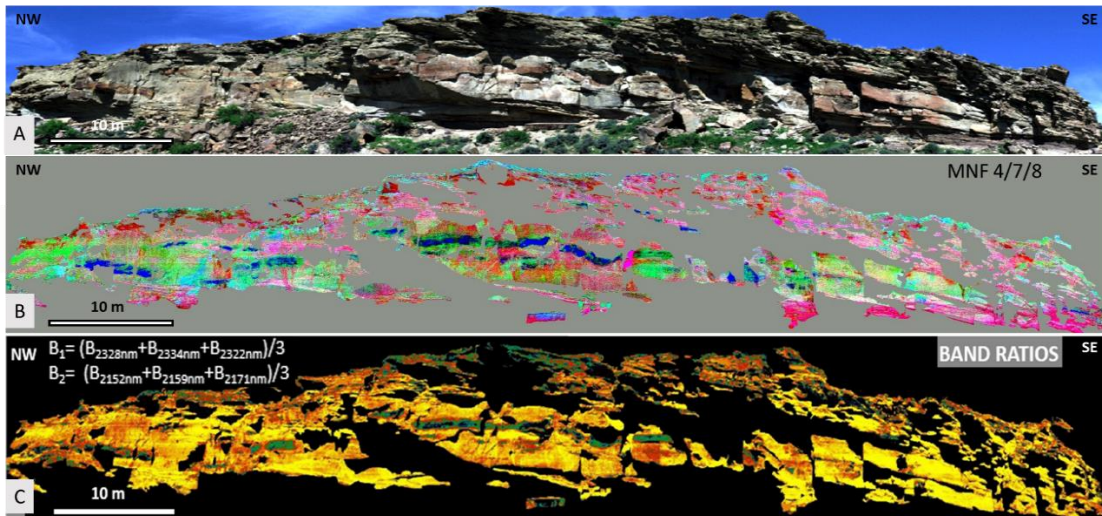


Figure 3-6 (a) Outcrop VNIR image in true color composite showing bands 174, 111, and 55 displayed as RGB. (b) Minimum Noise Fraction Transformation image for SWIR with bands 4,7,8 displayed as RGB. (c) Band ratios image for SWIR data displayed in (B_1/B_2) to enhance spectral differences [$B_1=(B_{2328nm}+B_{2334nm}+B_{2322nm})/3$, $B_2= (B_{2152nm}+B_{2159nm}+B_{2171nm})/3$]. Grey and black pixels correspond to mask areas in A and B, respectively.

SWIR reflectance data in MNF space are shown in Figure 3-7a. The first 11 MNF components were found to be spatially coherent, with eigenvalues less than 3.0. The spectra of the endmembers in MNF space used for MTMF classification are shown in Figure 3-7a, MTMF results are illustrated in Figure 3-8a. After data normalization, the abundance of each endmember was calculated from the MTMF classification results (Figure 3-10). Carbonate concretion represent 10 % of the outcrop while channel facies represent 54.6 %, bar facies represent 31 %, and distal facies represent 4 %.

The spectra of endmembers derived from, the outcrop SWIR image itself, core SWIR, and ASD are shown in Figure 3-7 b & b', Figure 3-7 c & c', and Figure 3-7 d & d', respectively. The graphs on the left show the reflectance of each endmember, whereas the graph on the right depict the normalized reflectance (continuum removed data) of each endmember. It should be noted that sometimes, differences between each endmember can only be determined in the normalized data. The SAM algorithm was applied to these three datasets (Figure 3-8b, c, and d) and the abundance of each endmember were compared as shown in Figure 3-10.

Different classification algorithms from the same endmembers, provided similar results (Figure 3-8a and b with MTMF and SAM). In Figure 3-8 b SAM classification results are shown. Similar to MTMF results, carbonate concretions represent 10 % of the outcrop. Comparatively, bar facies were ~30 %, channel facies were 59 %, and distal facies were 3 % of the total outcrop exposure.

SAM classification algorithm was applied using the spectral data and hyperspectral data collected in the laboratory (Figure 3-8c and d) as endmembers. The spectral and spatial variability between laboratory datasets and the hyperspectral data from the outcrop could be a

constraint in the classification process. For the SAM classified image, using hyperspectral data collected in the laboratory, carbonate concretions also represent 10 % of the outcrop. Bar facies are 47.5 %, channel facies are 41 %, and distal facies are 1 % (Figure 3-8c). These results were comparable with the ones obtained applying SAM algorithm with spectral data as endmembers (Figure 3-8d), where carbonate abundance are (15 %), bar facies are 46 %, channel facies are 37 % and distal facies are 2 % of the outcrop exposure.

The dissimilarity between spectra in carbonate concretions and host rock increases the accuracy of the classification. However, spectrally similar endmembers can be easily misclassified. This was the case of bar, channel facies, and distal facies, whose spectra were very similar (Figure 3-7).

From the classification results, carbonate concretions are distributed subparallel to the outcrop as elongated and heterogeneous patches. Overall, all classification methods show a lateral change in facies at the NW part of the outcrop from bar facies to a more channelized sandstone. Channel facies are predominantly located at the base of the Raptor Ridge outcrop with sharp contact at the base and top of each channel.

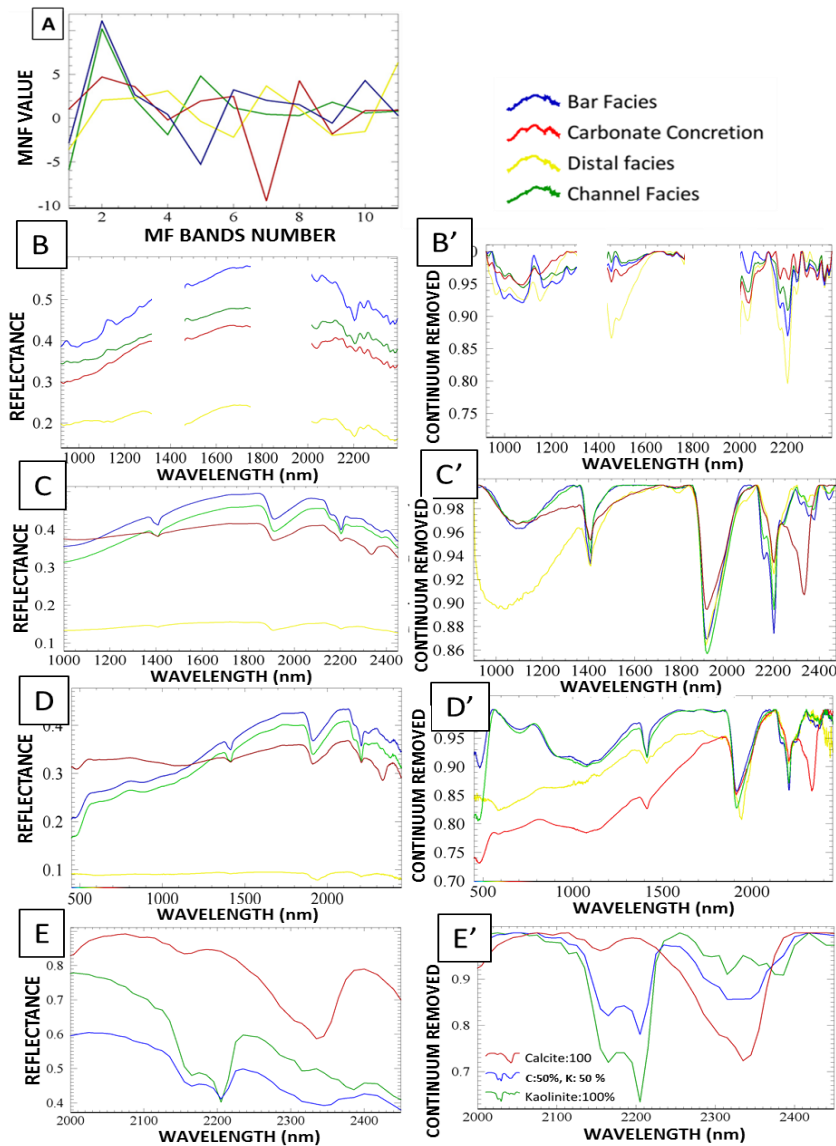


Figure 3-7 SWIR spectra of ROI's that were used for classification purposes. (a) Selected endmembers in the coherent MNF bands for MTMF classification. (b) Reflectance spectra of the selected endmembers in the hyperspectral image for SAM classification. (b') Continuum removed reflectance spectra of the selected endmembers in the hyperspectral image for SAM classification. Gaps in reflectance spectra correspond to water absorptions at 1,400 nm and 1,900 nm that were removed from the image. (c) Reflectance of facies derived from SWIR spectral data of cores. (c') Continuum removed reflectance of facies derived from SWIR spectral data of cores. (d) Reflectance of facies derived using spectroradiometer data. (d') Continuum removed reflectance of facies derived from spectroradiometer data. (e) Spectra of kaolinite and calcite and kaolinite:50 %-calcite: 50 % created from U.S. Geological Survey spectral library (Clark et al. 2007). (e') Continuum removed spectra of kaolinite and calcite and kaolinite:50 %-calcite: 50% created from U.S. Geological Survey (Clark et al. 2007).

In order to visualize the relative cement abundance, well-ordered kaolinite, calcite, and spectra of calcite (50 %)-kaolinite (50 %) mixture using from U.S. Geological Survey spectral library data were used (Figure 3-7 e & e'). The normalized SWIR spectra, using continuum removal, at specific bands (~2,200 nm and ~2,334 nm) were plotted to evaluate the relative abundance of kaolinite (Figure 3-9b) and calcite (Figure 3-9c) cements within the sandstone. In Figure 3-9a SAM results using U.S. Geological Survey spectral library are shown. Minimum abundance kaolinite was found within the carbonate concretions. Nyman et al. (2014) suggested that kaolinite and chlorite were precipitated after calcite. Therefore, calcite filled all pore spaces within the concretions preventing the precipitation of other mineral phases. Interestingly, kaolinite shows greater abundance in areas where distal facies and frontal splay facies were previously described (Figure 1-3). Prodelta facies are composed of sandy claystone and < 25 % of very fine grain sands (Gani & Bhattacharya 2007). On the other hand, frontal splay deposits may be found locally sandwiched between muddy prodelta facies (F1). These characteristics could allow these facies to have more clay content. The bottom left section of the outcrop is composed of frontal splay facies, as well as the top right section (Figure 3-4). Prodelta facies can be found in the middle-bottom part and right-bottom part. Distal facies, are usually darker in nature. Darker materials do not reflect light as well as lighter materials and absorption peaks were attenuated. Therefore, these facies might suffer from inaccurate classification.

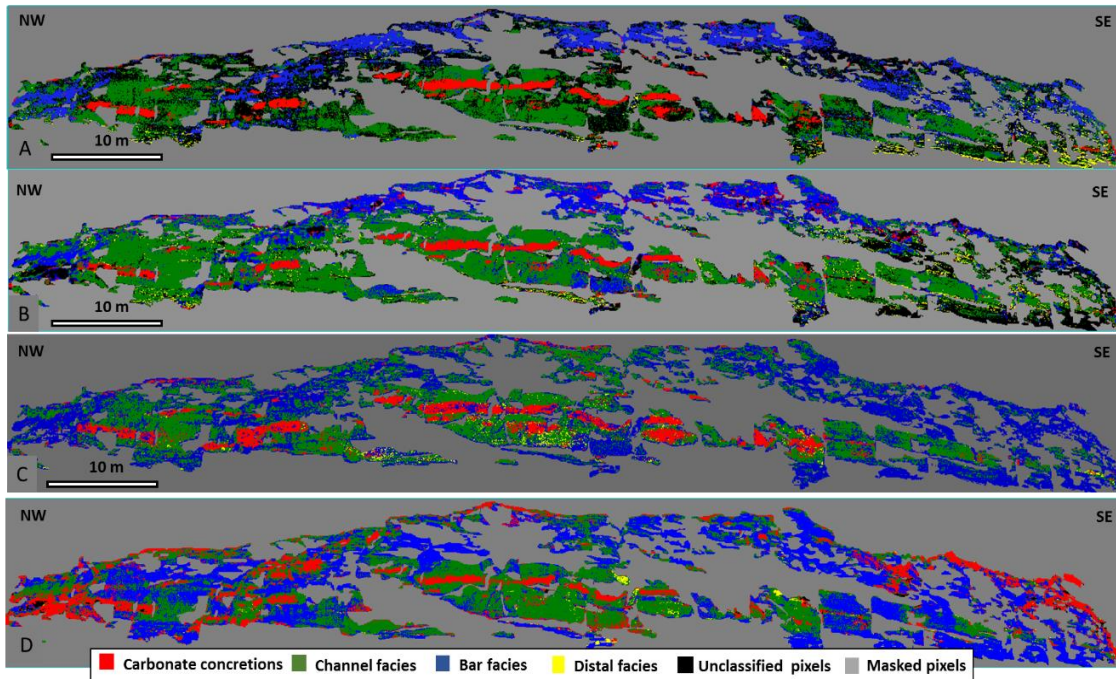


Figure 3-8 (a) Hyperspectral map extracted from the MTMF image using SWIR data set is depicted. Only pixels where MT score are >50 % or more, and infeasibility less than 30 were plotted. (b) Reclassified rule-based SAM image using extracted endmember from the image itself based on field data. (c) Reclassified rule-based SAM image using SWIR hyperspectral image spectra collected in the laboratory. (d) Reclassified rule-based SAM image using endmembers extracted from spectral data.

Previous extensive sedimentological studies (Gani & Bhattacharya 2007; Lee et al. 2007; Nyman et al. 2014) developed facies distribution maps based on detailed field observations (sedimentary structures, lithofacies, and ichnofacies description) (Figure 1-3).

The abundance of carbonate concretions estimated from hyperspectral data closely matched previous detailed studies (Lee et al., 2007 & Nyman et al., 2014) and suggested 12 % carbonate concretions for this outcrop (Table 1-3). The matching was based on visual comparison between MTMF classification results (Figure 3-8a) and previously created cement maps (Figure 1-3b).

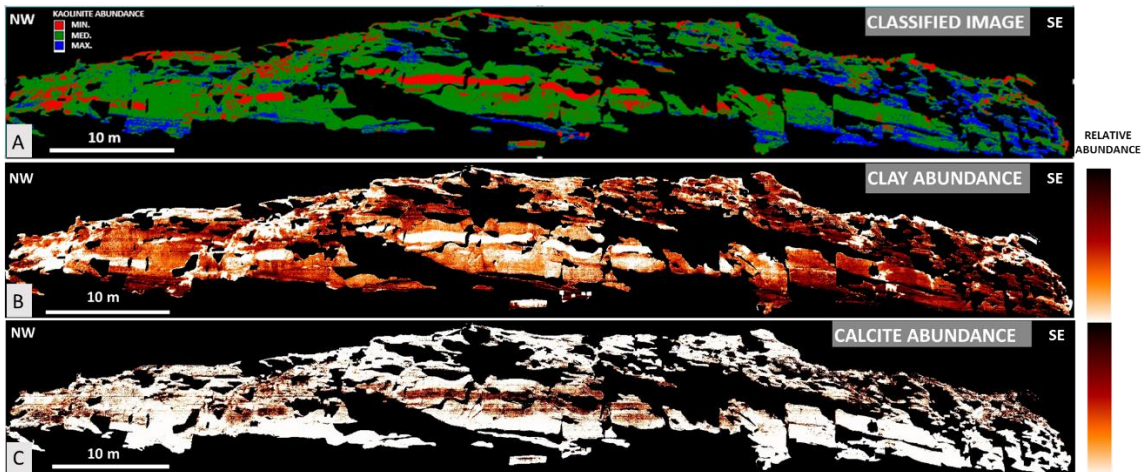


Figure 3-9 (a) SAM classified image using normalized SWIR image for kaolinite. Red corresponds to kaolinite free areas. Maximum content of kaolinite is shown in blue. (b) Normalized image showing 2,205 nm wavelength depth that corresponds to kaolinite absorption feature. (c) Normalized image depicting 2,334 nm wavelength depth that correspond to the absorption feature of calcite. Darker red areas correspond to greater depth features; hence more abundance. A threshold of 0.95 was used for noise removal.

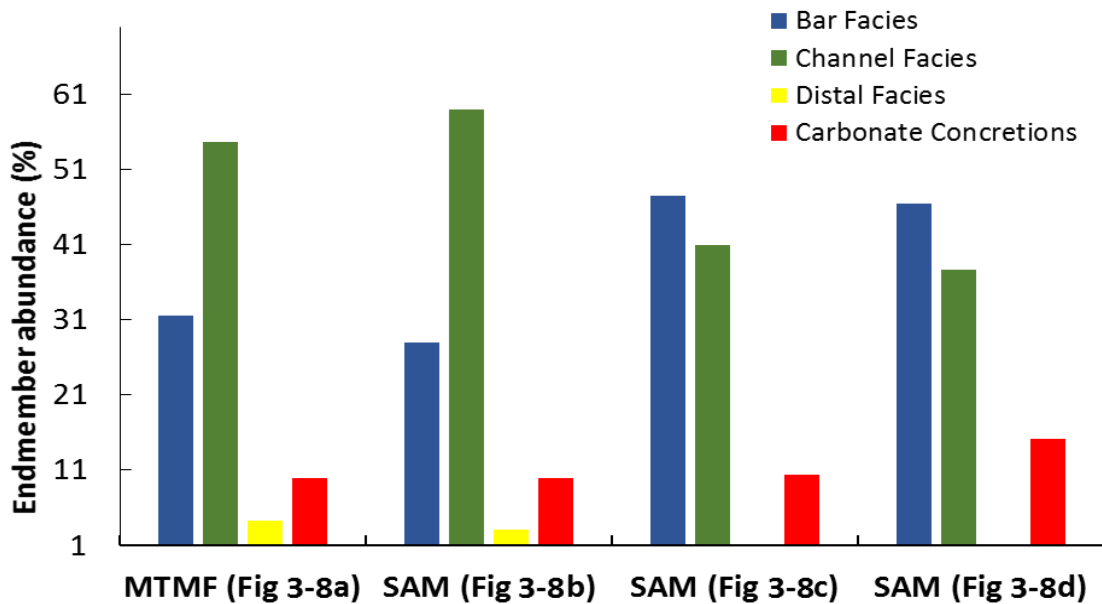


Figure 3-10 Comparison of normalized abundance of endmembers based on different classification methods in SWIR image of Raptor Ridge. All calculations were normalized excluding masked pixels for results.

3.3 DISCUSSION

Analysis of the spectral data reveal accurate information about mineralogical variations between facies association in Parasequence # 6 of the Frontier Formation. In addition, specific absorption features provide information about the rock physical characteristic (e.g., depth), such as grain size (Gaffey 1986; Zaini et al. 2012). In general, when calcite is present, the overall reflectance at the VNIR part of the spectra increases (e.g., Figure 3-2d). The overall spectral reflectance of channel facies was slightly lower than bar facies, probably related to a slightly greater grain size (Figure 3-1 and Figure 3-2). The higher absorption minimum depth of kaolinite in bar facies vs. channel facies cannot be related to greater abundances, since there was a difference in grain size between the two facies. Besides, the depth of the peak of the kaolinite in carbonate concretions vs. sandstone host rock could be related to abundance. The presence of an absorption minimum at ~2,335 nm in the concretions matches with the existence of calcite cement (Figure 3-3). The depth of these peaks slightly increased at the edges and could be associated with a greater abundance of calcite.

Bar facies are tidally influenced deposits, which show interbedded-thin mudstones between sandstone beds. Calcite cement can only precipitate in sandstone, giving a heterogeneous cement distribution, which was observed in the cores. On the other hand, channel facies, that have a fluvial influence, are massive. Therefore, calcite cement distribution appears homogeneously distributed along the concretions.

Considering previous studies (Lee et al., 2007 & Nyman et al., 2014), the MTMF classification method has been proven to be the most effective and reliable methodology to classify facies in a deltaic outcrop (Figure 3-8a). The variability of the abundance of channel

facies and bar facies depend on the classification methodology (Figure 3-10). The higher spectral variability between endmembers, the better the accuracy and reliability of the classification. Carbonate concretions are well characterized with SAM and MTMF methods (Figure 3-8). For all of the SWIR classification results, carbonate concretions represent ~10 % of the outcrop exposure, which matches previous sedimentological studies and suggested a 12 % abundance (Table 1-3 and Figure 3-10). These previous studies, were taken as a “ground truth” to estimate the accuracy of the results. Characterization of cement was tedious and time consuming due to visual similarity with the host rock (Janok P. Bhattacharya personal communication). Cement mapping using hyperspectral is a reliable and faster technique when combined with outcrop observations improves characterization results.

The comparison with previous studies was done based on visual information and, with the information available, it is not possible to systematically compare exact percentage of abundance based on previous work. This is because the angle from which the images were taken in both studies were different, and therefore results were slightly different. Gani & Bhattacharya (2007); Lee et al. (2007) and Nyman et al.(2014) created facies distribution maps based on field data. After, the results were plotted in an image collected from the top of the opposite ridge wall (200 m away). Hyperspectral outcrop data in this work was collected from the bottom of the opposite ridge wall, where the distance between the target outcrop and cameras was shorter (50 m) to improve resolution of the hyperspectral data.

Areas at the edge of the image can be distorted because of the cylindrical coordinate system of the hyperspectral images, so accuracy of the facies abundance should be taken with care. In this case, images were collected from a certain distance and at the center of the targeted area to reduce distortions. To obtain a highly accurate percentage for each endmember in the

image, the classified image should be draped over a point cloud Terrestrial Lased Scanning (TLS) dataset.

Outcrop areas, that do not receive direct sun light, cannot be correctly classified due to the lack of spectral information in these pixels. It was assumed that shadows are randomly distributed and classification results were normalized to obtain the final statistics and facies abundance.

Based on MTMF results, the area of each endmember abundance was estimated. Parasequence # 6 at Raptor Ridge is composed of 87 m² of bar facies, 150 m² of channel facies, 12 m² of distal facies, and 27 m² of carbonate concretions.

CHAPTER 4

4. RESULTS: THE UTRILLAS FORMATION

4.1 STRATIGRAPHY AND SEDIMENTOLOGY

The outcrop of the Utrillas Formation is composed of two poorly-cemented sandstone cycles that present a fining-upward sequence (~10 m thick) with an erosive base (Figure 4-1 & Figure 4-2a & b). The schematic stratigraphic column is shown in Figure 4-1. Above the erosive surface of the second cycle there is a thin highly oxidized conglomeratic bed (yellow arrow in Figure 4-2a). Meter scale cross stratification was found at the mid-part of the section. The bedding seems to be truncated at the top and it was not possible to measure its length. The second cycle (W-E outcrop Figure 4-2a) has more than one fining-upward sequence, suggesting a complex paleochannel facies. The upper part is composed of very fine to clay-size deposits. These sediments tend to be massive but some show thin bedded lamination. Sediments are grey to yellowish in color with some staining caused by Fe-oxides (Figure 4-2c). A blackish stained area was observed which does not follow the stratigraphy, and is located between the top of the first sandstone package and second claystone package (in Figure 4-1). Wood chips and pyrite cubes were found. This area is related to the presence of bitumen patches in the Utrillas Formation (ITGE 1994; AGGEP 2015). Native sulfur leakage and cubes of pyrite were found (Figure 4-2d).

The facies are interpreted as paleochannels and flood-plain facies deposited by a meandering stream. The large scale cross bedding suggests lateral accretion of point-bar deposits (Miall 1996). Miall (1996) suggested that the thickness of a meandering river sandbody deposits are approximately equal to the bankfull depth. According to this, the sediments at Basconillos del Tozo were deposited in a meandering river with a bankfull depth of: ~6 m. On the other hand, the width of the point bar (measured by the length of a single accretion surface)

is approximately two thirds of the former channel bankfull width (Miall 1996). Although, cross stratification seemed to be truncated by other paleochannel erosive surfaces, the width of the point bar was at least 15 m measured from W-E outcrop. Therefore, width to depth ratio was 2.5 corresponding to a high sinuosity meandering river.

These observations correlated with the upper member (U2) of the Utrillas Formation previously described by Arostegui et al. (2000) in the Pancorbo area, which is located north of present study area.

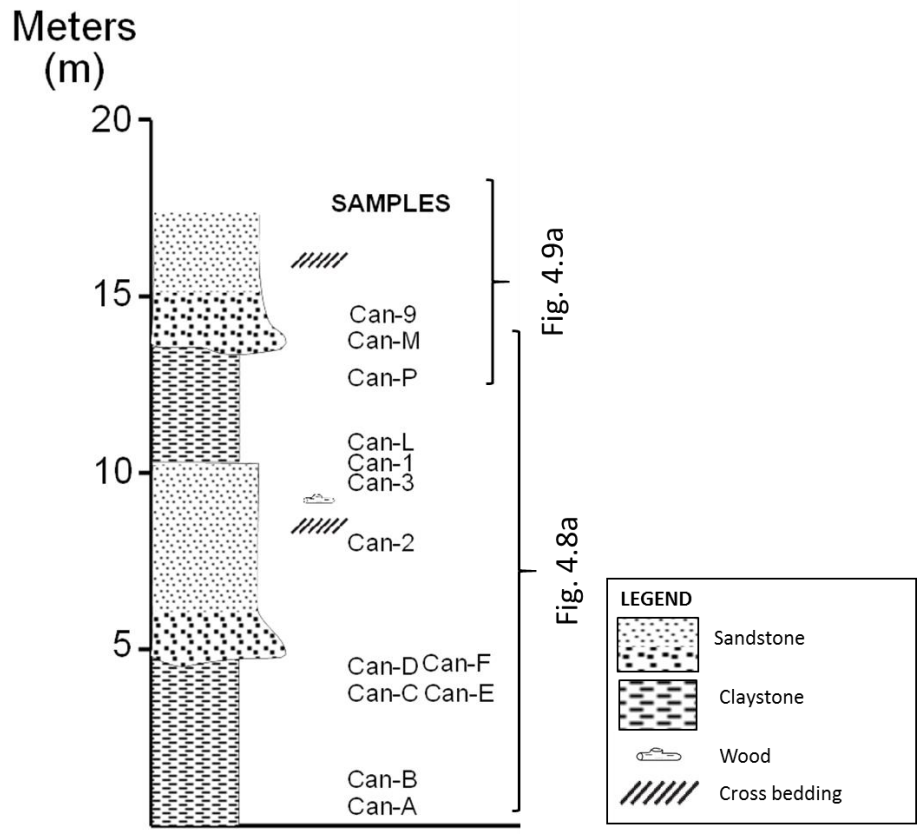


Figure 4-1 Schematic stratigraphic column for the outcrop of the Utrillas Formation. The locations for hand samples are shown. Figure 4-8a is for the S-W outcrop wall, whereas, W-E outcrop wall is shown in Figure 4-9a.

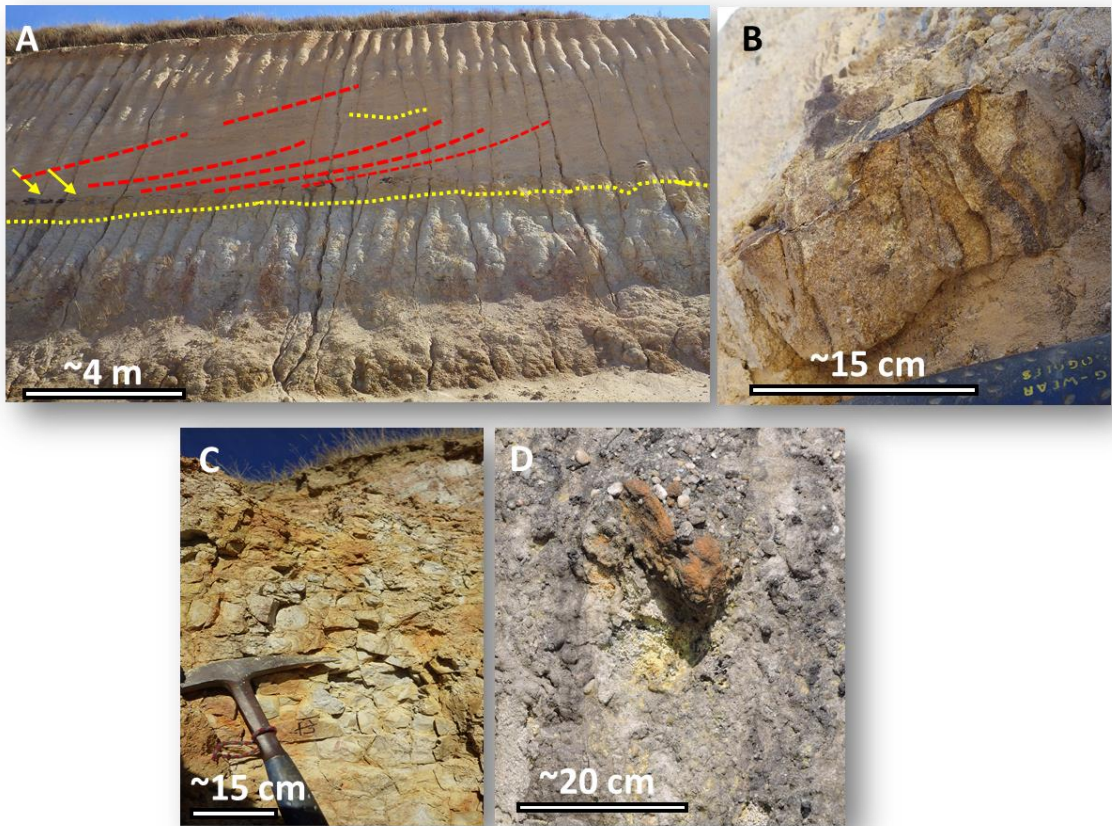


Figure 4-2 Photographs of the Utrillas Formation outcrop at Basconillos del Tozo. (a) The top sandstone package (in Figure 4-1) with planar cross stratification. Red dashed follow the stratification. Erosional contact between claystone and sandstone layers is marked by yellow line. (b) Conglomeratic sandstone at the base of the second sandstone package. claystone layers with supergenic alteration minerals that provide this reddish, yellowish color. (c) Fracture claystone with yellowish color. (d) Presence of native sulfur as an alteration product.

4.2 SPECTRAL DATA

The reflectance spectra of thirteen hand samples were collected using the ASD spectroradiometer. The most prominent absorption peaks in each sample are depicted in Table 4-1. Figure 4-3a show a photograph of the hand samples collected. The spectral data were compared with the reflectance data collected from images of SWIR hyperspectral camera (Figure 4-3b). Both datasets were nearly identical. The absorption peaks at $\sim 1,415$ nm and

~1,910 nm were related to water absorptions and, therefore, not taken into account in this study (Figure 4-3 and Table 4-1).

In samples Can-1, Can-2, Can-E, Can-M, and Can 9 peak absorption minimum of the VNIR part of the spectra were around ~ 500 nm & ~960 nm, and a smaller one at ~660 nm that can be related to the spectral signature of goethite (Table 4-1) (Haest et al. 2012). On the other hand, samples Can-L and Can-C, present absorption minimum peaks at 510-520 nm and 880-900 nm. These peaks resemble hematite spectra (Figure 2-1). Any mixture of these two Fe-oxides will present absorption minimum peaks in between goethite and hematite spectra.

Table 4-1 Major absorption minimum in spectral data of the hand specimen. Grey color corresponds to absorption minimum related to water. Red color corresponds to absorption minimum related to iron oxide minerals. Blue color corresponds to absorption minimum related to clay minerals.

Can-1	Can-2	Can-3	Can-A	Can-B	Can-C	Can-D	Can-F	Can-E	Can-9	Can-L	Can-M	Can-P
489	512	595	1414	528	533	583	606	496	501	522	512	604
979	951	1413	1912	1414	909	1413	1413	989	967	890	973	1413
1413	1413	1732	2207	1911	1413	2206	1911	1413	1415	1414	1433	1911
1922	1919	1917		2207	1727	2458	2206	1912	1728	1916	1931	2208
2207	1728	2164			1912			2207	1935	2208	2309	
	2165	2206			2206				2162			
2484	2207	2455							2207			
									2308			

The most prominent peak in the SWIR part of the spectra was at ~2,205 nm and is related to clay minerals, as shown in samples: Can-1, Can-2, Can-3, Can-A, Can-B, Can-C, Can-D, Can-F, Can-E, and Can-P. In Can-2 and Can-9 there was a smaller but prominent secondary peak at ~2,165 nm. This doublet is related to well-ordered kaolinite (Clark et al. 1990). In the rest of the samples, there was a slight concave shape at ~2,165 nm but not enough to create a doublet. This is characteristic of poorly-ordered kaolinite (Clark et al. 1990). Moreover, when kaolinite and micaceous phases coexist, the prominence of that secondary peak might be reduced.

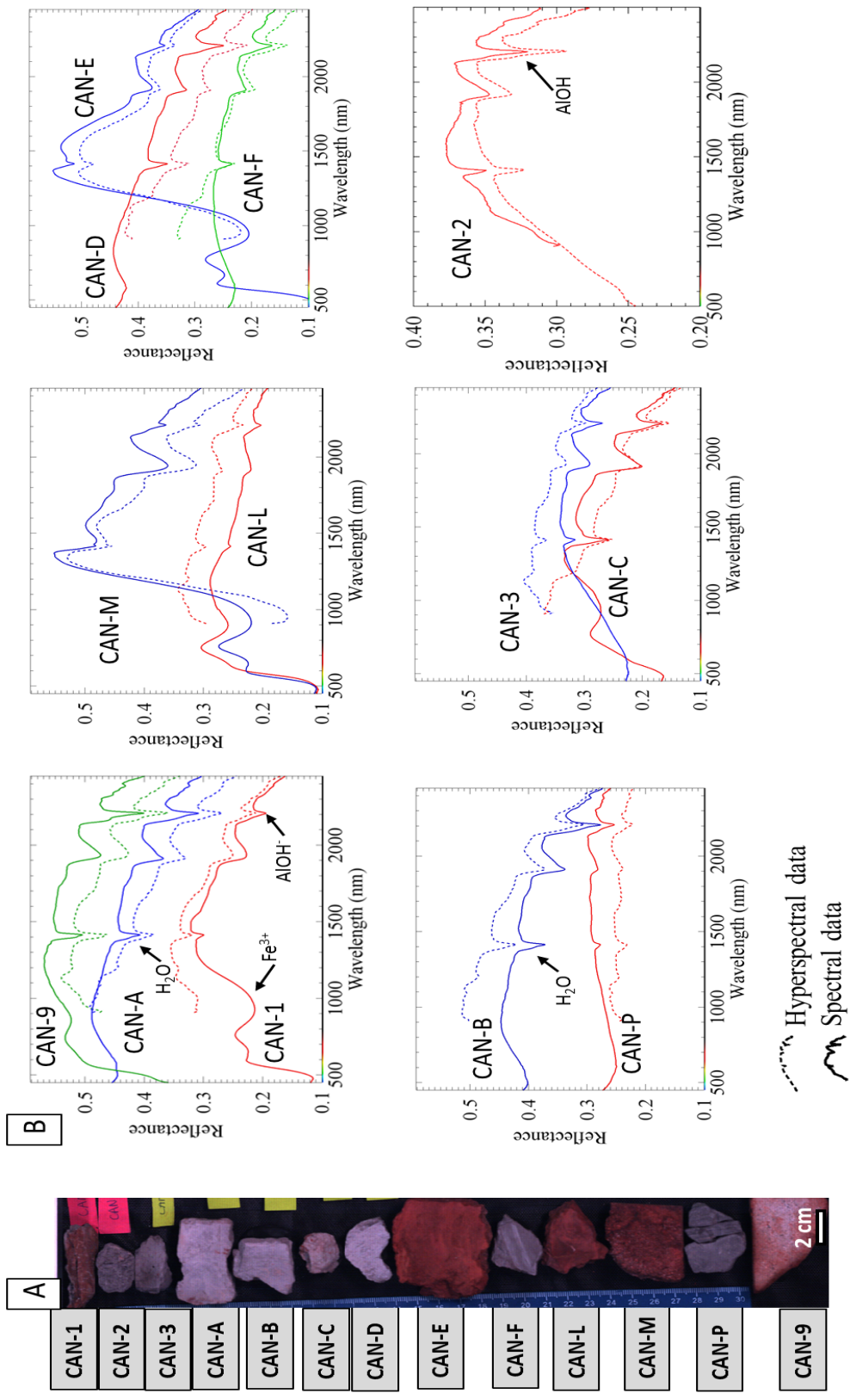


Figure 4-3 (a) Photograph of thin sections of samples from Utrillas Formation. (b) Plots showing the reflectance spectra in nanometers of the thin sections data collected with spectroradiometer (continuous lines) and laboratory setting SWIR hyperspectral image (dashed lines). Colors were chosen randomly.

4.3 HYPERSPECTRAL DATA

Different approaches and classification methods were employed to interpret thirteen hand samples and two SWIR outcrop images of the Utrillas Formation in Basconcillos del Tozo.

4.3.1 Imaging of Rock Samples

Several samples were collected at different parts of the outcrop. The locations are shown in Figure 4-1. Three samples Can-2, Can-9, and Can-M were collected at the coarser-grain facies, nine samples Can-A, Can-B, Can-C, Can-D, Can-F, Can-E, Can-L, Can-1 correspond to finer-grain deposits, and one from the dark altered area (Can-3). A photograph of the thirteen samples (chips), that were scanned on the stage, is shown in Figure 4-4a. For an initial interpretation of the SWIR data, MNF bands are displayed as RGB. In this case the first 20 bands were found to be spatially coherent and with eigenvalues less than 3.0 (Figure 4-4b). The MNF results were grouped in to three, Can-1, Can-2, & Can-3; Can-A, Can-B, Can-C, Can-D, & Can-F; and Can-E, Can-9, & Can-M. Each group of samples have similar spectra among them and different between the groups. The analysis of results for band-ratio image show a spectral similarity between samples grouped in to, Can-1, Can-2, & Can-3; Can A, Can-B, Can-C, Can-D, & Can-F and Can-E, Can-L, & Can M (Figure 4-4c).

SWIR images of the hand samples were classified using U.S. Geological Survey spectral library for clay minerals (Figure 4-5). Results show that clay minerals in Can-1 are most probably composed of a great abundance of the micaceous phase, while Can-A, Can-B, Can-C, Can-D, and Can-F tend to have an abundance of poorly-ordered kaolinite. Well-ordered kaolinite is present in Can-2, Can-3, and Can-9 (Figure 4-5).

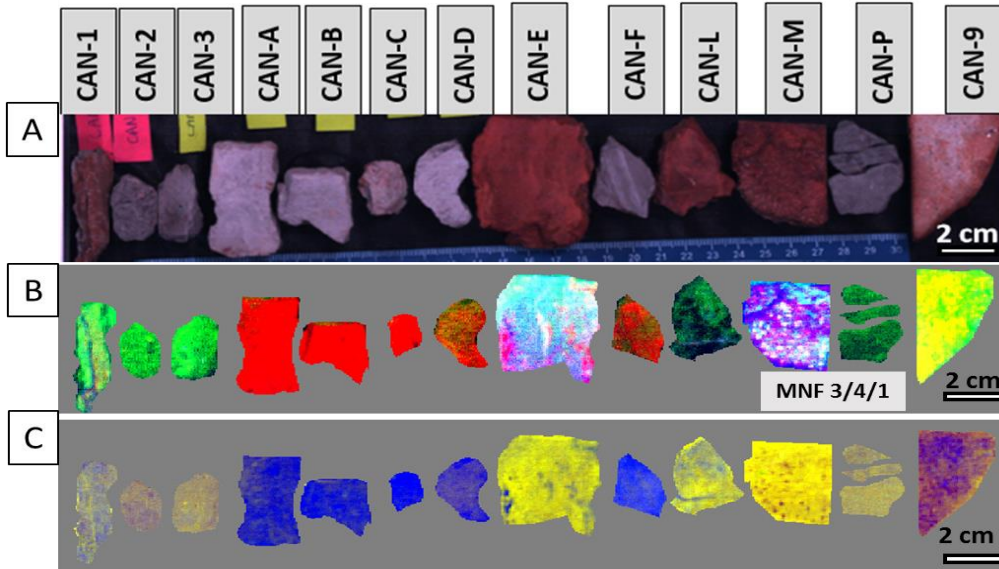


Figure 4-4 (a) True color composite image using the VNIR data of hand samples collected from the Utrillas Formation displayed as R: 475 nm, G: 510 nm, B: 650 nm. (b) MNF results for SWIR images with bands 7, 5, 4 displayed as RGB. (c) Band ratios image created from normalized data displayed as RGB. R: $(B1,958 \text{ nm}/B1,649 \text{ nm})$, G: $(B2,171 \text{ nm}/B2,127 \text{ nm})$, B: $(B2,151 \text{ nm}/B2,127 \text{ nm})$.

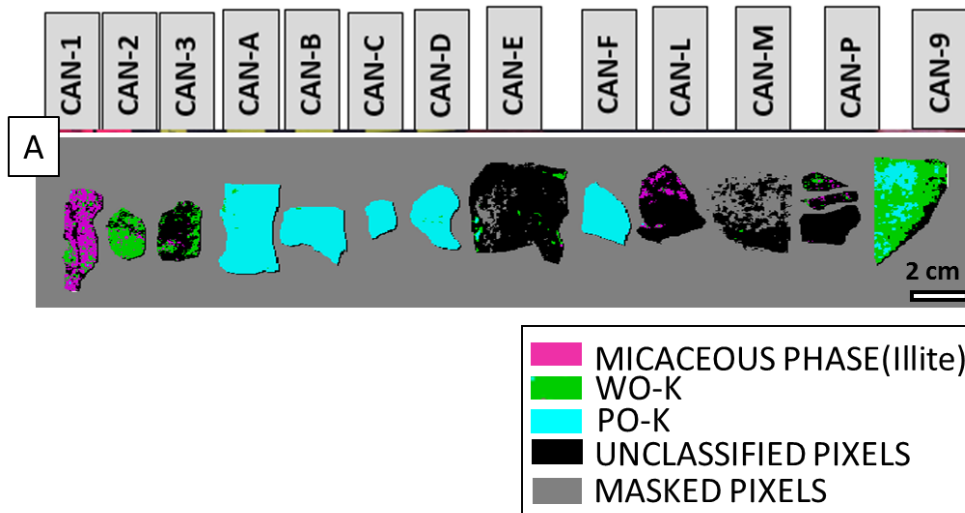


Figure 4-5 SAM classification image based on SWIR data from U.S. Geological Survey spectral library of: micaceous phase: Illite, well-ordered kaolinite [WO-K], and poorly-ordered kaolinite [PO-K]. The angular similarity threshold was always lower than 0.1 radians and different for each endmember.

Kaolinite and micaceous phases can coexist in the same rock. So, it is very unlikely that just one of the three clay minerals is present in one pixel, as depicted in Figure 4-5. Therefore, every pixel in the image is probably composed of a mixture/ percentage of the three endmembers, whose spectra differ from spectra of pure minerals. The resulting spectra in the pixel in question will be closer to the spectra of the endmember whose relative endmember abundance is higher. The SAM algorithm measures the similarity angle between the given spectra (in this case pure mineral endmembers) and the image. Here, the angular similarity threshold was always lower than 0.075 radians and has been varied for every endmember. Therefore, areas classified with a certain endmember have a very high abundance of that endmember.

Well- and poorly-ordered kaolinite spectra have certain divergences that allow resolving their presence and relative abundance (Figure 4-6). Specifically, when pure well-ordered kaolinite is present, the depth at band 2,159 nm tends to be deeper than the band at 2,165 nm in the normalized spectra. Besides, in pure poorly-ordered kaolinite spectra the depth at band 2,159 nm is equal or slightly smaller than the depth the band at 2,165 nm. The micaceous phase shows a significantly deeper peak at ~2,165 nm than 2,159 nm. Although the depth absorption minimum of the micaceous phase is equal to kaolinite, at ~2,203 nm, micaceous phase absorption features are wider, and therefore the absorption peak width finished one or two bands after the kaolinite absorption peak (Figure 4-6).

The crystallinity of the Utrillas Formation kaolinites in the hand samples was resolved using the “Kaolinite-Crystallinity Index” (KCI) and the “Micaceous phase abundance Index” (MPAI) (Figure 4-7a &b). Both mathematical expressions were applied in the normalized SWIR area of the spectra from 2,120 nm to 2,430 nm. When the KCI was applied, lower values imply that the secondary absorption minimum at 2,165 nm of the kaolinite was present. On the other hand,

higher values imply that the secondary absorption minimum at 2,165 nm of the kaolinite was weak or was not present (Figure 4-6). After initial data analysis, a threshold of 0.045 was set. KCI below 0.045 were considered to contain well-ordered kaolinite, values above 0.045 were considered to contain poorly-ordered kaolinite.

In a given pixel, with a mixture of high-micaceous phase abundance and low well-ordered kaolinite abundance, the secondary absorption feature at ~2,165 nm can resemble the spectra of poorly-ordered kaolinite, but the width of the absorption minimum, at ~2,206 nm, should be different. In order to resolve that, the MPAI was applied into the KCI results (Figure 4-7b). The very last band of the clay mineral absorption minimum was used to quantify the relative abundance of micaceous phase. The band at 2,271 nm was selected as an indication for micaceous phase abundance, which corresponds to the last band of the absorption minimum of pure kaolinite. Therefore, if the depth of band at ~2,271 nm equals 1, micaceous phase abundance is low. When this number is lower or greater than 1 indicates that the width of the absorption minimum at 2,203 nm is larger, and the abundance of micaceous phase is greater.

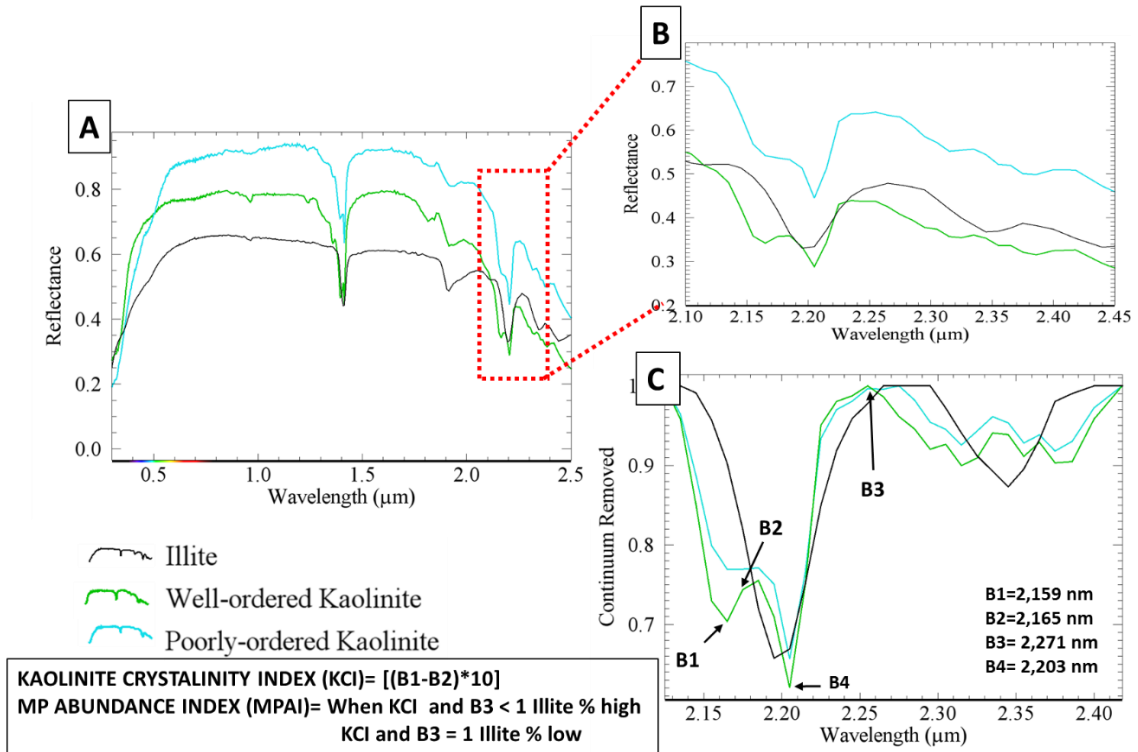


Figure 4-6 (a) Graph depicting wavelength (μm) vs. reflectance of the U.S. Geological Survey spectra of: illite in black, well-ordered kaolinite in blue, and poorly-ordered kaolinite in green. (b) Zoom to the graph A depicting the differences between illite, well-ordered kaolinite, and poorly-ordered kaolinite at $\sim 2,206$ nm absorption minimum. (c) Continuum removed reflectance spectra from 2,140 nm to 2,450 nm showing the bands used for kaolinite-crystallinity index and Micaceous Phase (MP) abundance index.

KCI and MPAI results are depicted in Figure 4-7a & b, respectively. For KCI, low values (less than 0) are represented by warm colors and indicate the presence of well-ordered kaolinite [Can-2, Can-3, Can-E, Can-L, Can-9, and Can-M]. While, high values (greater than 0) are depicted in cold colors and represent pixels with poorly-ordered kaolinite or very high-micaceous phase abundance. The samples with a greater abundance of poorly-ordered kaolinite or micaceous phase are: Can-A, Can-B, Can-C, Can-D, and Can-F. Only pixels with 2,203 nm absorption with depths greater than 0.95, with the continuum removed were used for classification.

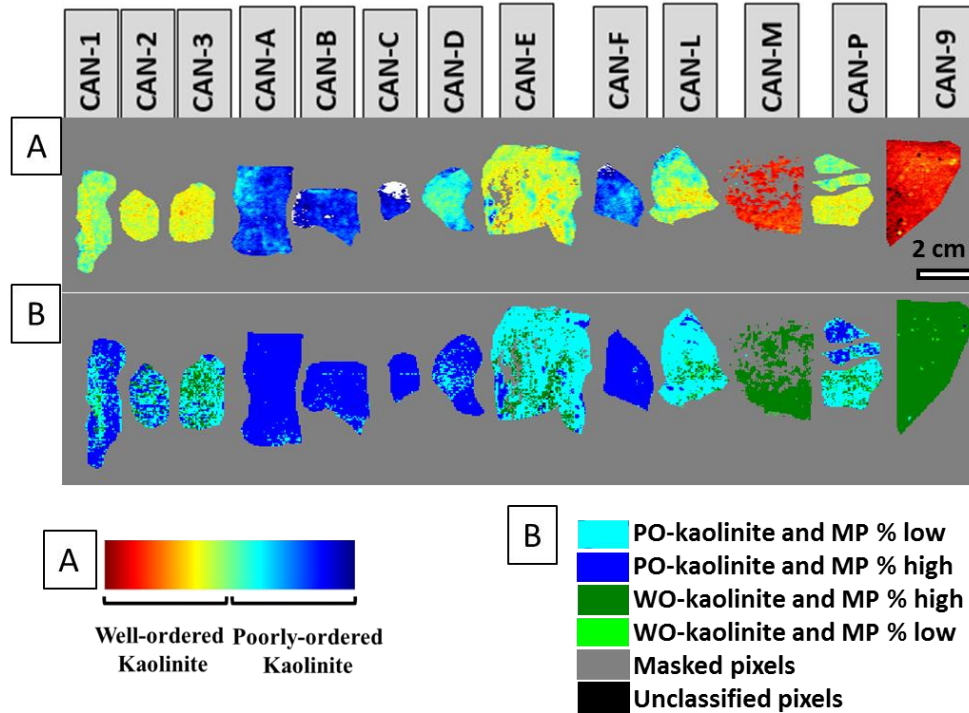


Figure 4-7 (a) Hyperspectral images of hand samples from the Utrillas Formation generated by applying 'Kaolinite-Crystallinity Index'. Warm colors are indicative of low values, thus presence of well-ordered kaolinite. Cold colors indicate high values, thus presence of poorly-ordered-kaolinite. (b) Classified image generated by applying 'Micaceous phase-crystallinity Index. Only pixels with 2,203 nm absorption feature depth greater than 0.95, of the continuum-removed image where used for classification. Abbreviations: PO-kaolinite and WH% low= poorly-ordered kaolinite and low-micaceous phase abundance, PO-kaolinite and WH% high= Poorly-ordered kaolinite and high-micaceous phase abundance, WO-kaolinite and WH% low= Well-ordered kaolinite and low-micaceous phase abundance, WO-kaolinite and WH% high= Well-ordered kaolinite and high-micaceous phase abundance.

Using both indexes, Can-2, Can-3, Can-E, Can-L, Can-9, and Can-M are composed of well-ordered kaolinite with certain abundances of micaceous phases (Figure 4-7b). Samples Can 1 and Can-P show a composition of poorly-ordered kaolinite with a low amount of micaceous phase, whereas Can-A, Can-B, Can-C, Can-D, and Can-F have higher abundance of micaceous phases (Figure 4-7b). Interestingly, Can-P depicts areas with poorly-ordered kaolinite with both high (dark blue) and low (light blue) abundance of the micaceous phase, showing a bedding

pattern (Figure 4-7). Grey and black pixels match with masked and unclassified pixels, respectively.

4.3.2 Imaging of the Outcrop

In this section, hyperspectral data of the two outcrops in the Utrillas Formations at Basconillos del Tozo were analyzed. Hyperspectral data of the outcrop were classified using different approaches. A true color image (Figure 4-8a and Figure 4-9a) based on the VNIR shows the S-N outcrop wall and W-E outcrop wall, respectively. It is important to notice that top layers of the right side of the S-W outcrop wall are the same as left side bottom layers of W-E outcrop wall.

For an initial interpretation of the SWIR data, MNF components were examined (Figure 4-8b & Figure 4-9b). The first 20 and 15 MNF components were found to be spatially coherent for the S-N outcrop and W-E outcrop, respectively. Band ratios were applied to highlight the areas where there were spectral differences between bands (Figure 4-8c and Figure 4-9c). MNF and band ratio results allowed the distinction among spectrally different beds. In Figure 4-8c and Figure 4-9c, cold colors (violet-blue-green) correspond to areas with finer-grain size samples were collected, whereas warm colors (red-yellow) correspond to areas where coarser-grain size samples. Reflectance spectra suggest that well-ordered kaolinite is present in the areas with coarse grain size and poorly-ordered kaolinite is present in fine-grain size sediments (Figure 4-8, graph 1-2-3 & Figure 4-9, graph 1&2). At the left side of the S-N outcrop and along the bottom part of the W-E outcrop some patches of spectrally different materials were detected (Figure 4-8b & c & Figure 4-9b & c). These irregular spots were much darker than the host rock and in places stained by oxides. Light was absorbed by the material in these irregular spots and

reflectance values were usually very low. This can create problems for classifying the image. Moreover, detailed spectral analysis suggests the presence of a spectral minimum at ~2,300 nm, characteristic for bitumen and hydrocarbons (Figure 4-8 Graph 3).

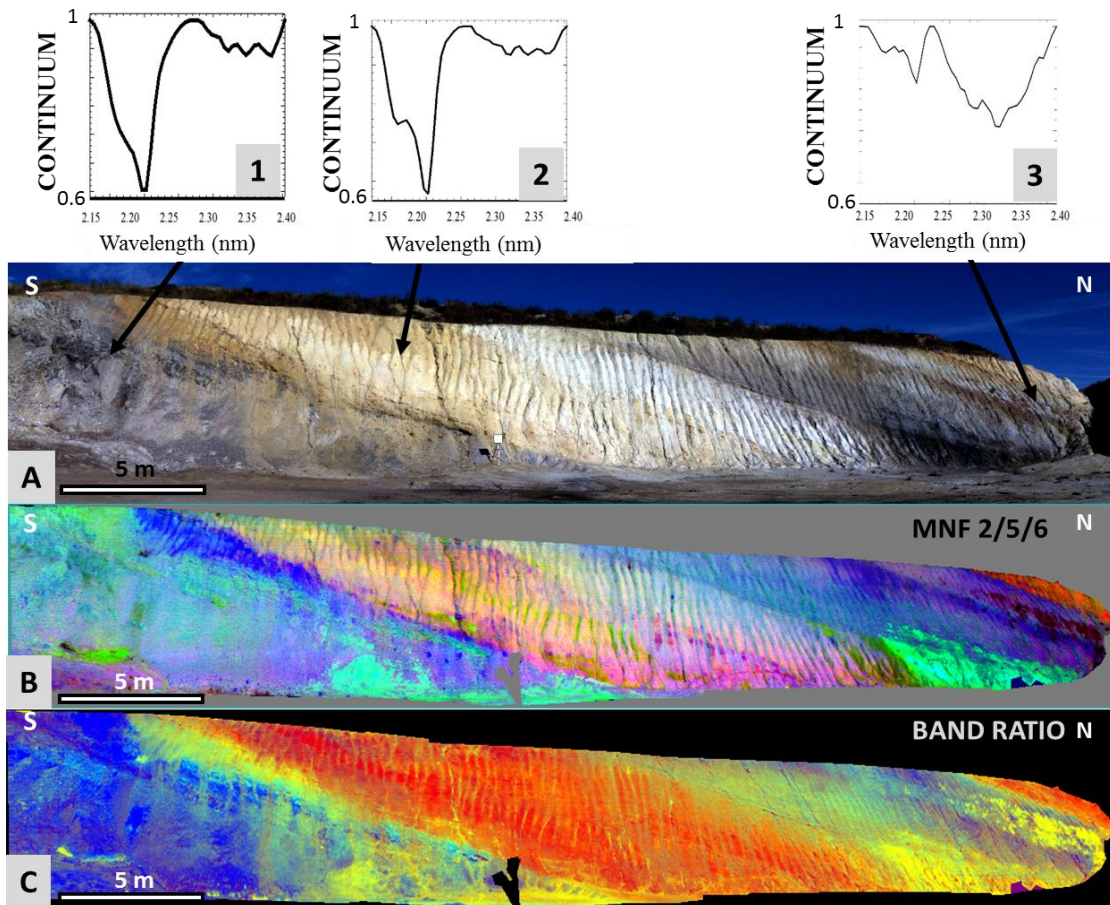


Figure 4-8 S-N outcrop of the Utrillas formation at Basconillos del Tozo. See Figure 1-5 for location. (a) True color composite VNIR image displaying bands R: 640 nm, G: 549 nm, and B: 469 nm. (b) Minimum Noise Fraction image for SWIR data with bands 2, 5, and 6 displayed as RGB. (c) Band-ratios image displayed as R: (Band 2,171 nm/Band 2,203 nm), G: (Band 2,203 nm/Band 2,171 nm), B: (Band 2,159 nm/ Band 2,171 nm). (Graph a) Example of continuum removed reflectance spectra of poorly-ordered kaolinite found in the flood-plain facies. (Graph b) Example of continuum-removed reflectance spectra of well-ordered kaolinite found in the paleochannel facies. (Graph c) Example of continuum-removed reflectance spectra of well-ordered kaolinite and calcite cement.

Thin-sections studies and spectroradiometer data allowed the identification of the two main facies, which contain spectrally distinctive minerals that might be present in the outcrop walls.

SWIR images of the outcrop were classified using spectral data collected from the hand samples to measure facies variations along the outcrop (Figure 4-8a & Figure 4-9a). Paleochannel facies are depicted in light green. Flood-plain deposits are depicted in dark blue. Alteration areas are depicted in yellow. Interestingly, zones of alteration in the S-W wall were related to either the top or bottom of the floodplain deposits. At the W-E wall alteration zones occur in patches.

For classification purposes (following the same procedure that was used for hand samples) U.S. Geological Survey spectral libraries were used (Clark et al. 2007). Well-ordered kaolinite, poorly-ordered kaolinite, and micaceous phase spectra (illite spectra) were used to classify the images of outcrop using the SAM algorithm (Figure 4-10b & Figure 4-11b). SAM classification results show two thick beds comprised of micaceous phase and poorly-ordered kaolinite which are shown in pink and blue color, respectively. These areas correspond to the previously classified flood-plain deposits in Figure 4-10b and Figure 4-11b. Well-ordered kaolinite is shown in green and correlates with previously described paleochannel deposits (Figure 4-10b & Figure 4-11b). Black and grey pixels correspond to unclassified and masked pixels, respectively.

The KCI was applied to the S-N outcrop wall (Figure 4-12a) and W-E outcrop wall (Figure 4-13a) of the quarry. Warm colors represent low values (less than 0.045 threshold) and the presence of well-ordered kaolinite. While, cold colors represent high values (more than 0.045 threshold) and the presence of poorly-ordered kaolinite or very high abundance of micaceous

phase (Figure 4-12a and Figure 4-13 a). From the continuum-removed image, pixels with 2,203 nm absorption feature with depths greater than 0.95 were used for classification.

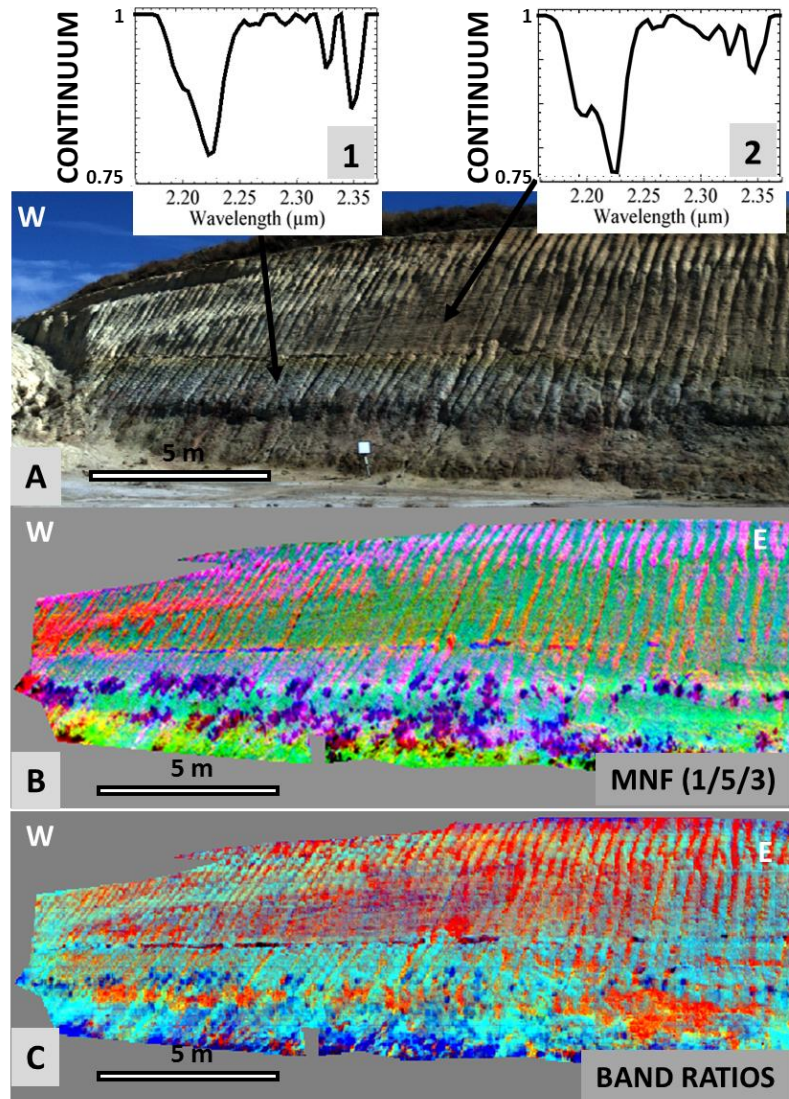


Figure 4-9 W-E outcrop of the Utrillas formation (a) True color composite VNIR image displaying bands R:640 nm, G:549 nm, and B:469 nm. (b) Minimum Noise Fraction image based on SWIR image with bands 1, 5, and 3 displayed as RGB. (c) Band-ratios image displayed as RGB the following: R: (Band 2,171 nm/Band 2,203 nm), G: (Band 2,203 nm/Band 2,171 nm), B: (Band 2,159 nm/ Band 2,171 nm). (Graph a) Example of continuum-removed reflectance spectra of poorly-ordered kaolinite found in the flood-plain facies. (Graph b) Example of continuum-removed reflectance spectra of well-ordered kaolinite found in the paleochannel facies. (Graph c) Example of continuum removed reflectance spectra of well-ordered kaolinite and calcite cement.

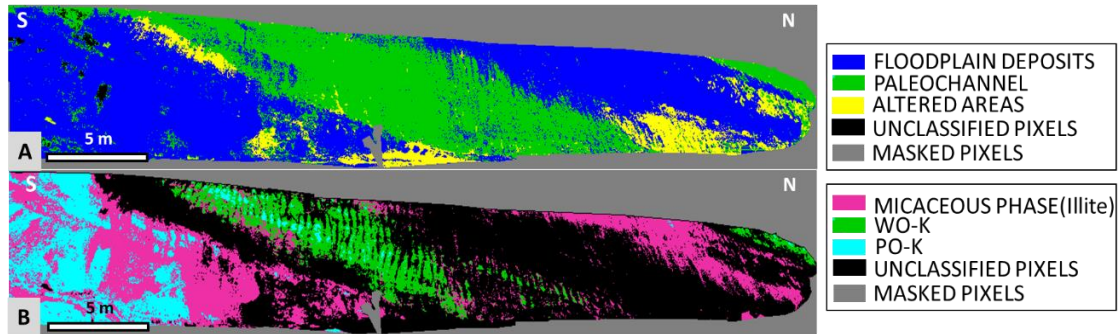


Figure 4-10 (a) SAM classification image of the S-N outcrop wall using ASD from collected hand samples. (b) SAM classification image of the S-N outcrop wall using U.S. Geological Survey spectral library of: micaceous phase: Illite, well-ordered kaolinite [WO-K], poorly-ordered kaolinite [PO-K], and calcite. The angular-similarity threshold was always lower than 0.1 radians and different for each endmember.

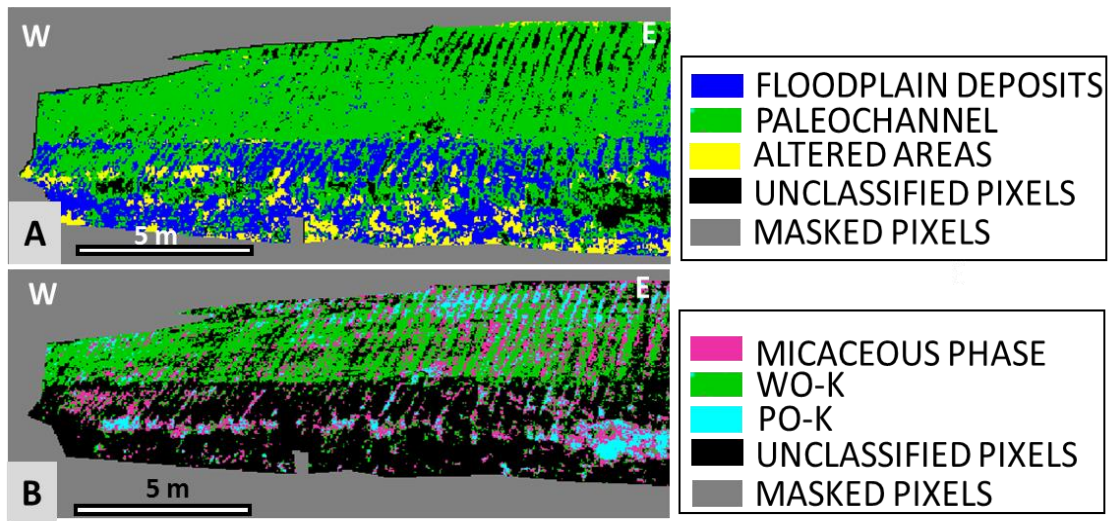


Figure 4-11 (a) SAM classification image of the W-E outcrop wall using spectral data of hand samples. (b) SAM classification image of the W-E outcrop wall using U.S. Geological Survey spectral library of: Micaceous phase: Illite, well-ordered kaolinite [WO-K], poorly-ordered kaolinite [PO-K], and calcite. The angular-similarity threshold was always lower than 0.1 radians and different for each endmember.

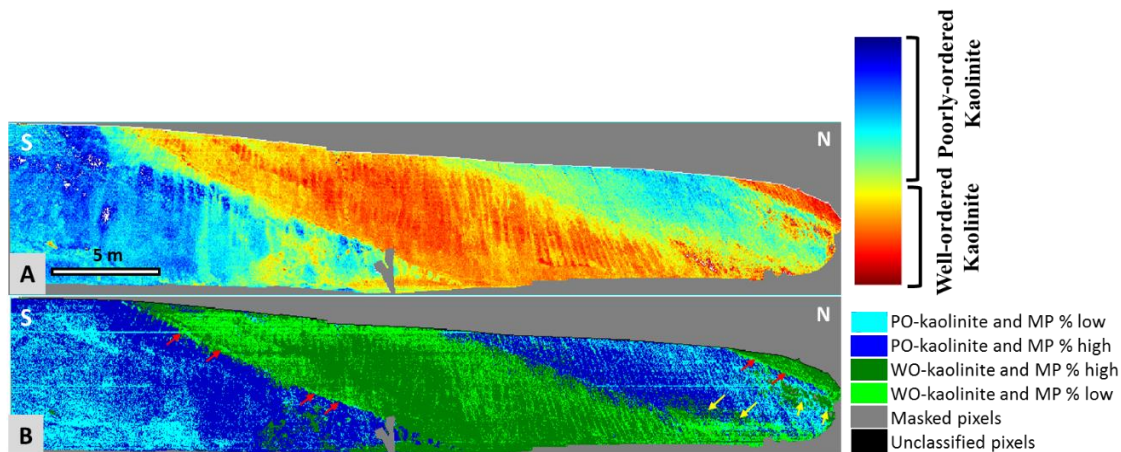


Figure 4-12 (a) “Kaolinite Crystallinity Index” resulting image for S-N outcrop of the Utrillas Formation. Warm colors are indicative of low values, thus presence of well-ordered kaolinite. Cold colors indicate high values, thus presence of poorly-ordered kaolinite. (b) “Micaceous phase-crystallinity Index” resulting image for S-N outcrop of the Utrillas Formation. Only pixels with 2,203 nm absorption feature depth greater than 0.95, of the continuum-removed image where used for classification. Abbreviations: PO-kaolinite and MP% low= poorly-ordered kaolinite and low-micaceous phase abundance, PO-kaolinite and MP% high= Poorly-ordered kaolinite and high-micaceous phase abundance, WO-kaolinite and MP% low= Well-ordered kaolinite and low-micaceous phase abundance, WO-kaolinite and MP% high= Well-ordered kaolinite and high-micaceous phase abundance.

Figure 4-12b and Figure 4-13b depicts the classified images using both the KCI and the MPAI. Light blue corresponds to areas where poorly-ordered kaolinite with a low concentration of micaceous phase was found, whereas dark blue presents areas with poorly-ordered kaolinite but high-micaceous phase concentration. Poorly-ordered kaolinite, with low and high abundance in micaceous phase was only present in the fine-grained flood-plain facies. On the other hand, light green corresponds to areas with well-order kaolinite with low-micaceous phase abundance, and dark green stands for well-ordered kaolinite with high-micaceous phase abundance (Figure 4-12b and Figure 4-13b). Well-ordered kaolinite was only present in the coarse grained paleochannel facies. Two thin beds (~10 cm), shown in light green, were observed at the contact between floodplain and paleochannel deposits (red arrow in Figure 4-12b). These layers were interpreted to be conglomeratic sandstone at the base of the

paleochannel facies with lower concentrations of micaceous phase. Yellow arrows in Figure 4-12b and Figure 4-13b, point to the irregular patchy areas where well-ordered kaolinite was present but does not follow the bedding. These areas correspond to the same pixels with an absorption minimum at $\sim 1,700$ nm and ~ 2300 nm and a high abundance of organic matter. Grey and black pixels match with masked and unclassified pixels.

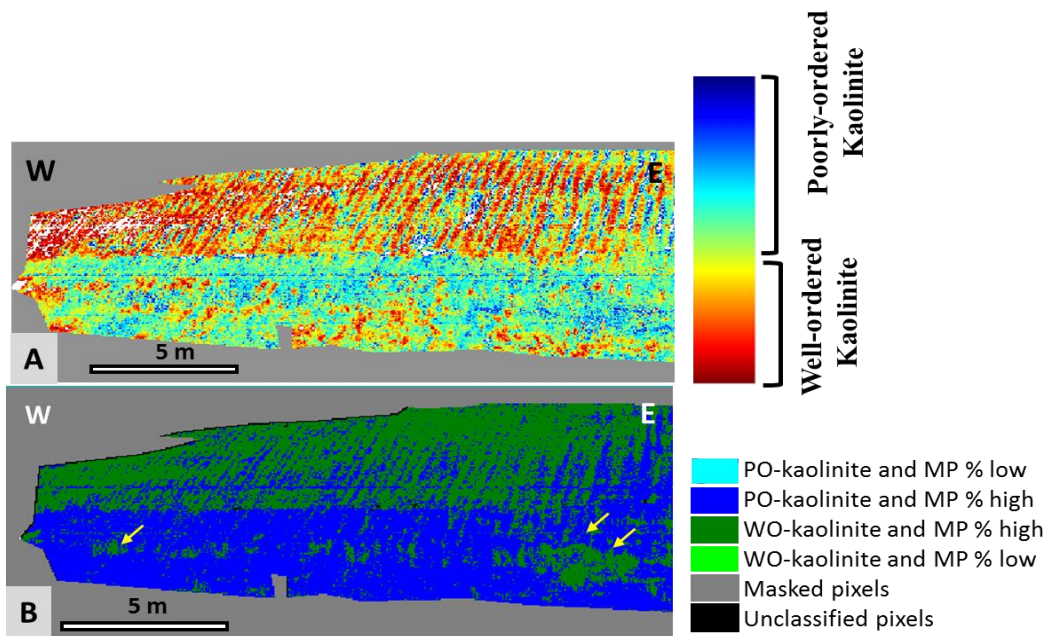


Figure 4-13 (a) "Kaolinite Crystallinity Index" image for W-E outcrop of the Utrillas formation. Warm colors are indicative of low values, thus presence of well-ordered kaolinite. Cold colors indicate high values, thus presence of poorly-ordered kaolinite. (b) "Micaceous phase-crystallinity Index" resulting image for W-E outcrop of the Utrillas Formation Only pixels with 2,203 nm absorption feature and depth greater than 0.95, of the continuum-removed image where used for classification. Abbreviations: PO-kaolinite and MP% low= poorly-ordered kaolinite and low-micaceous phase abundance, PO-kaolinite and MP% high= Poorly-ordered kaolinite and high-micaceous phase abundance, WO-kaolinite and MP% low= Well-ordered kaolinite and low-micaceous phase abundance, WO-kaolinite, MP% high= Well-ordered kaolinite, and high-micaceous phase abundance.

Based on the classification results from MPAI, ROI were created in the SWIR reflectance spectra image. The mean-reflectance spectra of the pixels included in each of the classes is

shown in Figure 4-14. In the right side of the graph, black arrows point out the distinctive characteristics of each endmember that were used for classification purposes.

In general, S-N outcrop image showed a much better result than W-E outcrop image. This could be because lighting conditions were much better at the S-N outcrop wall, with the sun directly perpendicular to the scanned area.

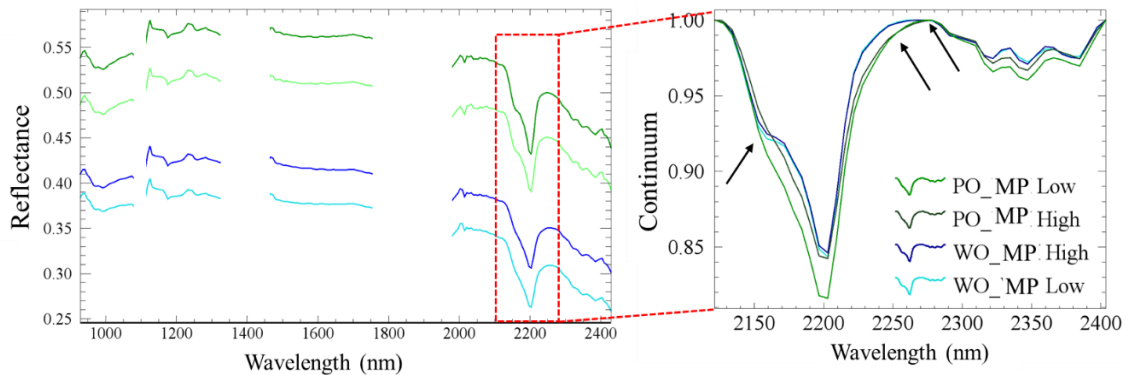


Figure 4-14 SWIR reflectance spectra of the results of MPAI results. (a) SWIR reflectance spectra. (b) Normalized SWIR reflectance spectra from 2120 nm- 2430 nm. Blank areas in the left side of graph correspond to water absorptions. Black arrows point out distinctive characteristics of each endmember. Abbreviations: PO-MP Low= poorly-ordered kaolinite and low-micaceous phase abundance, PO-MP High = Poorly-ordered kaolinite and high-micaceous phase abundance, WO_MP Low = Well-ordered kaolinite and low-micaceous phase abundance, WO_MP High= Well-ordered kaolinite and high-micaceous phase abundance.

4.4 PETROGRAPHY

As a test methodology to validate the hyperspectral data classification results, thirteen thin sections from hand specimens were analyzed and described. The sample distribution is shown in Figure 4-1. Main observations for each thin section and detailed point counting are described in Appendix A-1 & Appendix A-2. The Utrillas Formation is composed of very fine to medium, poorly-cemented sands, poorly-sorted and sub-angular to angular shape. The ternary diagram

suggests that the Utrillas Formation sandstones are subarkoses to quartzarenites with an average Q F R composition of $Q_{81}F_{16}R_3$ (Figure 4-15).

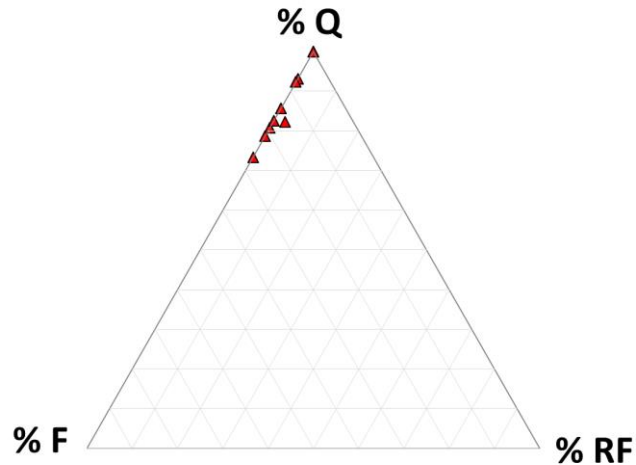


Figure 4-15 Q-F-RF compositional diagram of the sandstones from the Utrillas formation.

Based on the nomenclature proposed by Folk (1974) the paleochannel facies were described as fine to medium sand: kaolinite/illite-cemented siliceous immature muscovitic subarkoses. On the other hand, flood-plain deposit facies were classified as muscovitic kaolinite illite claystone.

The framework grains accounts for 75 % of the total rock volume. The majority of the grains were monocrystalline and polycrystalline quartz grains (80 %) with straight extinction to undulose extinction was observed. Idiomorphic high relief inclusions and trains of vacuoles were found, quartz overgrowth were sometimes present. Sub-rounded K-feldspar grains (microcline and orthoclase) (16 %) made up the framework constituents. They usually appeared altered into clay minerals (probably kaolinite) giving a brownish color. No plagioclase grains were observed in the samples. Tabular muscovite grains were usually bend (Figure 4-16a), and altered with low-birefringence clay mineral (kaolinite) (Figure 4-16a). Some muscovite grains appeared

completely altered showing pseudomorphs of muscovite grains. Few rounded sedimentary rock fragments and metamorphic fragments were found. Idiomorphic zircons and subangular tourmaline crystals were found as the accessory minerals. Rounded opaque and oxidized spots of organic matter and wood fragments were observed.

The sandstone matrix was composed of clay minerals (5 %). It is mainly composed of low- and high- birefringence clay minerals, probably kaolinite and illite in some cases mixed together. When illite was present, it appeared oriented in two preferential directions. Kaolinite and illite were hard to differentiate in the claystones (Figure 4-16b). Marfil & Gomez-Gras (1992) & Arostegui et al. (2000) reported the presence of microcrystalline quartz in the matrix, but this could not be verified by independent microscopic observation.

In coarser grain-size samples, primary pores were filled by authigenic kaolinite that shows mainly fan-like shapes (Figure 4-16c&d). Illite and quartz overgrowths were minor cement phases. Goethite and hematite cement were present in some samples, staining the samples in reddish colors (Figure 4-16d). The cement oxides that were present in sample Can-L are much darker than the one existing in samples CAN-M, Can-E, Can-1, or Can-9 (Figure 4-16e). Marfil & Gomez-Gras (1992), described the presence of calcite, dolomite, anhydrite, and barite cements, but could not be found in these samples.

Secondary porosity was 6.5 % of the total samples, however, the breakability of the samples suggests that the observed porosity could be larger than primary porosity of the rock. In finer-grain size samples porosity was rare.

The presence of different types of kaolinites in the Utrillas Formation is facies-dependent. Based on the petrographic studies and previous work (Marfil & Gomez-Gras 1992; Arostegui et

al. 2000), authigenic well-ordered kaolinites were found as the primary pore filling in the paleochannel facies with very low abundance of illite. The majority of the muscovite grains show a certain grade of kaolinization. On the other hand, in flood-plain deposits, the matrix was mainly composed of poorly-ordered kaolinite and Illite in different abundances. Muscovite grains were found.

Although most of the claystone appeared massive, in sample Can-P lamination was described. Various layers of claystones interbedded with siltstones were recognized (Figure 4-16).

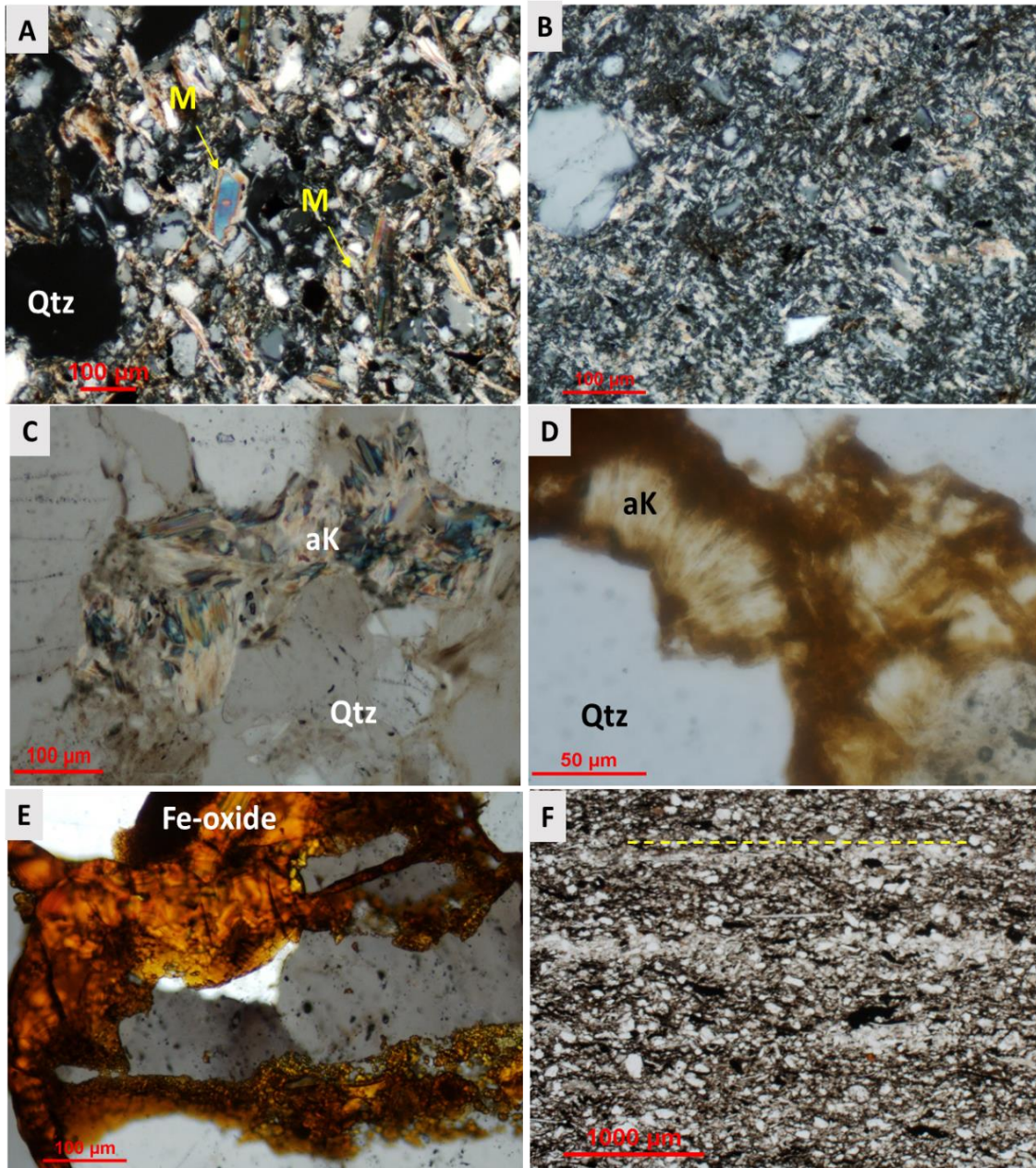


Figure 4-16 Photomicrographs of samples from the Utrillas Formation. (a) Fan-shape authigenic kaolinites growing at the edge of a monocrystalline quartz grain with straight extinction in sample Can-9 in plain light. (b) Poorly-sorted sandstone with micas bent and broken at the edges of the grains replaced by kaolinite in sample Can-2 in crossed nicols. (c) Pore-filling authigenic kaolinite in sample Can-9 in crossed nicols. (d) Fe-oxide cement (goethite) surrounded by a monocrystalline angular-quartz grain with undulose extinction in crossed nicols. (Can-M). (e) Laminated mudstone in sample Can-9 in crossed nicols. (f) Claystone in sample Can-F in crossed nicols. Qtz=quartz, M=Muscovite, ak=authigenic kaolinite, Yellow dashed indicated direction of lamination.

The main diagenetic events observed from the petrographic studies at the Utrillas Formation are: (1) quartz cement as quartz overgrowths, (2) kaolinization of feldspars and muscovite grains edges, (3) pore filling authigenic kaolinite showing a fan-shape pattern, (4) illite-kaolinite matrix coexisting (maybe due to the illitization of kaolinite described by (Marfil & Gomez-Gras 1992; Arostegui et al. 2001), and (5) Fe-iron oxides cement.

4.5 DISCUSSION

The Utrillas Formation at Basconillos del Tozo is composed of fine to medium sub-arkoses with a mean composition of $Q_{81}F_{16}R_3$. An erosive surface mark the boundary between each depositional cycle. At the bottom of each sequence, cross-stratified fine to medium sandstones layers (~5 m thick) were interpreted to be paleochannel from a meandering river (sinuosity >1.7). This paleochannels are capped with conformably overlaying claystone package (~5 m thick) interpreted as floodplain deposits. This interpretation is aligned with the nature of the upper Member (U2) of the Utrillas Formation in a northeastern region (Pancorbo) (Arostegui et al. 2000) and southern region (Umbral de Ateca, Soria) (Marfil & Gomez-Gras 1992).

Although, spectral and spatial resolution of spectroradiometer-point data and close-range hyperspectral data were different, they were proven to be highly comparable at least in SWIR part of the spectra (Figure 4-3).

Patches of well-ordered kaolinite in the flood-plain deposits correspond to darker altered areas related to high abundance of organic matter and the presence of native sulphur at the surface. This irregular alteration areas only occur in the flood-plain deposits and might be associated with a later diagenetic process due to the combination of organic acids, CO_2 , and H_2S due to microbial activity and hydrocarbon oxidation near the subsurface (Schumacher 1996).

Different processes of diagenesis such as transformation of illite into authigenic kaolinite, precipitation of pyrite, and sulfur presence (previously reported in Utah's Lisbon Valley field, Cement-Chickasha field in Oklahoma, and Turkey Creek oil seep near Denver) were associated with hydrocarbon seepages (Schumacher 1996). Marfil & Gomez-Gras, (1992); Petrovic et al. (1992); and Sun & Khan (2016) associated the authigenesis of kaolinite with meteoric waters in an early phase of diagenesis (eodiagenesis) and acidic water flux due the maturation of organic matter. On the other hand, Arostegui et al., (2000) suggested that only meteoric water is the cause of the alteration of feldspar and mica, and yet precipitation of authigenic kaolinite. This study suggests that during diagenesis, the alteration of feldspars and micas may have started the precipitation of well-ordered kaolinite but contemporary subsurface microbial activity might cause the formation of authigenic kaolinite in organic rich areas due to the local acidification of interstitial water.

Developed KCI and MPAl indexes proved to be efficient and useful for quantifying kaolinite crystallinity and micaceous phase (illite and muscovite) abundances. On the other hand, reflectance spectra of illite and muscovite are similar in the SWIR, so this technique fails to distinguish them.

Outcrop images were classified using the SAM technique utilizing pure endmembers for minerals from the U.S. Geologic Survey spectral library. Both SAM, KCI, and MPAl results show the presence of well-ordered kaolinite in samples of the paleochannel facies, whereas flood-plain deposits are composed of poorly-ordered kaolinite and micaceous phase. In the MPAl results, a thinner layer at the bottom of the second depositional cycle was interpreted as a coarser-grain size conglomeratic layer.

Hyperspectral results suggest that authigenic kaolinite with high crystallinity (Bauluz et al. 2008) is only present at the sandstone layers mixed with different abundance of muscovite transported grains. Whereas, detrital kaolinite with low crystallinity (Bauluz et al. 2008) is mainly present in claystone layers mixed with different abundance of micaceous phase.

In the Basconcillos del Tozo outcrop, the relative abundance of each facies was determined. The S-N outcrop is composed of 56 % of floodplain facies, 36 % paleochannel facies, and 8 % of altered areas. Whereas, W-E outcrop is composed of 25 % of floodplain facies, 67 % of paleochannel facies, and 0.2 % of altered areas as shown in Figure 4-17. Overall, The Utrillas Formation wall exposures at Basconcillos del Tozo quarry are composed of 214 m² of paleochannel facies, 235 m² of floodplain facies, and 36 m² of altered areas.

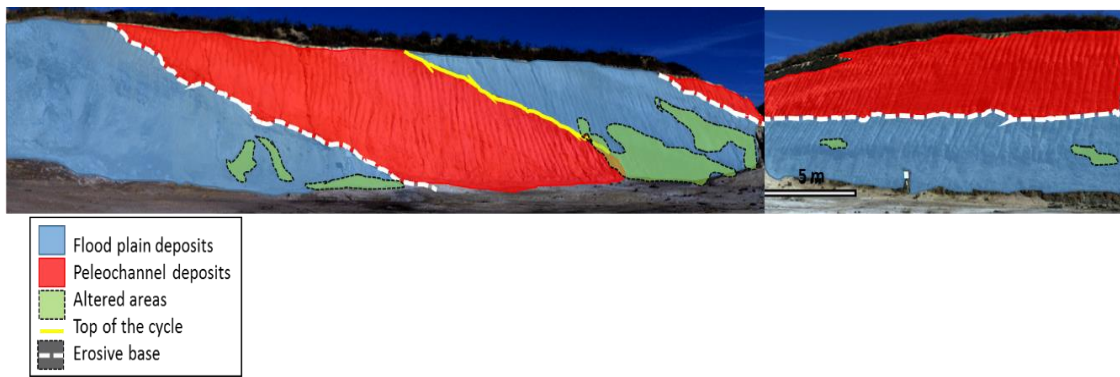


Figure 4-17 Facies interpretation of the Utrillas Formation outcrop based on SWIR classification methodologies.

SAM classified images using U.S. Geological Survey spectra library show the presence of well-ordered kaolinite in samples Can-2, Can-3, and Can-9. Results from KCI and MPAl show that well-ordered kaolinite with different abundance in micaceous phase in samples Can-2, Can-3, Can-9, Can-E, Can-L, and Can-M. At the same time, petrographic analysis of samples Can-9 and Can-M suggest the presence of well-ordered authigenic kaolinites with a low fraction of

muscovite flakes, whereas, samples Can-2 and Can-3 show a slightly greater abundance in muscovite detrital grains. Petrographic analysis were aligned with hyperspectral results and showed that authigenic kaolinite with high crystallinity (Bauluz et al. 2008) is only present in the sandstone layers mixed with different abundance of muscovite transported grains [Can-2, Can-3, Can-9, and Can-M].

SAM classification using U.S. Geological Survey spectral library suggest the presence of either poorly-ordered kaolinite or micaceous phase in samples; Can-A, Can-B, Can-C, Can-D, Can-F, and Can-E. When KCI and MPAI indexes were applied, samples Can-A, Can-B, Can-D, and Can-E were composed of poorly-ordered kaolinite with the greatest abundance of micaceous phase. On the other hand, samples Can-1, Can-E, Can-F, and Can-P (micro layered) were suggested to be composed of poorly-ordered kaolinite with low abundance of micaceous phase.

CHAPTER 5

5. CONCLUSIONS

Image spectroscopy is proven to be a powerful and nondestructive technique for geochemical and multi-scale characterization of compositional and mineralogical variations at the outcrop and laboratory settings. The advantages vs. disadvantages of imaging spectroscopy application to outcrops studies, in comparison with traditional techniques is compiled on Table 5-1.

Table 5-1 Advantages vs. disadvantages of imaging spectroscopy applied to sandstone outcrop studies.

ADVANTAGES
<ul style="list-style-type: none">• Non-destructive technique.• Quick, less expensive and objective technique that can reveal information about vertical and horizontal geochemical variations• Outcrop and laboratory data can be combined.• Geochemical study of inaccessible areas.• Facies distribution and mineral relative abundance mapping with centimeter resolution.
DISADVANTAGES
<ul style="list-style-type: none">• Shadowed areas and darker materials are still a problem for classification.• Only minerals that show characteristics absorption minimum can be identified.• For best results, images should be acquired in optimum light condition• Until now, lack of standardized methodology for image preprocessing hampered its use.

In this study, datasets with different spectral and spatial resolutions were combined to extract information about diagenesis in deltaic and fluvial sandstones. The high accuracy of laboratory spectral data allowed a precise mineralogical characterization, which was compared with other techniques, such as thin section analysis.

Darker materials (e.g., distal facies and chlorite in the Frontier Formation and altered areas in the Utrillas Formation) have lower overall reflectance values, due to the low emitted reflectance. Therefore, the classification of these endmembers was usually more difficult and sometimes absorption features were attenuated. The same problem was encountered in shadowed areas. Shadows and light differences produced by the sun's angle and the outcrop wall was a problem in this kind of studies. Atmospheric effects and large spatial variability could be problematic for automatic analysis of the data (Melgani & Bruzzone 2004). If the dataset is not carefully studied and processed, these issues might lead to a misclassification. In the near future, new cameras with their own source of light might automatically correct these issues.

The lack of standardized methodology in the hyperspectral data preprocessing need to be solved (Asadzadeh & de Souza Filho 2016). Hyperspectral data collection campaigns should be carefully planned in advance, taking into account outcrop direction and lighting conditions. For example, to scan vertical walls, dawn and dusk are the best hours when the sun is more perpendicular to the wall.

The study of Parasequence # 6 of the Frontier Formation at Raptor Ridge revealed that better classification results were achieved when using spectra from the image itself. Classification results using ASD spectra and hyperspectral data collected in the laboratory were still comparable but far less accurate. Reflectance spectral studies revealed that calcite cement is homogeneously distributed within concretions in channel facies and is the major diagenetic constituent. Whereas, concretions at the bar facies present a more heterogeneous distribution with non-calcite interbedded layers following the direction of the bedding. Normalized (shadowing and unclassified-removed pixels) classification results showed that the outcrop wall was composed of approximately 87 m² of bar facies, 150 m² of channel facies, 11.6 m² of distal

facies, and 26.7 m² of carbonate concretions. Previous sedimentological studies suggest very similar percentages (Lee et al. 2007; Nyman et al. 2014).

Field and petrographic observations at the Utrillas Formation at Basconillos del Tozo suggested that it is part of the upper member in the Umbral de Ateca, Soria and Pancorbo, Burgos. Classified image using the reflectance spectra of hand samples revealed that the S-W outcrop wall is composed of 128 m² of paleochannel facies, 202 m² of floodplain deposits, and 28 of m² altered areas. The, W-E outcrop wall is composed of 85 m² of paleochannel facies, 32 m² of floodplain deposits, and 8 m² of altered areas.

Crystallinity of kaolinite was obtained by the Hinckley Index, derived from XRD data (Hinckley 1963). This study successfully used the KCI and MPAI indexes to resolve the crystallinity of kaolinite, and its relative abundance when kaolinite is mixed with micaceous phase at the outcrop. Classification results with KCI and MPAI indexes were comparable with SAM classification results using clay mineral spectral endmembers from the U.S. Geological Survey spectral library.

According to the classification results using these indexes, paleochannel facies were found to be composed of well-ordered kaolinite with different abundance in micaceous phase, possibly related to the presence of muscovite. Flood-plain deposits, were composed of poorly-ordered kaolinite and micaceous phase (i.e., Illite). The presence of an absorption minimum at ~1,700 nm and ~2,300 nm at some altered areas might indicate bitumen. These areas are generally darker in color and are stained with Fe-oxides.

Close-range hyperspectral studies could be systematically applied as a routine technique for reservoir characterization, mining, or soil and water pollution studies. For example, in the

mining industry well-ordered kaolinite deposits are known as china clays. On the other hand, poorly-ordered kaolinite is known as ball clay or refractory clays. Each of them have different uses and economic values (Evans 1993). Close-range hyperspectral remote sensing could be applied as a systematic technique for facies characterization, hence better outcrop evaluation of crystallinity of kaolinites.

For years to come, cameras will become smaller and more user friendly. Therefore, VNIR and SWIR hyperspectral images could be integrated to geologic studies and become an essential field tool that will allow geologists to increase the accuracy of field studies allows for detailed mapping in difficult to access areas.

REFERENCES

- AGGEP. (2015). *El Campo de Petroleo de Ayoluengo (Burgos) 50 años de Historia*. Geología, 9 de mayo de 2015, Burgos, 32p.
- Aguilar, M. J., Ramirez del Pozo, J., & Riba, O. (1971). Algunas precisiones sobre la sedimentacion y paleoecologia del Cretacico Inferior de la zona de Utrillas-Villarroya de los Pinares (Teruel). *Estudios Geológicos*, 27, 497–512.
- Arostegui, J., Irabien, M. J., Sangüesa, J., & Zuluaga, M. C. (2000). La formacion de Utrillas en el borde sur de la Cuenca Vasco-Cantabrica: aspectos estratigráficos, mineralogicos. *Estudios Geológicos*, 56, 251–267.
- Arostegui, J., Irabien, M. J., Fernando, N., Sanguesa, J., & Zuluaga, M. C. (2001). Microtextures and the origin of muscovite - kaolinite intergrowths. *Clay Minerals*, 49(6), 529–539.
- Asadzadeh, S., & de Souza Filho, C. R. (2016). A review on spectral processing methods for geological remote sensing. *International Journal of Applied Earth Observation and Geoinformation*, 47, 69–90.
- Bauluz, B., Mayayo, M. J., Yuste, A., & González López., J. M. (2008). Genesis of kaolinite from Albian sedimentary deposits of the Iberian Range (NE Spain): analysis by XRD, SEM and TEM. *Clay Minerals*, 43(3), 459–475.
- Bell, J. H., Bowen, B. B., & Martini, B. A. (2010). Imaging spectroscopy of jarosite cement in the Jurassic Navajo Sandstone. *Remote Sensing of Environment*, 114(10), 2259–2270.
- Beroiz, C., & Permanyer, A. (2011). Hydrocarbon habitat of the Sedano Trough, Basque-Cantabrian Basin, Spain. *Journal of Petroleum Geology*, 34(4), 387–409.
- Bhattacharya, J. P., & Willis, B. J. (2001). Lowstand deltas in the Frontier Formation, Powder River Basin, Wyoming: Implications for sequence stratigraphic models. *AAPG Bulletin*, 85(2), 261–294.
- Bishop, J. L., Lane, M. D., Dyar, M. D., & Brown, A. J. (2008). Reflectance and emission spectroscopy study of four groups of phyllosilicates: smectites, kaolinite-serpentine, chlorites and micas. *Clay Minerals*, 43(1), 35–54.
- Boardman, J. W. (1998). Leveraging the high dimensionality of AVIRIS data for improved sub-pixel target unmixing and rejection of false positives: Mixture Tuned Matched Filtering. In *7th Annual JPL Airborne Geoscience Workshop*, 1998, Pasadena, CA.
- Boesche, N., Rogass, C., Lubitz, C., Brell, M., Herrmann, S., Mielke, C., Kaufmann, H. (2015). Hyperspectral REE (Rare Earth Element) Mapping of outcrops—applications for neodymium detection. *Remote Sensing*, 7(5), 5160–5186.

- Bolin, B. J., & Moon, T. S. (2003). Sulfide detection in drill core from the Stillwater Complex using visible/near-infrared imaging spectroscopy. *Geophysics*, 68(5), 1561.
- Bowitz, J., & Ehling, A. (2008). Non-destructive infrared analyses: A method for provenance analyses of sandstones. *Environmental Geology*, 56(3-4), 623–630.
- Buckley, S. J., Kurz, T. H., Howell, J. A., & Schneider, D. (2013). Terrestrial lidar and hyperspectral data fusion products for geological outcrop analysis. *Computers and Geosciences*, 54, 249–258.
- Canerot, J., Hudec, M. R., & Rockenbauch, K. (2005). Mesozoic diapirism in the Pyrenean Orogen: salt tectonics on a transform plate boundary. *AAPG Bulletin*, 89(2), 211–229.
- Chayes, F. (1956). *Petrographic modal analysis*. New York: Wiley, 113p.
- Clark, R. N., King, T. V. V., Klejwa, M., Swayze, G. A., & Vergo, N. (1990). High spectral resolution reflectance spectroscopy of minerals. *Journal of Geophysical Research*, 95, 12653-12680.
- Clark, R. N. (1999). Spectroscopy of rocks and minerals, and principles of spectroscopy. In A. N. Rencz (Ed.), *Remote Sensing for the Earth Sciences* (3rd ed., pp. 3–58). New York, USA: John Wiley and Sons.
- Clark, R. N., Swayze, G. A., Wise, R., Livo, E., Hoefen, T., Kokaly, R., & Sutley, S. J. (2007). *USGS digital spectral library splib06a*. (U.S. Geological Survey, Digital Data Series 231).
- Cudahy, T. (1997). PIMA-II spectral characteristics of natural kaolins. *CSIRO/AMIRA Project 435*. CSIRO, Division of Exploration and Mining, Australia.
- Denk, M., Glaber, C., Kurz, T. H., Buckley, S. J., & Drissen, P. (2015). Mapping of iron and steelwork by-products using close range hyperspectral imaging: A case study in Thuringia, Germany. *European Journal of Remote Sensing*, 48, 489-509.
- Dutton, S. P., Willis, B. J., White, C. D., & Bhattacharya, J. P. (2000). Outcrop characterization of reservoir quality and interwell-scale cement distribution in a tide-influenced delta, Frontier Formation, Wyoming, USA. *Clay Minerals*, 35, 95–95.
- Dutton, P. S., White, C. D., Willis, B. J., Dutton, S. P., John, A., & Jackson, K. G. (2002). Calcite cement distribution and its effect on fluid flow in a deltaic sandstone, Frontier Formation, Wyoming. *AAPG Bulletin*, 86(12), 2007–2021.
- Evans, A. M. (1993). *Ore Geology and Industrial Minerals*. (Third). Victoria, Australia: Blackwell Science Ltd., 400p.
- Folk, R. L. (1974). *Petrology of Sedimentary Rocks*. Austin, Texas: Hemphill Publishers, 159 p.

- Gaffey, S. J. (1986). Spectral reflectance of carbonate minerals in the visible and near infrared (0.35-2.55 microns): calcite, aragonite, and dolomite. *American Mineralogist*, 71(1-2), 151–162.
- Gaffey, S. J. (1987). Spectral reflectance of carbonate minerals in the visible and near infrared (0.35-2.55um): Anhydrous Carbonate Minerals. *Journal of Geophysical Research*, 92, 1429–1440.
- Gallie, E. A., McArdle, S., Rivard, B., & Francis, H. (2002). Estimating sulphide ore grade in broken rock using visible/infrared hyperspectral reflectance spectra. *International Journal of Remote Sensing*, 23(11), 2229–2246.
- Gani, M. R. (2005). *3-D facies architecture of river deltas: Lessons from the Turoinian Wall Creek Member, Central Wyoming, USA*. Ph.D Dissertation. The University of Texas at Dallas, 149p.
- Gani, M. R., & Bhattacharya, J. P. (2007). Basic building blocks and process variability of a Cretaceous Delta: internal facies architecture reveals a more dynamic interaction of river, wave, and tidal processes than is indicated by external shape. *Journal of Sedimentary Research*, 77(4), 284–302.
- Gani, M. R., Bhattacharya, J. P., & MacEachern, J. A. (2008). Using ichnology to determine the relative influence of waves, storms, tides, and rivers in deltaic deposits: examples from Cretaceous Western Interior Seaway, U.S.A. in MacEachern, J.A., Bann, K.L., Gingras, M.K., and Pemberton, S.G., eds., *Applied Ichnology, SEPM Short Course Notes*, 209-225.
- Goetz, A. F. H., Vane, G., Solomon, J. E., & Rock, B. N. (1985). Imaging spectrometry for earth remote sensing. *Science*, 228, 1147–1153.
- Green, A. A., Berman, M., Switzer, P., & Craig, M. D. (1988). Transformation for ordering multispectral data in terms of image quality with implications for noise removal. *IEEE Transactions on Geoscience and Remote Sensing*, 26(1), 65–74.
- Haest, M., Cudahy, T., Laukamp, C., & Gregory, S. (2012). Quantitative mineralogy from infrared spectroscopic data. I. Validation of mineral abundance and composition scripts at the rocklea channel iron deposit in Western Australia. *Economic Geology*, 107(2), 209–228.
- Hassouta, L., Buatier, M. D., Potdevin, J. L., & Liewig, N. (1999). Clay diagenesis in the sandstone reservoir of the Ellon Field (Alwyn, North Sea). *Clays and Clay Minerals*, 47(3), 269–285.
- Hecker, C., Van Der Meijde, M., Van Der Werff, H., & Van Der Meer, F. D. (2008). Assessing the influence of reference spectra on synthetic SAM classification results. *IEEE Transactions on Geoscience and Remote Sensing*, 46(12), 4162–4172.
- Hinckley, D. N. (1963). Variability in "crystalinity" values among the kaolin deposits of the Coastal Plain of Georgia and South Carolina. *Clays and Clay Minerals*, 11, 229-235.

- Hörig, B., Kühn, F., Oschütz, F., & Lehmann, F. (2001). HyMap hyperspectral remote sensing to detect hydrocarbons. *International Journal of Remote Sensing*, 22(8), 1413–1422.
- Hunt, G. R., & Salisbury, J. W. (1970). Visible and near-infrared spectra of minerals and rocks; I, silicate minerals. *Mod. Geol.*, 1(7), 283–300.
- ITGE (1994). *Mapa Geologico de España, 1:50.000, Hoja 134, Polientes, Memoria*.
- Krupnik, D., Khan, S. D., Okyay, U., Hartzell, P., Zhou, H. (2016). Study of Upper Albian rudist buildups in the Edwards Formation using ground-based hyperspectral imaging and terrestrial laser scanning. *Sedimentary Geology*, 345, 154-167.
- Kruse, F. A. (1996). Identification and mapping of minerals in drill core using hyperspectral image analysis of infrared reflectance spectra. *International Journal of Remote Sensing*, 17(9), 1623–1632.
- Kruse, F. A., Weatherbee, O., Peppin, W., Bedell, R., Calvin, W., & Taranik, J. V. (2010). HSI mineral mapping from airborne, outcrop, and drill-core perspectives. In W. T. I. S. for O. E. FL (Bellingham (Ed.), *In Proceedings of the SPIE Symposium on Defense & Security Proceedings of the SPIE Symposium on Defense & Security*. Orlando.
- Kruse, F.A., Bedell, R. L., Taranik, J. V., Peppin, W. A., Weatherbee, O., & Calvin, W. M. (2012). Mapping alteration minerals at prospect, outcrop and drill core scales using imaging spectrometry. *International Journal of Remote Sensing*, 33(6), 1780–1798.
- Kühn, F., Oppermann, K., & Hörig, B. (2004). Hydrocarbon Index – an algorithm for hyperspectral detection of hydrocarbons. *International Journal of Remote Sensing*, 25(12), 2467–2473.
- Kurz, T. H., Buckley, S. J., Howell, J. A., & Schneider, D. (2008). Geological outcrop modelling and interpretation using ground based hyperspectral and laser scanning data fusion. The international archives of the photogrammetry. *Remote Sensing and Spatial Information Science*, 37(8), 1229-1234.
- Kurz, T. H., Buckley, S. J., Howell, J. A., & Schneider, D. (2009). Close range hyperspectral and lidar data integration for geological outcrop analysis. In *Proceedings of First Workshop on Hyperspectral Image and Signal Processing: Evolution in Remote Sensing, 2009 (WHISPERS '09)*, 26-28th August, 2009. Grenoble, France.
- Kurz, T. H., Dewit, J., Buckley, S. J., Thurmond, J. B., Hunt, D. W., & Swennen, R. (2012a). Hyperspectral image analysis of different carbonate lithologies (limestone, karst and hydrothermal dolomites): The Pozalagua Quarry case study (Cantabria, North-west Spain). *Sedimentology*, 59(2), 623–645.

- Kurz, T. H., Buckley, S. J., & Howell, J. A. (2012b). Close range hyperspectral imaging integrated with Terrestrial Lidar Scanning applied to rock characterisation at centimetre scale. *ISPRS - International Archives of the Photogrammetry, Remote Sensing and Spatial Information Sciences*, 39(5), 417–422.
- Kurz, T. H., Buckley, S. J., & Howell, J. A. (2013). Close-range hyperspectral imaging for geological field studies: workflow and methods. *International Journal of Remote Sensing*, 34(5), 1798–1822.
- Lee, K., Gani, M. R., McMechan, G. A., Bhattacharya, J. P., Nyman, S. L., & Zeng, X. (2007). Three-dimensional facies architecture and three-dimensional calcite concretion distributions in a tide-influenced delta front, Wall Creek Member, Frontier Formation, Wyoming. *AAPG Bulletin*, 91(2), 191–214.
- Marfil, R., & Gomez-Gras, D. (1992). Procedencia y modelo diagenetico de las areniscas de Facies Utrillas en la Cordillera Iberica (Umbral de Ateca) y la Meseta Norcastellana. *Rev. Soc. Geol. España*, 5(3-4), 101–115.
- McKeown, N. K., Bishop, J. L., Cuadros, J., Hillier, S., Amador, E., Makarewicz, H. D.,. (2011). Interpretation of reflectance spectra of clay mineral-silica mixtures: Implications for Martian clay mineralogy at Mawrth Vallis. *Clays and Clay Minerals*, 59(4), 400–415.
- Melgani, F., & Bruzzone, L. (2004). Classification of hyperspectral remote sensing. *IEE Transactions on Geoscience and Remote Sensing*, 42(8), 1778–1790.
- Merewether, E. (1996). Stratigraphy and tectonic implications of Upper Cretaceous rocks in the Powder River Basin, northeastern Wyoming and southeastern Montana. *US Geological Survey Bulletin*, 1917, 1–104.
- Meunier, R. C. (2005). *Clays*. Berlin: Springer, 472p.
- Miall, A. D. (1996). *The Geology of Fluvial Deposits (First)*. Toronto, Canada: Springer, 528p.
- Murphy, R. J., Monteiro, S. T., & Schneider, S. (2012). Evaluating classification techniques for mapping vertical geology using field-based hyperspectral sensors. *IEEE Transactions on Geoscience and Remote Sensing*, 50(8), 3066–3080.
- Murphy, R. J., & Monteiro, S. T. (2013). Mapping the distribution of ferric iron minerals on a vertical mine face using derivative analysis of hyperspectral imagery (430-970nm). *ISPRS Journal of Photogrammetry and Remote Sensing*, 75, 29–39.
- Murphy, R. J., Schneider, S., & Monteiro, S. T. (2014). Mapping layers of clay in a vertical geological surface using hyperspectral imagery: variability in parameters of SWIR absorption features under different conditions of illumination. *Remote Sensing*, 6(9), 9104–9129.

- Nyman, S. L., Gani, R. M., Bhattacharya, J. P., & Lee, K. (2014). Origin and distribution of calcite concretions in Cretaceous Wall Creek Member, Wyoming: Reservoir-quality implication for shallow-marine deltaic strata. *Cretaceous Research*, *48*, 139–152.
- Okyay, U., & Khan, S. D. (2016). Remote detection of fluid-related diagenetic mineralogical variations in the Wingate Sandstone at different spatial and spectral resolutions. *International Journal of Applied Earth Observation and Geoinformation*, *44*, 70–87.
- Petrovic, A., Khan, S. D., & Thurmond, A. K. (2012). Integrated hyperspectral remote sensing, geochemical and isotopic studies for understanding hydrocarbon-induced rock alterations. *Marine and Petroleum Geology*, *35*(1), 292–308.
- Ramírez del Pozo, J. (1969). *Síntesis estratigráfica y micropaleontológica de las facies Purbeck y Wealdense del Norte de España*. Madrid: CEPSA S.A., 68p.
- Rodger, A., Laukamp, C., Haest, M., & Cudahy, T. (2012). A simple quadratic method of absorption feature wavelength estimation in continuum removed spectra. *Remote Sensing of Environment*, *118*, 273–283.
- Rojas, M., Dopido, I., Plaza, A., & Gamba, P. (2010). Comparison of support vector machine-based processing chains for hyperspectral image classification. *Proc. of SPIE*, *7810*, 1–12.
- Savitzky, A., & Golay, M. J. E. (1964). Smoothing and differentiation of data by simplified least squares procedures. *Analytical Chemistry*, *36*(8), 1627–1639.
- Schneider, S., Murphy, R. J., & Melkumyan, A. (2014). Evaluating the performance of a new classifier – the GP-OAD: A comparison with existing methods for classifying rock type and mineralogy from hyperspectral imagery. *ISPRS Journal of Photogrammetry and Remote Sensing*, *98*, 145–156.
- Schumacher, D. (1996). Hydrocarbon-induced alteration of soils and sediments. *AAPG Memoir*, *66*, 71–89.
- Smith, G. M., & Milton, E. J. (1999). The use of the empirical line method to calibrate remotely sensed data to reflectance. *International Journal of Remote Sensing*, *20*(13), 2653–2662.
- Snyder, C. J., Khan, S. D., Bhattacharya, J. P., Glennie, C., & Seepersad, D. (2016). Thin-bedded reservoir analogs in an ancient delta using terrestrial laser scanner and high-resolution ground-based hyperspectral cameras. *Sedimentary Geology*, *342*, 154–164.
- Sun, L., and Khan, S. D.(2016). Ground-based hyperspectral remote sensing of hydrocarbon-induced rock alterations at cement, Oklahoma. *Marine and Petroleum Geology*, *77*, 1243-1253.

- Taylor, G. S. (2000). Mineral and lithology mapping of drill core pulps using visible and infrared spectrometry. *Natural Resources Research*, 9(4), 257–268.
- Taylor, K. G., & Machent, P. G. (2011). Extensive carbonate cementation of fluvial sandstones: An integrated outcrop and petrographic analysis from the Upper Cretaceous, Book Cliffs, Utah. *Marine and Petroleum Geology*, 28(8), 1461–1474.
- Van der Meer, F. (1995). Spectral reflectance of carbonate mineral mixtures and bidirectional reflectance theory: quantitative analysis techniques for application in remote sensing. *Remote Sensing Reviews*, 13, 67–94.
- Van der Meer, F., De Jong, S., B., & W. (2001). Imaging spectrometry: basic principles and prospective applications. *Kluwer Academic Publishers*, pp. 17–61. (F. Van der Meer & D. Jong, Eds.). Dordrecht, The Netherlands.
- Van der Meer, F. (2004). Analysis of spectral absorption features in hyperspectral imagery. *International Journal of Applied Earth Observation and Geoinformation*, 5(1), 55–68.
- Willis, B. J., Bhattacharya, J. P., Gabel, S. L., & White, C. D. (1999). Architecture of a tide-influenced river delta in the Frontier Formation of central Wyoming, USA. *Sedimentology*, 46(4), 667–688.
- Wiltschko, D. V., & Dorr, J. A. (1983). Timing of deformation in Overthrust Belt and Foreland of Idaho, Wyoming, and Utah. *American Association of Petroleum Geologists Bulletin*, 67(8), 1304–1322.
- Zaini, N. (2009). *Calcite-dolomite mapping to assess dolomitization patterns using laboratory spectra and hyperspectral remote sensing : A case study of Bédarieux mining area , SE France*. Master Thesis. International Institute of Geo-Information Science and Earth Observation.
- Zaini, N., Van der Meer, F., & van der Werff, H. (2012). Effect of grain size and mineral mixing on carbonate absorption features in the SWIR and TIR wavelength regions. *Remote Sensing*, 4(4), 987–1003.
- Zaini, N., Van der Meer, F., & Van der Werff, H. (2014). Determination of carbonate rock chemistry using laboratory-based hyperspectral imagery. *Remote Sensing*, 6(5), 4149–4172.
- Zhang, G., Wasyluk, K., & Pan, Y. (2001). The characterization and quantitative analysis of clay minerals in the Athabasca basin, Saskatchewan: Application of shortwave infrared reflectance spectroscopy. *Canadian Mineralogist*, 39(5), 1347–1363.

Zhouyu, F., Caelli, T., Nianjun, L., & Robles-Kelly, A. (2006). Boosted band ratio feature selection for hyperspectral image classification. *Proceedings - International Conference on Pattern Recognition*, 1(1), 1059–1062.

Web sites:

Envi Help: <https://www.harrisgeospatial.com/docs/home.html>

Specim: www.specim.fi

Geological Survey of Sweden: <http://www.sgu.se/en/>

National Oceanic and Atmospheric Administration: <http://www.noaa.gov/>

A. APPENDIX A

Appendix A-1 Tables with primary observation for the thin sections of the Utrillas Formation.

CAN 1	
SORTING: Poorly sorted	GRAIN SHAPE: Angular
GRAIN SIZE: 0.15 mm	UDDEN-WENTHWORTH SIZE CLASS: Fine sand
OBSERVATIONS: The framework constituents were floating in a clay matrix, most of which was composed of illite. Monocrystalline quartz grains show straight extinction and have inclusions. Feldspar grains were usually altered, especially at the grain edges. Tabular muscovite grains show preferential elongation direction. Organic matter rounded particles were found. Some high birefringence accessory minerals were found (probably tourmaline)	

CAN A	
SORTING: Poorly sorted	GRAIN SHAPE: Angular
GRAIN SIZE: 0.05-0.15 mm	UDDEN-WENTHWORTH SIZE CLASS: Very fine to fine sand
OBSERVATIONS: Less organic matter. Some areas were stained in Fe-oxides that acts as a cement. The matrix was homogeneous and composed of a low birefringence clay mineral. Muscovite was not common.	

CAN B	
SORTING: Poorly sorted	GRAIN SHAPE: Angular
GRAIN SIZE: 0.15-0.05 mm	UDDEN-WENTHWORTH SIZE CLASS: Very fine to fine sand
OBSERVATIONS: Some areas were stained in Fe oxides that acts as a cement. The matrix was composed of a low birefringence clay mineral (kaolinite). Muscovite and feldspar grains were rare. The overall porosity of rock is high.	

CAN E	
SORTING: Poorly sorted	GRAIN SHAPE: Angular
GRAIN SIZE: 0.05 mm	UDDEN-WENTHWORTH SIZE CLASS: Very fine grain
OBSERVATIONS: Majority of quartz grains were monocrystalline and present straight extinction. Some of grain their edges were "altered" by iron oxides. Muscovite grains were elongated and some of the broken and bended. Some of the muscovite grains were totally altered to clay minerals and stained by the Fe-oxides.	

Appendix A-1 (CONT.) Tables with primary observation of the Utrillas Formation thin sections.

CAN L	
SORTING: Poorly sorted	GRAIN SHAPE: Angular to subangular
	UDDEN-WENTHWORTH SIZE CLASS: Very fine grain
OBSERVATIONS: Majority of quartz grains were monocrystalline and present straight extinction. Some of grain their edges were "altered" by iron oxides. Muscovite grains were elongated and some of the broken and bended. Some of the muscovite grains were totally altered to clay minerals and stained by the Fe-oxides. In comparison with CAN-E the Fe-oxides were darker.	

CAN M	
SORTING: Bidomal	GRAIN SHAPE: Angular
GRAIN SIZE: 0.15-1.5 mm	UDDEN-WENTHWORTH SIZE CLASS: Coarse sand to fine sand
OBSERVATIONS: Feldspar grains were altered. Quartz grains were generally clean and present some with some inclusions. Quartz grains were sometimes fragmented.	

CAN C	
SORTING: Well-sorted	GRAIN SHAPE: Subangular to angular
GRAIN SIZE: 0.15 mm	UDDEN-WENTHWORTH SIZE CLASS: Very fine grain
OBSERVATIONS: Very few framework grain constituents. The matrix was composed of clay minerals. Qtz grains were moderately sorted and angular, monocrystalline. Some areas of the rock were stained with Fe iron	

CAN 9	
SORTING: Moderately sorted	GRAIN SHAPE: Subangular to angular (some subrounded very few)
GRAIN SIZE: 0.75 mm	UDDEN-WENTHWORTH SIZE CLASS: Coarse sand
OBSERVATIONS: Frame constituents were mainly monocrystalline (more abundant) and polycrystalline quartz. Grains were touching each other. Some well-defined book-shape and fan shape low birefringence clay minerals (kaolinite) were found. Feldspars were present. Tartan-like twining found (microcline). Comparing with other samples there in less matrix content (some Fe iron).	

Appendix A-1 (CONT.) Tables with primary observation of the Utrillas Formation thin sections.

CAN D	
SORTING: Moderately sorted	GRAIN SHAPE: Subangular to angular (some subrounded very few)
GRAIN SIZE: 0.2 mm	UDDEN-WENTHWORTH SIZE CLASS: coarse sand to very fine sand
OBSERVATIONS: Very few framework grain constituents were found. Quartz grains were moderately sorted and angular, monocrystalline. Some areas of the rock were stained with Fe iron. Some white micas found. The matrix was composed of clay minerals	

CAN 2	
SORTING: Bimodal	GRAIN SHAPE: Subangular to subrounded
GRAIN SIZE: 1 to 0.075 mm	UDDEN-WENTHWORTH SIZE CLASS: coarse sand to very fine sand
OBSERVATIONS: Bimodal. There were some sedimentary transported rounded clasts. Great abundance of white micas, most of them non-banded. Presence of organic matter particles. Porosity present.	

CAN P	
SORTING: Poorly sorted	GRAIN SHAPE: Subangular to angular
GRAIN SIZE: 1 to 0.075 mm	UDDEN-WENTHWORTH SIZE CLASS: Medium sand
OBSERVATIONS: Very similar characteristics to CAN D and CAN C. Very low content of organic matter. Some transported sedimentary grains.	

Appendix A-2 Point counting results of the Utrillas Formation facies. Abbreviations QRF: Quartz, Rock fragments, Feldspar, Rock Frag: rock fragments.

SAMPLE #	CAN-1	CAN-A	CAN-B	CAN-E	CAN-L	CAN-M	CAN-C	CAN-9	CAN-D	CAN-2
POINT COUNT										
Quartz	22	18	27	21	24	99	8	141	2	152
Feldspar	8	3	2	5	2	27	1	21	0	28
Rock frag	0							9		5
Matrix	82	176	208				180	14	189	14
Fe- oxide cement	98	12		172	186	79	38	2		3
Muscovite grains	3		1	3	8	2	1	7		5
Others (organic matter,...)	11	0		1	6		3	1		1
Accessories	0	3								
Pore	0	1	12	2		16	22	14	13	14
QFR Total	30	21	29	26	26	126	9	171	2	185
TOTAL	224	213	250	204	226	223	253	209	204	222
***	***	***	***	***	***	***	***	***	***	***
% QFR										
% Quartz	73.3	85.7	93.1	80.8	92.3	78.6	88.9	82.5	100.0	82.2
% Feldspar	26.7	14.3	6.9	19.2	7.7	21.4	11.1	12.3	0.0	15.1
% Rock fragments	0.0	0.0	0.0	0.0	0.0	0.0	0.0	5.3	0.0	2.7
TOTAL %	100.0	100.0	100.0	100.0	100.0	100.0	100.0	100.0	100.0	100.0
% PORE	0.000	0.469	4.800	0.980	0.000	7.175	8.696	6.699	6.373	6.306
% MATRIX	36.607	82.629	83.200	0.000	0.000	0.000	71.146	6.699	92.647	6.306